Nanoscale Coherent Diffractive Imaging using High-harmonic XUV Sources

Dissertation
submitted in partial fulfillment of the
requirements for the degree of
doctor rerum naturalium (Dr. rer. nat.)

FRIEDRICH-SCHILLER-
UNIVERSITÄT
JENA

Faculty of Physics and Astronomy

Getnet Kassa Tadesse

Name : Getnet Kassa Tadesse

Date of Birth : 09.03.1988

Place of Birth : Gondar, Ethiopia

Examiners

1. Prof. Dr. Jens Limpert
   Friedrich Schiller University of Jena
   Abbe Center of Photonics, Institute of Applied Physics

2. Prof. Dr. Christian Eggeling
   Friedrich Schiller University of Jena
   Institute for Applied Optics and Biophysics

3. Associate Prof. Dr. William Brocklesby
   University of Southampton
   Optoelectronics Research Centre

Date of Defense : 30.09.2019

Contents

Chapter 1

Introduction

Progress in fundamental science and technology relies on our understanding of the processes and mechanisms behind the systems under investigation. One of the indispensable tools in broadening our understanding and finding potential solutions to technological challenges is high resolution imaging. Among the variety of imaging modalities explored so far, light microscopy is the earlies and most commonly used one. Imaging with photons (as opposed to electrons or ions) has the advantage of longer penetration depths in addition to chemical sensitivity and spectroscopic information that can also be acquired [1, 2]. In 1873, Ernst Abbe put forward his famous formula describing the limits on the resolution of a microscope set by the wavelength of the light source and the numerical aperture (NA) of the optics used [3]. Except for samples suitable for super-resolution techniques, light sources with shorter wavelengths in the XUV and X-ray regime have to be used to achieve higher resolutions. Both full-field and scanning X-ray microscopes, therefore, demonstrated resolutions down to $\sim$ 10 nm beyond the reach of almost all super-resolution modes of light microscopy [4, 5]. However, the resolution of classical XUV/X-ray microscopes is mainly limited by the quality of the optics used in focusing or image formation.

Driven by the progress in coherent XUV/X-ray sources and iterative phasing algorithms, a new imaging modality known as coherent diffractive imaging (CDI) was demonstrated in the late 1990s [6]. CDI techniques avoid the use of image forming optics between the sample and the detector which overcomes the performance limitation due to focal power, losses and aberration of the XUV/X-ray optics. As a result, resolutions as high as 2 nm and 3 nm were demonstrated using CDI techniques at large scale facilities like synchrotron sources [7, 8]. The availability of amplitude and phase information in CDI techniques also gives the possibility of chemical composition mapping [8]. In combination with tomography, CDI techniques were used to non-destructively image complex 3D structures including integrated circuits and whole unstained cells with nanoscale resolutions [9, 10]. Until recently, the application of these techniques was mainly confined to large scale facilities like synchrotrons and X-ray free electron lasers (XFELs). These sources only offer limited access for beamtimes and are non-portable which hindered a broader use of CDI techniques for everyday scientific and commercial applications. The availability of table-top sources based on high-order harmonic generation (HHG) promises to exploit the full potential of CDI techniques by overcoming the issues of access and portability. CDI experiments employing table-top sources reported wavelength-scale resolutions although a reliable performance measure is yet to be performed [11–13]. The ultrashort pulse durations of HHG sources also enabled pump-probe experiments which was applied in studying magnetization dynamics, heat and energy transport among others [14, 15].

Potential applications of CDI techniques, e.g. in the semiconductor industry and biological sciences, still require higher resolutions and reasonable acquisition times than the currently reported performance levels. So far, table-top CDI setups couldn't resolve features $<$ 100 nm whereas typical feature sizes in semiconductor masks or organelles in biological cells are just few tens of nanometers. Given the longer wavelengths of $\sim 10\ nm - 40\ nm$ compared to synchrotrons, table-top CDI setups therefore require very high NA to achieve these resolution values. However, the photon flux of HHG sources was not high enough to record diffraction that makes use of the available NA of the setup in a reasonable exposure time. Fortunately, HHG sources have seen exceptional increase in coherent XUV flux during the last decade [16, 17]. In particular, fiber laser driven HHG sources demonstrated record-high photon flux in the XUV spectral range owing to their unique high power capabilities and novel strategies for power scaling. Nowadays, fiber laser driven HHG sources can deliver photon flux that exceeds 10^{14} photons/second in a single harmonic line at 21 eV [18]. This opened up new opportunities for scaling the performance of table-top CDI systems. But it also brought new challenges since a different regime has to be explored in terms of power handling and new limits on resolution. The separation of generated harmonic beam from the driving laser and ensuring stable illumination at high powers are some of the power-related challenges. Temporal coherence of the source and propagation effects in wavelength-sized features set new limits on resolution that were not reachable so far both in table-top and large scale setups. For high resolution ptychography, for example, the HHG source needs to be optimized for narrow spectral widths and small XUV beam sizes at the sample to overcome the resolution limit due to temporal coherence. Due to the wavelength-scale resolutions achievable with HHG sources, propagation phenomena that are not observable at synchrotron and XFEL sources (due to the high wavelength to resolution ratios) were shown to influence image quality [19]. These propagation effects and possible ways to overcome them also need to be explored in greater detail. In estimating imaging performance, a reliable resolution metric is necessary so as to qualify these techniques for real-world applications. Previous table-top setups mainly used knife-edge resolution tests and single isolated features to estimate performance. The possibility of numerical artifacts and artificially sharp features in phase retrieval also demands the use of a direct Rayleigh-type resolution criterion.

In this work, table-top CDI was pushed towards higher resolutions by employing fiber laser driven HHG sources delivering record-high photon flux. The high coherence and photon flux of the HHG source enabled the highest resolution CDI experiments on a table-top. In a holographic implementation of CDI which is relevant for time-resolved experiments, the smallest features resolved in a table-top setup were demonstrated with reduction of acquisition times from hours to minutes. For extended samples, as is the case for most real world applications, a Rayleigh-type resolution criterion was used for the first time to demonstrate imaging of features only few wavelengths in size. In the following chapter, the fundamental principles of diffraction theory and the basic ideas behind the variety of CDI implementations is discussed. A brief introduction into the process of HHG and the requirements on the coherence of sources for CDI is also presented. Details of the laser system and experimental setup used in this work are described in chapter 3 together with the CDI results with sub-wavelength resolution. The operating principle of a wavefront sensor developed for XUV wavelengths is also presented in this chapter along with a proof-of-principle experiment in the visible spectral range. In chapters 4, the highest resolution holographic CDI experiment on a table-top setup and refinement of resolution using iterative phase retrieval is presented. The waveguiding effects observed in the reconstructions are also described in this chapter using a numerical simulation of the sample structure. Chapter 5 covers imaging of extended samples using ptychography with wavelength-scale resolutions and stresses the importance of using a direct real space resolution metric in performance estimation. The last chapter provides a summary of the important results of this work and point possible directions for future works.

Chapter 2

Fundamentals

In this chapter, the fundamental principles and techniques necessary for a proper understanding of the results of the thesis are presented. We start by a discussion of the theory of diffraction which is the principle by which the techniques and findings in this work are based upon. We then proceed to a description of the basics of coherent diffractive imaging (CDI) techniques and point out the requirements, advantages and disadvantages of each modality. Coherence, which is the main requirement on the light source in CDI, and sources of coherent XUV/soft X-ray light are presented in the last subsections of this chapter.

2.1 Diffraction of Light

Imaging systems rely on the interaction of light (electrons or ions) with the sample so as to acquire an image representing the transmission, phase or any other property of the sample. In CDI, the underlying principle of light-matter interaction is diffraction of an incoming coherent light field by the sample to be imaged. First reported by Grimaldi with preliminary explanations by Huygens and Fresnel, diffraction is a consequence of the wave nature of light and cannot be accounted for in a ray optics representation [20]. Diffraction happens when a light field is transversally confined (by an object or by tight focusing) to small sizes or partially obstructed by an object, and it becomes more observable when the confinement is on the order of the wavelength of the light source.

2.1.1 Scalar diffraction theory

Propagation of electromagnetic waves has to satisfy Maxwell's equations in the material media through which the field is propagating. In the most general formulation, the Cartesian components of the electric and magnetic fields are coupled with one another through the properties of the material media. Therefore, a solution of Maxwell's equations, in general, requires doing a full vectorial analysis considering all field components of the electric and magnetic fields [21]. For the special case of linear, isotropic, homogeneous, non-dispersive and non-magnetic medium in the absence of free charges, this coupling between the field components is lifted. In this special case, each field component needs to satisfy the equation

$$\nabla^2 u(\mathbf{r},t) - \frac{n^2}{c^2}\frac{\partial^2 u(\mathbf{r},t)}{\partial t^2} = 0 \tag{2.1}$$

known as the scalar wave equation. The variable $u(\mathbf{r},t)$ stands for any of the field components E_x, E_y, E_z, H_x, H_y and H_z. The operation ∇^2 stands for the Laplacian, n is the refractive index of the medium and c is the speed of light in vacuum. In this work, we are interested in diffraction of light field from an object under investigation and its propagation in free space afterwards. In this diffraction phenomenon, the medium is inhomogeneous at the boundary of the object and the scalar wave equation is an approximation. Nevertheless, it has been shown the scalar approximation gives accurate results if the size of the diffracting object is larger than the wavelength and the diffracted field is recorded far away from the object [20]. A criterion for satisfying the latter of these two conditions is discussed in the next section and special cases when the former condition is not satisfied are investigated in section 4.3.

Considering a field with a certain frequency, the spatial and temporal dependence of the total field $u(\mathbf{r},t)$ can be separated. The resulting equation for the spatial component $U(\mathbf{r})$ is known as Helmholtz equation and can be written as

$$(\nabla^2 + k^2)U(\mathbf{r}) = 0 \tag{2.2}$$

where $k = 2\pi n/\lambda$ is the wave vector and λ is the wavelength. We are interested in solutions of Helmholtz equation that satisfy the boundary conditions for our system. In general, the diffraction problems encountered can be formulated as: given a field distribution at an initial plane $z = z_0$, what will the field distribution be at a parallel plane located a distance $z = z_1$. This scenario is depicted in Fig. 2.1 where the transversal plane is chosen to lie along the Cartesian x and y axes while the longitudinal axis is z.

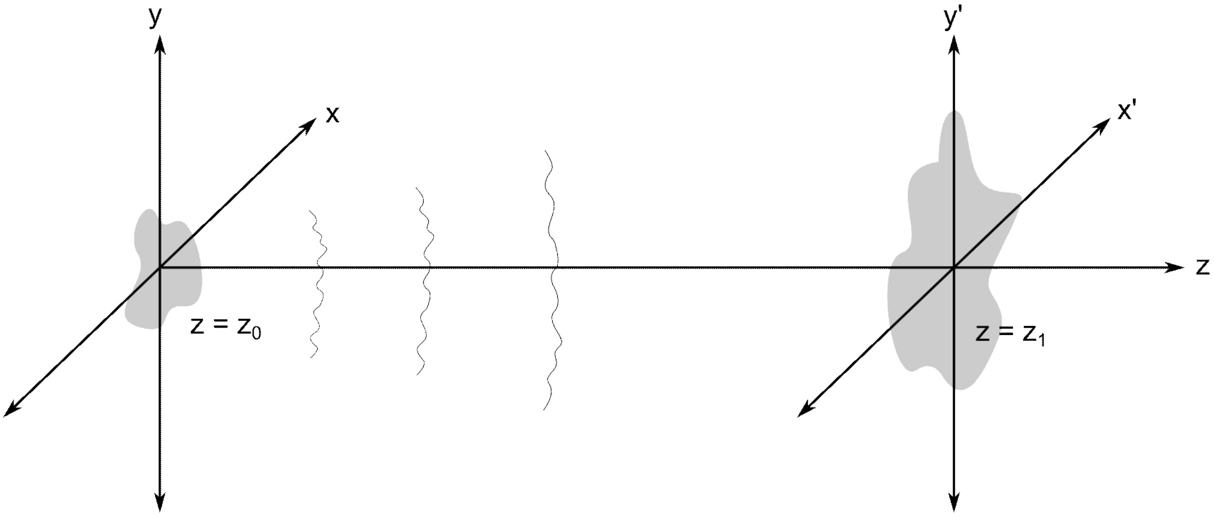

Figure 2.1: Formulation and geometry of diffraction from planar surfaces.

There are two common formulations to compute the field values at the new plane at $z = z_1$ which we will refer to as the detector plane. The first one uses Green's theorem to compute the field at a given point from a surface integral around that point. Both the Kirchhoff and Rayleigh-Sommerfeld diffraction formulas use this approach and a detailed discussion of these solutions can be found in [20]. We focus on the second formulation known as spectrum of plane waves (SPW) or angular spectrum method because of its simplicity and convenience for important approximations. SPW relies on the decomposition of a given field into plane waves propagating with different wave vectors using Fourier transformation.

The light field $U(x, y)$ at the initial plane $z = z_0$ (which will be referred to as the sample plane) can be expressed in terms of its so-called spatial frequency components using the inverse Fourier transform as

$$U(x, y; z_0) = \frac{1}{4\pi^2} \iint_{-\infty}^{\infty} A(\alpha, \beta; z_0) e^{i(\alpha x + \beta y)} d\alpha d\beta \tag{2.3}$$

where the spatial frequency components $A(\alpha, \beta; z_0)$ are computed by the Fourier transform of the wave field $U(x, y; z_0)$. For a given value of spatial frequenceis α_0 and β_0, $A(\alpha_0, \beta_0; z_0)$ is the complex amplitude of a plane wave propagating with wave vectors

$k_x = \alpha_0$ and $k_y = \beta_0$. The integral over α and β signifies that the light field is a superposition of these plane waves propagating in different directions. Substituting the expression for $U(x, y; z_0)$ into the Helmholtz equation of Eq. 2.2 and taking the forward propagating solution at the detector plane gives

$$A(\alpha, \beta; z_1) = A(\alpha, \beta; z_0) e^{i\sqrt{k^2-\alpha^2-\beta^2} z_1} \tag{2.4}$$

The expression in Eq. 2.4 is a manifestation that plane waves are normal modes of a linear, homogeneous and isotropic medium. As a result, only the phase of the plane wave changes while its amplitude is constant as long as the quantity $\sqrt{k^2 - \alpha^2 - \beta^2}$ is real. Once we have the values for the spatial frequencies at the detector plane, the light field in real space is a superposition which is again computed by an inverse Fourier transform as

$$U(x, y; z_1) = \frac{1}{4\pi^2} \iint_{-\infty}^{\infty} A(\alpha, \beta; z_1) e^{i(\alpha x + \beta y)} d\alpha d\beta \tag{2.5}$$

The Fourier and inverse Fourier transform operations can be numerically implemented using the fast Fourier transform (FFT) algorithm by discretizing the xy plane in a regular grid. In doing so, the sampling period in the initial and final planes will be the same and has to satisfy the Nyquist criterion in order to avoid aliasing effects. In addition, the computational window has to include most of the light field at the two planes in numerical implementations of SPW. Otherwise, the computational errors will be large due to reflections at the boundary [22]. But in a typical experiment, the initial light field will diffract to cover an area much larger than its initial size as it reaches the detector plane. To include this extended light field, the computational window has to be very large if this detector plane is far away. Maintaining the same sampling period in this scenario will result in very large matrix sizes beyond the computational capabilities of most machines. As a result, application of SPW is limited to analysis in the near-field where the field doesn't diverge significantly. However, the computational demands of SPW can be reduced by introducing approximations that are valid under certain conditions. These useful approximations are the topic of the following subsection.

2.1.2 Far-field (Fraunhofer) approximation

By using a priori information about the geometry of the diffraction phenomenon under investigation, the computation of the field distribution at a given plane can be greatly reduced. From the expression in Eq. 2.4, the transfer function of free space is the term $e^{i\gamma z_1}$ where γ is the z component of the wave vector given by $\sqrt{k^2-\alpha^2-\beta^2}$. There are scenarios where the x and y components of the wave vector (α and β) are very small compared to the wave vector k. This happens, for example, when considering diffraction of a loosely focused beam or from a sample with features much larger than the wavelength of the illumination. In these cases, the expression for γ can be approximated using Taylor expansion as

$$\sqrt{k^2-(\alpha^2+\beta^2)} \approx k - \frac{\alpha^2+\beta^2}{2k} \quad \text{for} \quad \alpha^2+\beta^2 \ll k^2 \tag{2.6}$$

The above approximation is termed as Fresnel (paraxial) approximation and is valid for diffraction with small angles to the optical axis. The transfer function and the corresponding response function (inverse Fourier transform of the transfer function) under Fresnel approximation is thus

$$H(\alpha,\beta;z_1) = \exp\left[ikz_1 - i\frac{\alpha^2+\beta^2}{2k}z_1\right] \tag{2.7a}$$

$$h(x,y;z_1) = -\frac{i}{\lambda z_1}\exp(ikz_1)\exp\left[i\frac{k}{2z_1}(x^2+y^2)\right] \tag{2.7b}$$

The wave field at the detector plane can then be evaluated by a convolution of $u(x,y;z_0)$ with $h(x,y;z_1)$ and minor rearrangement leading to

$$U(x,y;z_1) = \frac{e^{ikz_1}}{i\lambda z_1}e^{i\frac{k}{2z_1}(x^2+y^2)}\iint_{-\infty}^{\infty}\left[U(x',y')e^{i\frac{k}{2z_1}(x'^2+y'^2)}\right]e^{-i\frac{2\pi}{\lambda z_1}(xx'+yy')}dx'dy' \tag{2.8}$$

Note that the integral in Eq. 2.8 is simply a Fourier transform of the product of the field distribution at the sample plane and a quadratic phase factor. In addition, the quadratic phase factor is inversely proportional to the distance z_1 between the sample and detector planes. Since the integral over x' and y' is bounded by the size of the diffracting area (sample), the phase factor goes to unity under the condition

$$z_1 \gg \frac{k(x'^2 + y'^2)_{max}}{2} \tag{2.9}$$

The maximal extent of $(x'^2 + y'^2)_{max}$ is simply $2a^2$ where a is the overall size of the sample. Eq. 2.9 is commonly expressed in terms of the Fresnel number $N_f = a^2/(\lambda z)$ as any distance for which the condition $N_f < 0.1$ is satisfied. For a given wavelength and sample size, the detector plane is said to be in the far-field if it satisfies this condition. In the far field, the expression for the diffracted field and intensity at the detector plane becomes

$$U(x, y; z_1) = \frac{e^{ikz_1}}{i\lambda z_1} e^{i\frac{k}{2z_1}(x^2+y^2)} A\left(k\frac{x}{z_1}, k\frac{y}{z_1}\right) \tag{2.10a}$$

$$I(x, y; z_1) \propto \left| A\left(k\frac{x}{z_1}, k\frac{y}{z_1}\right)\right|^2 \tag{2.10b}$$

where $A(\alpha, \beta)$ is the Fourier transform of $U(x, y)$. Aside from the multiplicative factors, it can be seen that the diffracted field in the far field is given by the Fourier transform of the field at the initial plane. This approximation is termed as far field (Fraunhofer) approximation and is primarily used in computing diffraction patterns in this work. The diffraction pattern (diffracted intensity) $I(x, y)$ is defined as the squared amplitude of the field distribution $U(x, y)$ and is proportional to the measured intensity in an experiment [20]. As an example, for a 1 cm aperture illuminated by light with 532 nm wavelength, the detector plane has to be at $z > 1.8$ km to be in the far field. In contrast, the samples we are interested in this work are few microns in size. For a 5 μm sample illuminated by an XUV beam at 20 nm wavelength, the detector plane has to be at $z > 12.5$ mm which fits quite well in a typical experimental environment. The far field approximation makes iterative algorithms to be discussed in the next section feasible due to its speed and simplicity.

2.2 Coherent Diffractive Imaging (CDI) Techniques

In conventional microscopy, a sample is illuminated by a light (electron or ion) source and an image is formed on a detector by collecting waves scattered from the sample under investigation. In scanning alternatives, a focused illuminating beam is raster scanned across a sample and its transmission/reflection is integrated on a detector. The achievable resolution in both cases is mainly limited by the wavelength of the source and the numerical aperture of the collecting (or focusing) optics. A straightforward approach for improving resolution is therefore to use a source with shorter wavelength for illumination. As a result, the highest resolutions of 0.45 $\mathring{A}$ for silicon specimen and $< 3\mathring{A}$ for biological samples were reached using transmission electron microscopes [23, 24]. Electron microscopy has the disadvantage that it has lower penetration depth and is therefore limited to imaging thin sliced samples or outer surfaces [1]. Lots of interesting samples from biological cells to integrated circuits are thick and slicing them is destructive in addition to the complexities of sample preparation. Visible light microscopy has the advantage that the penetration depth is larger but the achievable resolution is limited to hundreds of nanometers except for specialized super-resolution techniques that could reach sub-100 nm resolution [5].

Imaging in the XUV and X-ray spectral range offers a compromise between electron and visible light microscopy in terms of resolution and penetration depth. Photons in the XUV spectral range, for example, can penetrate through μm thick samples while having Abbe limited resolution of tens of nanometers [2]. Unfortunately, the resolution achieved in conventional XUV/X-ray microscopes is limited by the quality of optics used in focusing the illumination or collecting the scattered waves. Focusing power and low transmission ($< 10\%$) of zone plate optics [25] used in conventional X-ray microscopes limits the achieved resolution to ≈ 10 nm so far [4, 26].

To overcome this limitation, light scattered from the sample can be directly recorded using a pixelated detector avoiding any lossy collecting optics between the sample and detector. These techniques are collectively known as coherent diffractive imaging (CDI) techniques. Resolutions of 2 nm $-$ 5 nm in the X-ray [7, 8] and sub-wavelength resolutions in the XUV spectral range [13] have already been demonstrated using CDI techniques. Sometimes also referred to as lensless imaging, the resolution in CDI techniques is limited only by the illumination wavelength and the effective numerical aperture (NA) of the measurement. Since only the intensity of the diffracted field is measured, CDI techniques mostly rely on iterative algorithms to recover the phase information. In the following subsections, the basic principle of CDI, phase retrieval algorithms and the different modalities used in this work are discussed.

2.2.1 Basics

As its acronym suggests, the basic principle of CDI is coherent diffraction of an incoming wave field from a sample under investigation. The diffraction phenomenon starts with an interaction between the sample and illumination as shown in Fig. 2.2 at the plane we refer to as the sample plane. The illuminating field is modified due to the interaction and this wave exiting the sample is referred to as the exit surface wave (ESW). The ESW then propagates in free space and its diffraction pattern is recorded by a pixelated detector. To establish a deterministic relationship between the measured diffraction pattern and the sample, coherence of the illuminating beam is central in CDI. For the upcoming discussion, we assume a spatially and temporally coherent illumination. Effects of partial coherence will be discussed later in section 2.3.

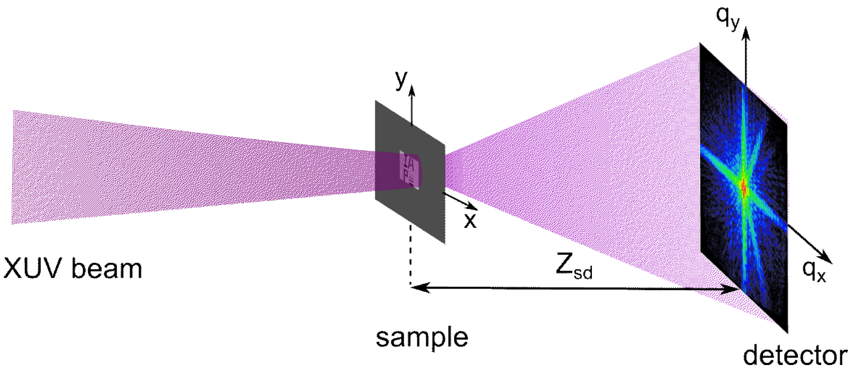

FIGURE 2.2: Schematic diagram of a basic CDI setup.

As discussed in the previous section, the diffracted field at the detector can be related to the wave exiting the sample (ESW) using a simple Fourier transform if the detector plane is in the far field of the ESW. For an isolated sample, Z_{sd} in Fig. 2.2 is chosen to be large enough to satisfy the far field criterion of Eq. 2.9 taking into account the estimated sample size. In this case, the detector plane is the Fourier plane and the measured intensity can be mapped onto a grid of spatial frequencies q_x and q_y. Throughout this thesis, the magnitude of the wave-vector $\mathbf{q}$ is defined as $1/\lambda$ to be consistent with literature in the CDI community. A one dimensional illustration of the diffraction phenomenon in Fourier space is shown in Fig. 2.3(a). The incident field has wave-vector of $\mathbf{q}_{in}$ and the field diffracted at an angle θ has a wave-vector designated as $\mathbf{q}_{out}$. Since both $\mathbf{q}_{in}$ and $\mathbf{q}_{out}$ have the same magnitude given by $1/\lambda$, all diffracted fields lie on a sphere with a radius of $1/\lambda$ known as the Ewald sphere. The momentum transfer (change in momentum) associated with this particular diffraction is then given by

$$\mathbf{q} = \mathbf{q}_{out} - \mathbf{q}_{in} \quad \text{where} \quad |q| = \frac{2}{\lambda} sin\left(\frac{\theta}{2}\right) \tag{2.11}$$

The momentum transfer vector $\mathbf{q}$ can be interpreted as the spatial frequency of the ESW $A(\alpha, \beta)$ in Eq. 2.3 in analogy with Bragg's law for diffraction from a crystal structure [27].

The real space equivalent of the same diffraction phenomenon is shown in Fig. 2.3(b) when the diffraction pattern is recorded on a pixelated detector with a total of N by N pixels and a pixel size of p. The overall size d of the detector is therefore Np as shown by the inset at the bottom of Fig. 2.3(b). The maximum angle that can be captured by the detector is therefore $tan^{-1}(d/2z_{sd})$ and the maximum momentum transfer q_{max} can be computed using Eq. 2.11. From the property of discrete Fourier transform (DFT), the pixel size of the image is inversely related to the maximum spatial frequency measured and is given by

$$s = \frac{\lambda}{4sin\left[\frac{1}{2}tan^{-1}\left(\frac{d}{2z_{sd}}\right)\right]} \tag{2.12}$$

Note that the pixel size s in the above equation is essentially the resolution limit due to the numerical aperture of the measurement and will be referred to as the Abbe limit. For small diffraction angles, $tan(\theta) \approx \theta$ and $sin(\theta) \approx \theta$ and Eq. 2.12 is approximately given by $\lambda z_{sd}/d$. The overall field of view of the image is given from the Fourier relation as

$$L_{FOV} = \frac{1}{\Delta q_{min}} = \frac{\lambda}{4sin\left[\frac{1}{2}tan^{-1}\left(\frac{p}{z_{sd}}\right)\right]} \approx \frac{\lambda z}{p} \tag{2.13}$$

The small angle approximation is also used in computing L_{FOV} above and it fits with the description in the upper inset of Fig. 2.3(b) since the total number of image pixels is also N. The momentum transfer $\mathbf{q}$ lies on a sphere (the Ewald sphere) although our

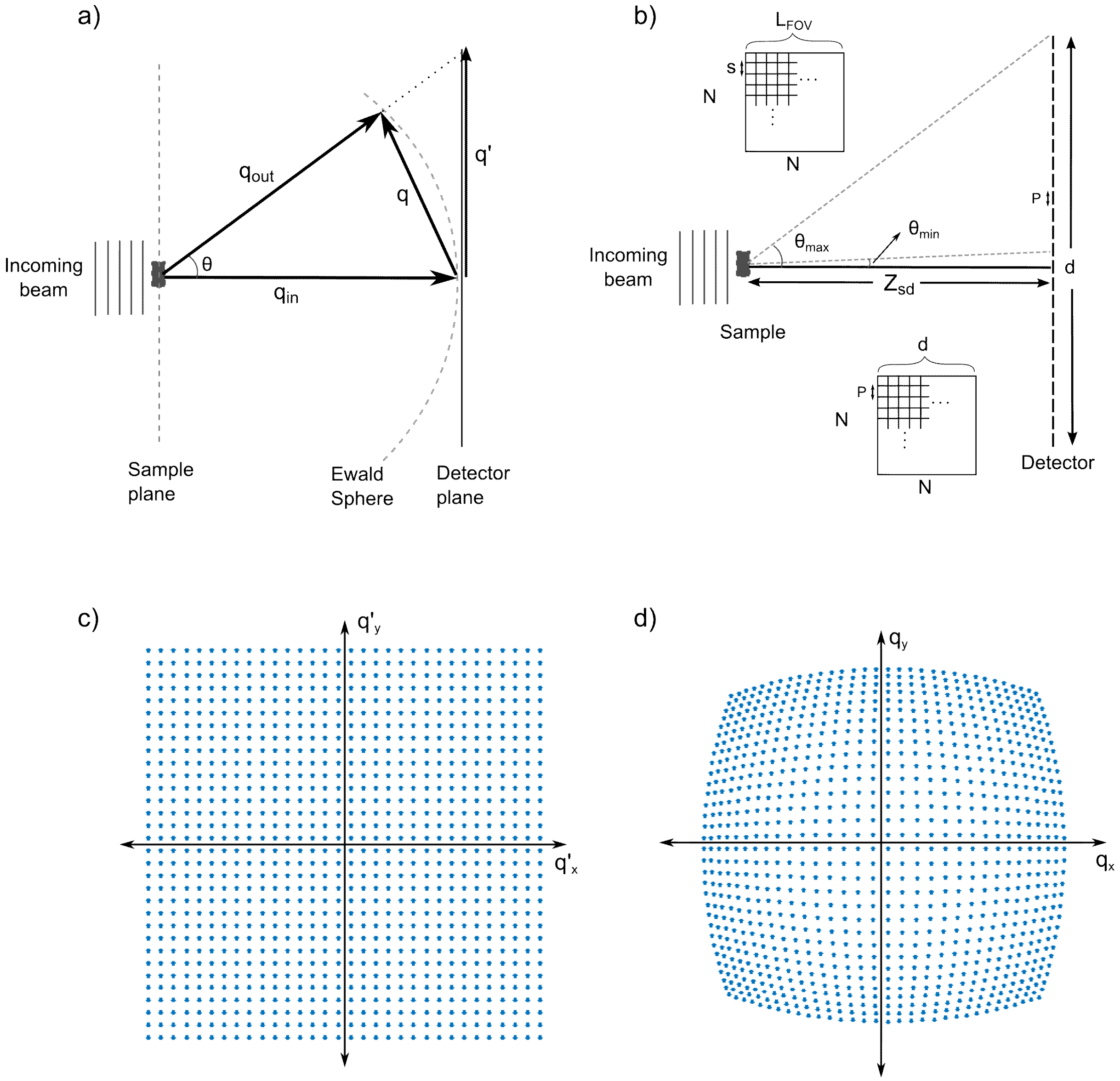

FIGURE 2.3: Details of diffraction in real and Fourier space. (a) Definition of momentum transfer vector and Ewald sphere. (b) Relation between experimental parameters (sample-detector distance, detector pixel size and number of pixels) and the reconstructed image parameters (pixel size and field of view). (c) Grid of spatial frequencies sampled by the detector. (d) Measured spatial frequencies after curvature correction.

detectors normally have flat surfaces. The measured momentum transfer vector for a given angle θ is therefore $\mathbf{q}'$ instead of $\mathbf{q}$ as shown in Fig. 2.3(a). A mapping of the measured $\mathbf{q}'$ vectors to the correct $\mathbf{q}$ vectors on the Ewald sphere is therefore necessary. This procedure is known as curvature correction [28] and is illustrated in Fig. 2.3(c) and (d) for a diffraction with a high NA of 0.7. In Fig. 2.3(c), each point represents one pixel of the detector that contains information about the spatial frequency components

$(q'_x,\ q'_y)$ and its periodicity comes from the periodicity of pixels in a detector. To perform curvature correction, the angles θ is calculated for a given $(q'_x,\ q'_y)$ from the geometry shown in Fig. 2.3(b) and the corrected vector $(q_x,\ q_y)$ were computed using Eq. 2.11. When this $\mathbf{q}'$ grid is mapped onto its corresponding $\mathbf{q}$ grid, the resulting q vector map is shown in Fig. 2.3(d). Measured spatial frequencies $\mathbf{q}'$ at higher angles (corners for example) experience the highest shift due to curvature correction while those at small angles are negligibly shifted.

In a CDI measurement, our detector only measures the intensity values corresponding to the spatial frequency map of Fig. 2.3(d) and the phase information will be lost. One mechanism to recover the phase is to use a special holographic setup that will be discussed in section 2.2.3. In the general case, the phase information will have to be recovered numerically through iterative phase retrieval algorithms. The principle of numerical phase recovery was first conceived by Sayre [29] as an extension of Shannon's theorem on sampling requirements for digitizing continuous wave signals [30]. There is a minimum frequency by which a signal has to be sampled in real space, known as the Nyquist frequency (f_{Nyq}), so that it can be faithfully represented in a discretized Fourier space. For the one dimensional case, a sample with an overall size of 'a' should be sampled in Fourier space with a spatial frequency spacing ($\varDelta q$) of at most $1/a$. This is equivalent to sampling at a frequency of $f_{Nyq} = a/(\lambda z_{sd})$ for small diffraction angles.

Sampling at the Nyquist frequency is sufficient to recover the real space information if both the Fourier amplitude and phase of the sampled signal are known. For a signal with real and Fourier space representations related with a DFT having N sampling points, there are 2N (N amplitude and N phase) known values in Fourier space (or equivalently 2N independent equations) and 2N unknowns in real space which can be computed using fast Fourier transform (FFT) algorithms. However, if the phase values of the Fourier space points are unknown, the number of equations (just N) is smaller than the unknowns in real space (2N). Interpreting the Fourier relation as sets of nonlinear coupled equations, the phase values in Fourier space can, in principle, be solved if the Fourier amplitudes are sampled at a sampling frequency $\geq 2f_{Nyq}$. This principle is known as oversampling and it is equivalent to zero padding of the real space points. Oversampling increases the number of equations from N to 2N. Meanwhile, the unknowns in real space are still 2N (N amplitude and N phase) since the newly padded values are known to be zeros. Fourier phase values can afterwards be numerically retrieved from the oversampled amplitude and the solution is shown to almost always be unique for the 2D and 3D cases [31, 32].

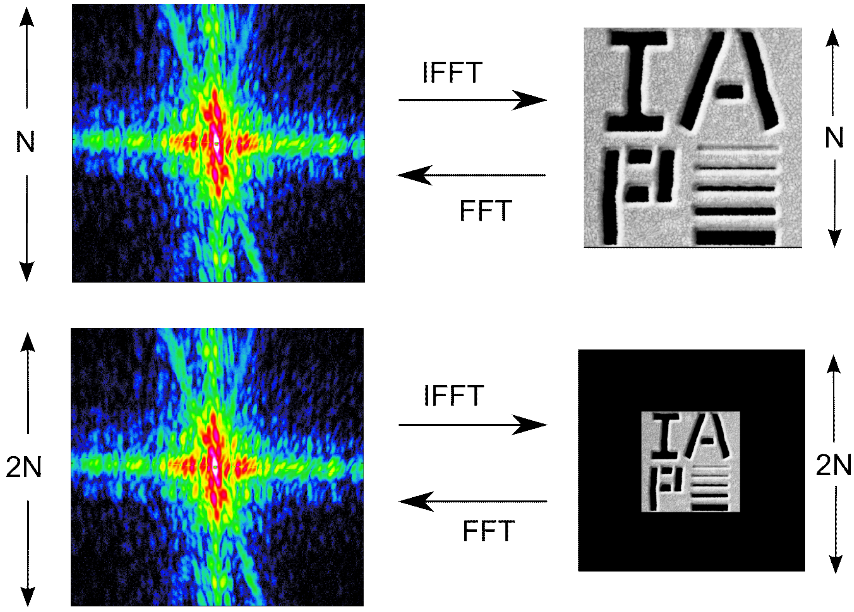

Figure 2.4: The effect of oversampling a diffraction pattern. Reducing the sampling interval (oversampling the diffraction pattern) by a factor of two results in zero padding the object by the same factor in both directions.

The 2D case of an oversampled diffraction pattern is shown in Fig. 2.4 where the idea of zero padding is illustrated. Oversampling can be expressed as the ratio of the object region and zero padded region as

$$\text{Oversampling ratio } (\sigma) = \frac{\text{object region} + \text{zero-padded region}}{\text{object region}} \tag{2.14}$$

An oversampling ratio $\sigma \geq 2$ is necessary to be able to solve the phase problem. Notice that, along one Cartesian coordinate, we only need to sample $\sigma^{1/2}$ times more to satisfy the oversampling criteria of Eq. 2.14. From the geometry described in Fig. 2.3(b), this so called linear oversampling degree (O) can be expressed as [33]

$$O = \frac{\lambda z_{sd}}{ap} = \sqrt{\sigma} \tag{2.15}$$

For an estimated sample size 'a', the phase of the diffracted field can be solved if we choose the pixel size and distance z_{sd} so that the oversampling degree of Eq. 2.15 is greater than $\sqrt{2}$. This solution is performed iteratively by the so called iterative phase retrieval algorithms (IRA) that are the topic of the next subsection.

2.2.2 Iterative phase retrieval algorithms

Once the oversampling method proposed the possibility of solving the phase problem discussed in the previous section, different algorithms were proposed to tackle the problem of finding an efficient and robust way to recover the phase information. The first practical algorithm for phase retrieval was proposed by Gerchberg and Saxton in 1972 for any imaging setup where only intensity distributions are measured e.g electron, visible or X-ray microscopy [34]. This algorithm assumes that the intensity distribution is known both in the sample and detector plane and uses an iterative scheme to solve for the phase distribution in both planes. But generally, the intensity distribution in the sample plane is unknown in imaging systems which makes this algorithm limited in application. The Gerchberg-Saxton algorithm was later modified where the knowledge about the intensity distribution at the sample was relaxed to just its estimated size and non-negativity [35]. It was later shown that if the sample is known to be in a defined region, known as its support, the phase problem can be solved even if the sample transmission is complex-valued (amplitude and phase) [36]. A generic diagram common to all phase retrieval algorithms is shown in Fig. 2.5.

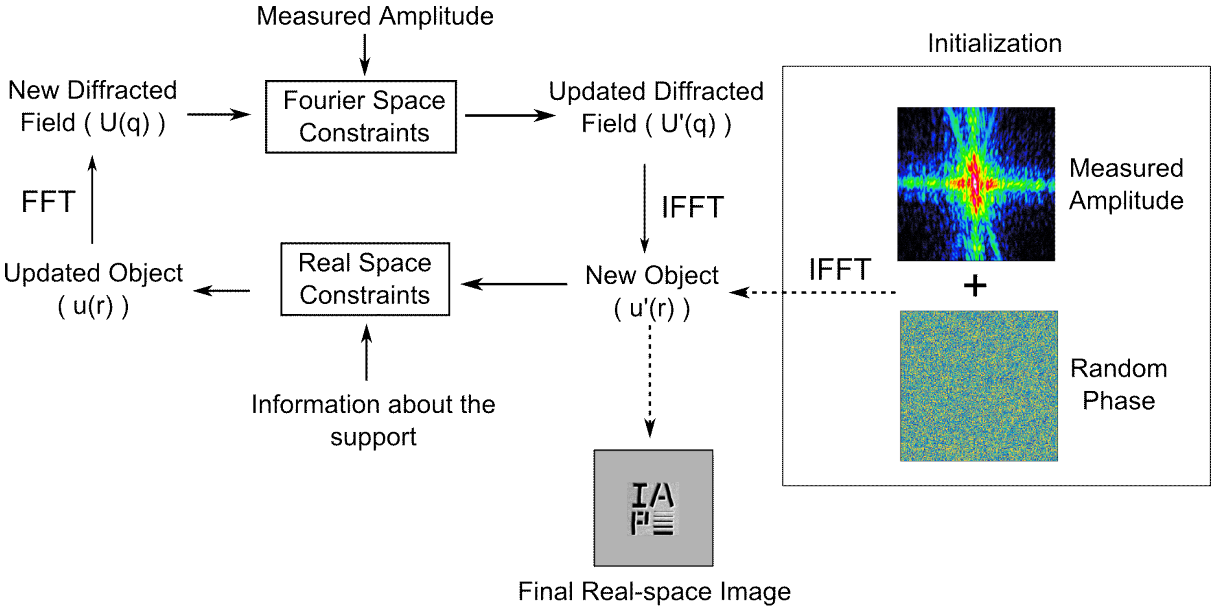

FIGURE 2.5: Illustration of the basic phase retrieval procedure in CDI.

The algorithm starts by applying a random phase to the measured diffraction amplitude and inverse Fourier transforming the resulting field to get a first estimate of the object. Then a priori information about the object is used as a constraint, known as real space constraint, to update this object estimate. The estimated object size is the main constraint here although different phase retrieval algorithms use slightly differing approaches. The updated image is then Fourier transformed to get a new estimate for the diffracted field. In the block named Fourier space constraints in Fig. 2.5, the amplitude of this diffracted field will be replaced by the measured amplitude while the phase is kept. The updated field in Fourier space is then inverse Fourier transformed to arrive at the object estimate for the next iteration. An error metric monitors the convergence to stop the iteration and a final real-space image is thereby retrieved.

In applying the real-space constraint, a priori information about the object can vary from a measured (accurate) real-space amplitude to a rough estimate of its overall spatial extent. The region where the object is assumed to have non-zero amplitude is referred to as the support. First experimental demonstrations of phase retrieval used a rectangular region larger than the known size of the object as a support and the algorithm then refines the features inside [6, 33]. A lower resolution image of the object acquired with a different technique (e.g. scanning electron microscopy) can also be used to define the support [37]. The shrink-wrap algorithm was later proposed to lift the need for these a priori information about the object [38]. In this algorithm, the first estimate of the support is the autocorrelation of the object (inverse Fourier transform of the measured diffraction intensity) with values above a given threshold. After a certain number of iterations, the support is updated to an area slightly bigger that the current object estimate. This is done by computing the convolution of the current object estimate with a Gaussian function and thresholding the result to a certain fraction of the maximum value.

For the following description of the different algorithms, $u_n(r)$ denotes the object estimate at the n^{th} iteration, $U_n(q)$ is its Fourier transform and $\sqrt{I(q)}$ is the amplitude of the measured diffraction pattern. The Fourier space constraint of replacing the computed diffraction amplitude with the measured one can be expressed mathematically as

$$\begin{aligned} u'_n(r) &= FT^{-1}\{U'_n(q)\} && \text{(2.16a)} \\ &= FT^{-1}\left\{\sqrt{I(q)} \cdot \exp[i \cdot \arg\{U_n(q)\}]\right\} && \text{(2.16b)} \\ &= P_M u_n(r) && \text{(2.16c)} \end{aligned}$$

The term P_M in the equation above signifies that the Fourier space constraint can be represented as an operator acting on the current estimate $u_n(r)$. The block named real-space constraint in Fig. 2.5 uses one of the approaches discussed previously to determine the support and computes the updated object estimate. In doing so, different algorithms were proposed so far. The simplest of these algorithms is the so called error reduction (ER) algorithm and the updated object is computed as [35]

$$u_{n+1}(r) = \begin{cases} u'_n(r), & \text{if } r \in S \\ 0, & \text{otherwise} \end{cases} \tag{2.17}$$

where $u_{n+1}(r)$ is the newly updated object, $u_n(r)$ is the object estimate from the previous iteration and $u'_n(r)$ is given by Eq. 2.16. The ER algorithm simply sets regions outside the support to zero and is shown to work fine when the intensity distribution in the object space is known. But for the general case, it is shown that convergence speed of the ER algorithm is low due to inability to escape stagnation at a local minima [39]. A modified algorithm that uses the principle of a feedback loop was proposed that resolves these issues. This algorithm is known as hybrid input-output (HIO) algorithm and uses the values outside the support as error signals rather than setting them to zero [35]. For the HIO algorithm, the updated object is computed as

$$u_{n+1}(r) = \begin{cases} u'_n(r), & \text{if } r \in S \\ u_n(r) - \beta u'_n(r), & \text{otherwise} \end{cases} \tag{2.18}$$

where β is a feedback parameter with values mostly between 0.5 and 1. The HIO algorithm is one variation of a class of input-output algorithms and shows the best convergence speed amongst them. The convergence speed can be controlled by the parameter β. Smaller β values result in slow but stable convergence while β values close to 1 result in faster convergence that could sometimes lead to instabilities. Another algorithm proposed to result in a more stable solution to phase retrieval than the HIO algorithm is the relaxed averaged alternating reflections (RAAR) algorithm [40]. The object space constraint in RAAR is expressed as

$$u_{n+1}(r) = \begin{cases} u'_n(r), & \text{if } r \in S \\ \beta u_n(r) + (1 - 2\beta) u'_n(r), & \text{otherwise} \end{cases} \tag{2.19}$$

In most practical scenarios, a combination of the above algorithms is used because their performance depends on the current state of the iterative process. The convergence of the algorithms can be monitored by an error metric defined in Fourier space as

$$E_F = \frac{\sum\limits_{q_x,q_y} \left(|U_n(q)| - \sqrt{I(q)} \right)^2}{\sum\limits_{q_x,q_y} I(q)} \tag{2.20}$$

The error value in a reconstruction by iterative phase retrieval algorithms will have a non-zero value at the end of the iteration. Independent reconstructions starting with random starting phases will therefore have minor differences from one another. One way to improve reliability is to have multiple independent reconstructions and take the average. A better strategy was suggested by Miao et al [41] in an approach known as guided hybrid input-output (GHIO) algorithm for the HIO algorithm (but can also be used with the RAAR algorithm). It divides the reconstruction process into multiple generations where the best reconstruction (one with lowest error) in one generation is used as a seed and merged with the remaining ones. The reconstructed object is virtually the same in all reconstructions of the last generation thus providing better reliability than simple averaging.

Convergence speed and stability of the phase retrieval algorithms depends on lots of factors for an experimental data. These include the coherence of the source, signal to noise ratio (SNR) of the measurement, the complexity of the sample and the parameters used in the algorithms. But in general, a higher oversampling ratio is shown to yield reconstructions with better quality with all other factors unchanged [33]. In addition, for a given measured diffraction pattern, there are two possible solutions to the phase retrieval process with one 180° rotated relative to the other (a property of Fourier transform). An object estimate in a certain iteration can thus have features that are a mixture of these two solutions. This issue, known as the twin-image problem, can cause stagnation during phase retrieval especially when the support is centrosymmetric or loose [42]. In these cases, additional steps such as those proposed in [43] are necessary to escape the stagnation and get a correct solution. Although image reconstruction by phase retrieval is an elegant approach for high-resolution imaging, reliability and speed are major issues that have to be dealt with. In the following sections, two approaches that increase the robustness of diffractive imaging are discussed.

2.2.3 Fourier transform holography

One strategy to overcome the issues of reliability and speed of iterative phase retrieval algorithms in CDI is to record the phase information during the diffraction measurement. This technique uses interference between a wave of interest (object wave) and a reference wave to record the phase profile of the object wave. First reported by Gabor, this technique is generally known as holography [44]. In the context of CDI, the object wave is the field diffracted from the sample under investigation. The reference wave can be the illuminating beam itself if the sample is small compared to the beam size and it is mounted on a transparent membrane. This variation is known as digital in-line holography (DIH) when the interference pattern (hologram) is recorded on a pixelated detector and high resolution imaging was demonstrated using this technique [45], [46]. Unfortunately DIH inherently suffers from the twin image problem where an unfocused complex conjugate image is overlapping with the reconstruction [47]. One way to avoid the twin image problem in holography is to spatially separate the object wave and the reference wave. This approach is known as Fourier transform holography (FTH). The basic idea of FTH is to use a reference structure in a close proximity of the sample in an off axis configuration. In the simplest case shown in Fig. 2.6(a), a small pinhole is located on the same plane as the sample but at a slightly shifted transversal position. The waves diffracting from the sample interfere with the reference waves from the pinhole and the resulting hologram is recorded in the far-field.

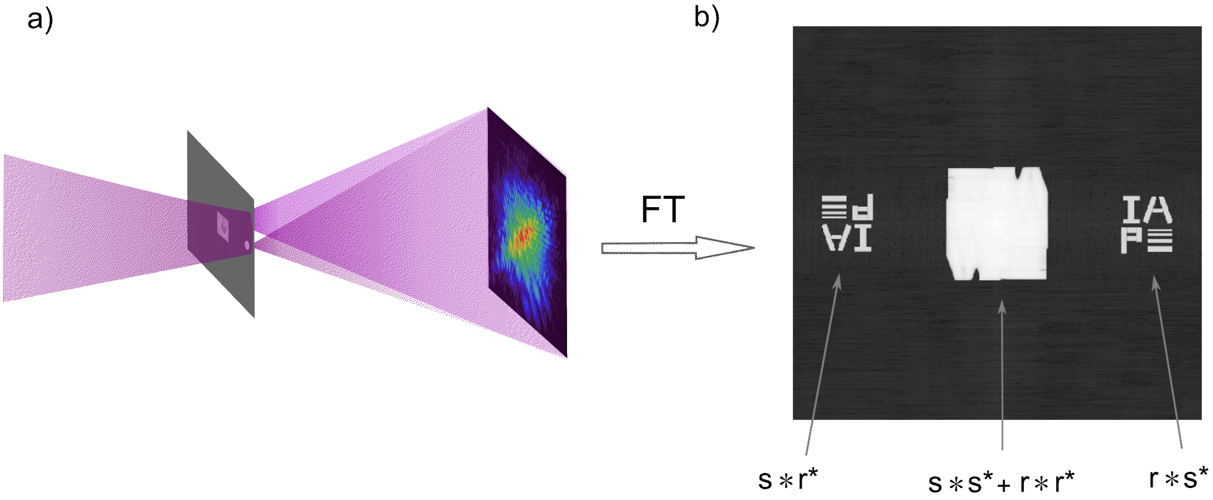

FIGURE 2.6: (a) Schematic diagram of a single reference FTH setup. (b) Illustration of the different terms in an FTH reconstruction. The term ’s’ represents the exit wave from the sample while ’r’ represents that of the reference structure.

In the following, a simple mathematical analysis of the recording and reconstruction of holographic images is presented. For a plane wave illumination, u_o with a full spatial and temporal coherence, the waves exiting the sample and the reference pinhole can be written as

$$s(x, y) = u_o t_s(x, y) \tag{2.21a}$$

$$r(x, y) = u_o t_r(x, y) \tag{2.21b}$$

where t_s and t_r are the transmission functions of the sample and reference pinhole. In the far-field, the recorded hologram is simply the Fourier transform of the superposition of the two waves and is given by

$$U(q_x, q_y) = FT\{u_t(x, y)\} = FT\{s(x, y)\} + FT\{r(x, y)\} \tag{2.22a}$$

$$U(q_x, q_y) = S(q_x, q_y) + R(q_x, q_y) \tag{2.22b}$$

Only the intensity (I) of the above hologram is recorded and this can be decomposed as follows

$$I = |U|^2 = |S + R|^2 \tag{2.23a}$$

$$= |S|^2 + |R|^2 + SR^* + S^*R \tag{2.23b}$$

The first two terms in the above equation represent the intensity values from the sample or reference alone while the last two terms represent the interference responsible for the fringes in a hologram. Extracting an image of the sample from the recorded hologram only requires performing a single Fourier transform, hence the name Fourier transform holography. The reconstructed image in FTH can be written as

$$FT\{I\} = FT\{|S|^2\} + FT\{|R|^2\} + FT\{SR*\} + FT\{S * R\} \tag{2.24a}$$

$$\begin{aligned} u_{rec}(x', y') = {} & s(x', y') * s^*(x', y') + r(x', y') * r^*(x', y') \\ & + s^*(x', y') * r(x', y') + r^*(x', y') * s(x', y') \end{aligned} \tag{2.24b}$$

where x' and y' are the real-space variables of the reconstructed image. The first two terms are the autocorrelation of the sample and that of the reference. These terms will be at the center of the reconstructed image as shown in Fig. 2.6(b). The third term is the cross-correlation of the sample with the reference and the fourth term is its complex conjugate. For the ideal case where the reference $r(x, y)$ is a delta function, the third and fourth terms in Eq. 2.24(b) become two copies of the sample $s(x', y')$ and $s * (-x', -y')$. Due to the off axis geometry, these two copies will be spatially separated as shown in Fig. 2.6(b) thereby avoiding the twin image problem. For a reference pinhole with finite diameter, these two copies will be blurred due to the convolution operation. The larger the diameter of the reference, the larger the blur and therefore the lower the achieved resolution.

Thus, in addition to the Abbe limit of the measurement, the achievable resolution in FTH is also limited to 70% of the reference pinhole diameter [48]. However, if the recorded hologram satisfies the oversampling criterion, iterative algorithms can additionally be used to refine the resolution achieved by FTH alone. In this case, the advantages of both FTH and conventional CDI can be exploited to achieve a robust high resolution imaging system. Decreasing the size of the reference in FTH to achieve better resolution results in lower flux going through it. This in turn lowers the contrast of the recorded holograms thereby decreasing the image SNR. Different schemes were proposed to tackle this issue in conventional FTH. One approach is the use of multiple references instead of just a single one. This scheme, known as multiple reference FTH, can increase image SNR by averaging the multiple copies available [49]. Usage of an extended reference (slits or rectangles) with sharp edges in holography was also proposed to enhance contrast and achieve a better resolution [50–52]. However, the linear differential operations involved in this technique was shown to amplify noise at higher spatial frequencies [53]. Other alternatives of using a structured reference was also proposed to have significant increase in image SNR [54].

2.2.4 Ptychography

One common limitation of the conventional CDI and FTH techniques discussed so far is that only isolated samples can be imaged. In conventional CDI, the sample has to be small enough to satisfy the oversampling criterion for the given geometry. In FTH, both the sample and the reference structure should fit in the field of view of the imaging system besides the constraint that they have to be sufficiently separated to avoid overlap during reconstruction. For a typical setup in the XUV spectral range, the overall size of the sample cannot exceed few microns for these techniques. To image extended samples, the illuminating beam can be scanned across the sample and multiple diffraction patterns recorded. Provided that each diffraction pattern can be phased appropriately, an extended image can be recovered. This technique is known as ptychography and the idea was first proposed in 1969 for crystalline samples [55]. It was later modified for non-periodic samples and subsequently combined with the phase retrieval algorithms discussed previously [56, 57].

The idea behind ptychography is best explained in relation to scanning transmission X-ray microscopy (STXM). In STXM, an illumination (probe) is scanned across an extended sample and the transmission of the sample at each scan point is integrated using a photodetector (a photodiode for example). The resolution in STXM is, therefore, determined by the probe diameter. If, instead, a diffraction pattern is measured at each scan point in STXM using a pixelated detector, we essentially have a ptychographic setup. The only additional requirements are coherence of the source and that the far-field criterion has to be fulfilled for a given exit wave. A schematic diagram of a ptychographic imaging setup is shown in Fig. 2.7(a) below. An illuminating beam (probe) is confined in space at the sample plane either by focusing or by using a pinhole. The probe size determines the size of the exit wave and it, therefore, determines the sampling to be used in Fourier space and the sample-detector distance. The sample is raster scanned across the probe and diffraction patterns are recorded at each scan point. A typical set of concentric scan points is shown in Fig. 2.7(b) together with the path followed during a measurement. As shown in the inset of Fig. 2.7(a), there needs to be an overlap in the area covered by the probe between successive scan points. The oversampling criterion in CDI and the reference wave in FTH are replaced by the overlap criterion in ptychography. It states that there has to be sufficient overlap between successive scan points for the phase retrieval to work successfully. A given sample area is illuminated by multiple scan points and the resulting data redundancy allows for robust image reconstruction. The optimum overlap was shown to be $\sim 60\%$ where overlap is defined as $O = 1 - a/d$, a is the distance between scan points and d is the beam diameter [58].

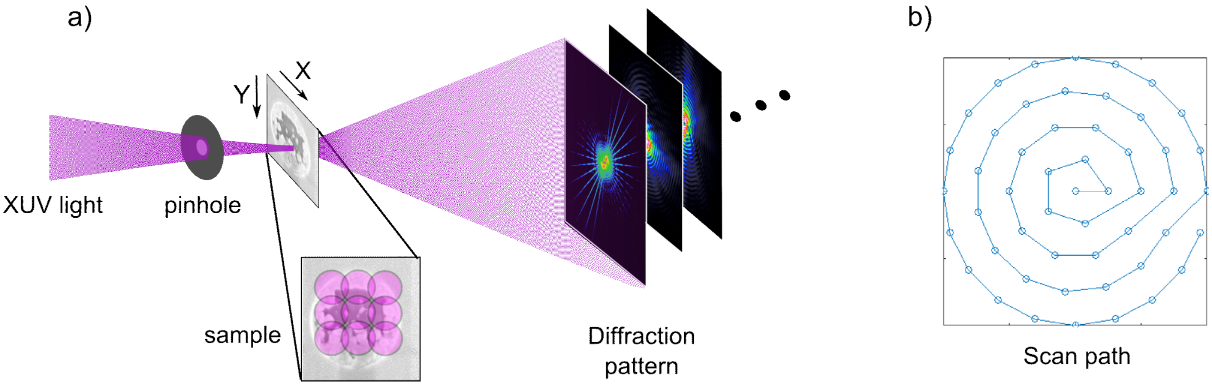

FIGURE 2.7: (a) A ptychographic imaging setup with a beam constraining pinhole. Inset of the sample shows the multiple overlapping illuminations with one diffraction pattern acquired per illumination. (b) A typically used spiral scan pattern.

The ptychographic reconstruction algorithms take the diffraction patterns and their corresponding scan coordinates to recover the amplitude and phase profile of the sample together with the illuminating probe. Consider a ptychographic dataset of J measured diffraction patterns $I_j(q)$ where j = 1, 2, ..., J and $q = (q_x, q_y)$ is the spatial frequency coordinate. In real space, this corresponds to a set of J exit waves $\psi_j(\mathbf{r})$ where $\mathbf{r}$ is the real space coordinate. The reconstruction problem is formulated as finding the sample $O(\mathbf{r})$ and probe $P(\mathbf{r})$ profiles that satisfy the following constraints:

$$\psi_j(\mathbf{r}) = O(\mathbf{r})P(\mathbf{r} - \mathbf{r}_j) \quad \text{for } j = 1, 2, ..., J \tag{2.25a}$$

$$I_j(\mathbf{q}) = |FT\{\psi_j(\mathbf{r})\}|^2 \tag{2.25b}$$

The first part of Eq. 2.25 is known as the overlap constraint and states that the exit waves $\psi_j(\mathbf{r})$ shall be expressed as a product of the sample profile and probe profile at the specified scan point $\mathbf{r}_j$ for $j = 1, 2, ..., J$. The second part is the Fourier constraint that establishes the Fourier relation between each exit wave and its corresponding diffraction pattern. A number of algorithms have been proposed to solve the ptychographic reconstruction problem[59–61] and the two commonly used ones will be briefly discussed. These are the extended ptychographical iterative engine (ePIE) and the difference map

(DM) algorithms. The main difference between the two is that ePIE takes one diffraction pattern at a time while DM considers all diffraction patterns in performing a single iteration.

In the ePIE algorithm, the diffraction patterns are first arranged in a random order $s(j)$ for $j = 1, 2, ...J$ and the reconstruction proceeds as follows [59]:

i) Take the object and probe estimates from the previous iteration and compute the current estimate of the j^{th} exit wave as

$$\psi_j(\mathbf{r}) = O(\mathbf{r})P(\mathbf{r} - \mathbf{r}_{s(j)}) \tag{2.26}$$

For the first iteration, take a probe with an estimated size and shape of the illumination and the object as free space.

ii) Apply the Fourier constraint

   (a) Fourier transform the exit wave estimate $\Psi_j(\mathbf{q}) = FT\{\psi_j(\mathbf{r})\}$

   (b) replace the modulus of $\Psi_j(\mathbf{q})$ by the measured diffraction amplitude

$$\Psi_j(\mathbf{q}) = \sqrt{I_{s(j)}(\mathbf{q})}\frac{FT\left\{\psi_j(\mathbf{r})\right\}}{\left|FT\left\{\psi_j(\mathbf{r})\right\}\right|} \tag{2.27}$$

   (c) Compute the updated exit wave estimate as : $\psi_j\prime(\mathbf{r}) = FT\{\Psi_j(\mathbf{q})\}$

iii) Apply the overlap constraint. Compute the object and probe estimates from the updated exit wave

$$\text{Object update function :} \quad O_{j+1}(\mathbf{r}) = O_j(\mathbf{r}) + \alpha\frac{P_j^*(\mathbf{r} - \mathbf{r}_{s(j)})}{\left|P_j(\mathbf{r} - \mathbf{r}_{s(j)})\right|_{max}^2}(\psi\prime_j(\mathbf{r}) - \psi_j(\mathbf{r}))$$

$$\text{Probe update function :} \quad P_{j+1}(\mathbf{r}) = P_j(\mathbf{r}) + \beta\frac{O_j^*(\mathbf{r} - \mathbf{r}_{s(j)})}{\left|O_j(\mathbf{r} - \mathbf{r}_{s(j)})\right|_{max}^2}(\psi\prime_j(\mathbf{r}) - \psi_j(\mathbf{r}))$$

The variables α and β control the amount of feedback from the previous iteration and values between 0.5 and 1 are commonly used for better performance [59]. The object update function adds a weighted feedback of the difference between the new and previous exit wave estimates while using the probe as a support. The same is true for the probe update function.

iv) If $j < J$, proceed to step (i) with $j \rightarrow j+1$ using the diffraction pattern $I_{s(j+1)}$. But if $j = J$, one full iteration is complete. Therefore, quit if the total number of iterations is reached. Otherwise, proceed to step (i) with $j = 1$.

The DM algorithm is different from the ePIE algorithm mainly in applying the constraints for all j values in parallel. The Fourier constraint is the same as ePIE except that it is now performed on all exit waves in one step. The overlap constraint in DM is applied as follows [60]

$$O(\mathbf{r}) = \frac{\sum_j P^*(\mathbf{r} - \mathbf{r}_j)\psi_j(\mathbf{r})}{\sum_j |P(\mathbf{r} - \mathbf{r}_j)|^2} \tag{2.28a}$$

$$P(\mathbf{r}) = \frac{\sum_j O^*(\mathbf{r} + \mathbf{r}_j)\psi_j(\mathbf{r} + \mathbf{r}_j)}{\sum_j |O(\mathbf{r} + \mathbf{r}_j)|^2} \tag{2.28b}$$

Note that the two equations above are coupled and summed up over all j values. Therefore, the object and probe estimates are computed iteratively within themselves. The first estimate for $O(\mathbf{r})$ is computed using $P(\mathbf{r})$ from the previous iteration and this object estimate is used to compute the current probe estimate in Eq. 2.28(b). A few iterations of Eq. 2.28(a) and (b) are shown to suffice. The algorithm then proceeds to the next iteration using the difference map iteration procedure detailed in [62]. This iteration procedure is similar to the HIO algorithm described by Eq. 2.18. The iterations are performed until a certain error threshold or a predefined number of iterations is reached.

A variety of related algorithms have been proposed that improve the quality of the reconstruction when there are inaccuracies in position, limited coherence, noise and other experimental issues [61, 63, 64]. The Maximum Likelihood algorithm is one example that uses a nonlinear optimization approach and provides images with improved qualities [61]. In addition, different algorithms for correction of positioning inaccuracies have been suggested and these are indispensable since nanometer-scale positioning is challenging [63, 65].

Ptychography has stricter stability requirements on the light source and sample positioners compared to conventional CDI and FTH. This is because the probe profile has to be constant throughout the scan and the positioning errors have to be much smaller than the scan step. In addition, an accurate knowledge of the sample-camera distance is necessary since this determines the pixel size of the reconstruction. An accurate overlap between successive exit waves in turn requires knowledge of the correct pixel size. The ptychographic reconstruction discussed so far relies on the validity of the projection approximation which is expressed in Eq. 2.25(a). This approximation is valid only when the object is optically thin (thickness $\sim$ wavelength) in which case the exit wave is a product of the probe and object transmission function. For thick objects, the exit wave can no longer be expressed as a simple product and propagation through the object has to be taken into account. One approach for ptychographic reconstruction of thick objects is the multi-slice method that considers multiple thin slices of the object and propagates the exit wave within these slices [66].

2.3 Coherence Requirements

As the name suggests, CDI techniques rely on coherent diffraction and coherence of the light source is a central requirement for successful image retrieval. Generally, a source is said to be coherent when portions of its wavefront separated in space and time are correlated and able to interfere with one another. A detailed mathematical treatment of coherence, metrics for quantifying it and discussions of partial coherence can be found in classic optics books as [21, 67]. There are two measures of coherence of a light source: spatial and temporal coherence. The discussions about the different CDI techniques so far assumed sources that are both spatially and temporally coherent.

Spatial coherence refers to how two parts of a wavefront from a source transversally separated in space are correlated with one another and Young's double slit experiment is commonly used to measure it. The visibility of the interference fringes from a double slit is defined as

$$\text{Visibility}(V) = \frac{I_{max} - I_{min}}{I_{max} + I_{min}} \tag{2.29}$$

where I_{max} is the intensity at the zeroth order fringe and I_{min} is that at the first minimum. Recently, non-redundant array of pinholes have been suggested to have a more complete measure of the degree of spatial coherence along different transversal directions [68]. For CDI, spatial coherence determines the maximum size of the sample for which waves from its opposite ends are able to interfere and can be expressed in terms of transversal coherence length (ξ_t). For this purpose, ξ_t of a source can be related to the divergence angle of the radiation and the observation distance as [25]

$$\xi_t = z\varDelta\theta = z\frac{\lambda}{2\pi d} \tag{2.30}$$

where z is the observation distance, $\varDelta\theta$ is the divergence angle, λ is the wavelength and d is the source size. It has been shown that a transversal coherence length (ξ_t) larger than twice the sample size (a) is recommended for conventional CDI [69]. But if a larger oversampling ratio (O) is used, this criterion is modified to $\xi_t > Oa$ since the beam has to be coherent for the sample and the zero-padded region of the reconstruction. Equivalently, finer details of the diffraction pattern have to be recorded faithfully for higher field of view (or higher oversampling ratio). Partial spatial coherence tends to decrease the visibility of diffraction fringes for all spatial frequencies. Thus algorithmic approaches can be used to improve the reconstruction quality of diffraction measurements with partial spatial coherence. One such method models this effect by a convolution of the far field pattern with a coherence function [70]. Another method suggested for ptychography models the probe as an incoherent superposition of multiple modes that are incorporated in the iterative phase retrieval algorithms [71].

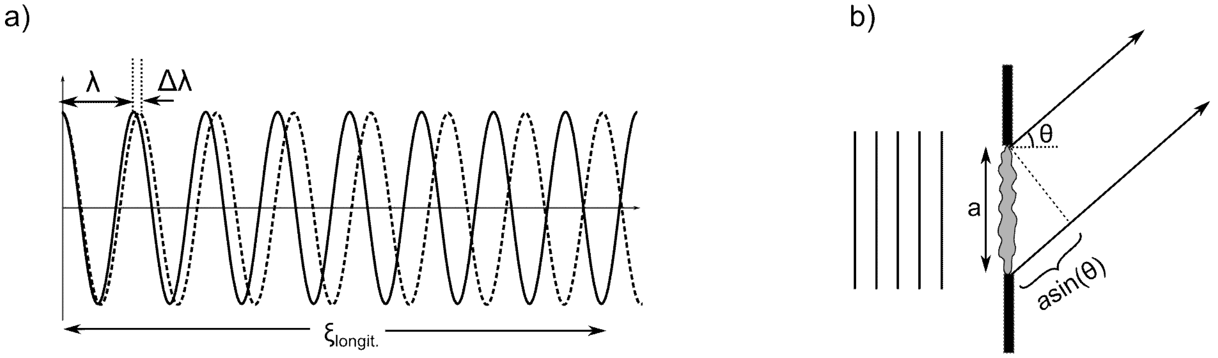

FIGURE 2.8: (a) Illustration of the relation between longitudinal coherence length and spectral bandwidth of a source. (b) Path length difference between opposite edges of a sample for diffraction at an angle θ.

On the other hand, temporal coherence refers to correlation between two wavefronts from a source that are separated in time. Equivalently, it can be expressed in terms of the longitudinal distance over which two wavefronts are able to interfere. Temporal coherence simply expresses how monochromatic a source is and it is quantified by measuring the spectral bandwidth. The relation between the spectral bandwidth ($\varDelta\lambda$) of an illumination and its longitudinal coherence length ($\xi_{longit.}$) is illustrated in Fig. 2.8(a). For a source at a central wavelength of λ with a bandwidth of $\mathit{\Delta}\lambda$, two waves at opposite ends of the spectrum will be out of phase after a certain longitudinal distance. This distance is termed as the longitudinal coherence length and is found to be [72]

$$\xi_{longit.} = \frac{\lambda^2}{2\mathit{\Delta}\lambda} \tag{2.31}$$

For a sample with an overall size of a in a CDI setup shown in Fig. 2.8(b), the longitudinal separation between waves diffracted at an angle θ from opposite ends of the sample is given by $a\sin(\theta)$. If this separation is larger than $\xi_{longit.}$, the two waves are incoherent with one another and won't produce an interference fringe. Since the longitudinal separation is dependent on the diffraction angle (and therefore the measured spatial frequency), temporal coherence puts a limit on the maximum achievable resolution given by [72]

$$d \geq a\frac{\mathit{\Delta}\lambda}{\lambda} \tag{2.32}$$

For a measurement with an oversampling degree O, the right side of the above equation has to be multiplied by O since a larger effective size is being considered [33]. For a ptychographic setup, the variable a in Eq. 2.32 refers to the size of the exit wave in a reconstruction which is roughly the size of the illuminating beam. Note that the resolution limit due to temporal coherence could be stricter than the Abbe limit of Eq. 2.12 if the beam size exceeds a certain value ($\sim 10\ \mu$m for XUV beams). There are experimental as well as algorithmic approaches to overcome the limit of imaging performance due to partial temporal coherence. Tuning the generating conditions for XUV/X-ray radiation for the narrowest bandwidth and subsequent use of frequency-selective elements (gratings, monochromators or multi-layer mirrors) can be performed during the experiment. For ptychography, reducing the focal spot size of the illuminating beam is also an alternative according to Eq. 2.32. For a known spectrum of the source, the relative magnitude and distribution of multiple wavelengths can be incorporated in the phase retrieval algorithms for improved performance [73]. Algorithms that decompose the illuminating beam into multiple modes previously suggested for tackling partial spatial coherence are also shown to be applicable here [71, 74].

2.4 High-order Harmonic XUV Sources

In high performance imaging systems, the source of light (electron or ion) is one of the main components that determines the quality, measurement time or any other performance metric. As a consequence of the Abbe limit, the resolution of an imaging system is fundamentally limited by the wavelength of the source. Thus, sources with the shortest wavelength that deliver enough photon flux are necessary for high resolution imaging. As discussed in the previous chapter, CDI techniques in particular have an additional requirement on the coherence of these sources. Development of short wavelength coherent sources and scaling of their photon flux was therefore an active research area for the last few decades.

2.4.1 XUV/Soft X-ray sources

The brightest sources of XUV and X-ray light so far are synchrotrons and X-ray free-electron lasers (XFELs). These sources mostly use transversal acceleration (undulation) of relativistic electrons in dedicated large scale storage rings or linear accelarators [75, 76]. Nowadays, third generation synchrotrons can generate X-rays from few hundred eV to hundreds of keV with brightness on the order of 10^{21} photons/(s mm^2 mrad^2 0.1% bw) while XFELs generate pulses in the XUV and soft X-ray spectral range with peak brightness orders of magnitude higher than synchrotrons [77]. However, the spatial coherence of synchrotrons is generally low and spatial filtering is usually necessary that results in reduced the photon flux for an experiment [78]. XFELs also suffer from shot-to-shot fluctuation of pulse parameters as well as some timing jitter [77]. But most importantly, these sources are expensive and not easily accessible since they involve large scale facilities where users have to apply for beamtime. Table-top XUV/soft X-ray sources are cheaper and more accessible alternatives and have already been used for imaging and spectroscopic applications. Compact XUV/soft x-ray sources that employ laser-produced and discharge-tube plasmas have been applied in full field soft x-ray microscopy [79, 80]. These sources, however, have limited spatial coherence in addition to the low photon flux and applications in imaging achieved only moderate resolutions [81, 82].

About three decades ago, a frequency conversion technique for generating coherent flux in the XUV/soft X-ray spectral region was experimentally observed [83, 84]. In this technique, known as high-order harmonic generation (HHG), an intense infrared/visible laser interacts with a non-linear medium to generate multiple odd harmonics from tens of eV up to keV photon energies [16, 85]. The availability of compact high power driving lasers makes HHG a table-top XUV/soft X-ray source. In addition, HHG sources have a high degree of spatial coherence because the generated XUV/soft X-ray beam follows the spatial properties of the driving laser (wavefronts are phase-coupled) [86, 87]. Ultrashort pulses with femtosecond to attosecond pulse durations are generated in an HHG process which makes these sources attractive for time-resolved studies [88]. A drawback of the HHG process is the low conversion efficiency from the infrared/visible laser of 10^{-5} for XUV beams around 30 eV and 10^{-9} for soft X-ray beams around 300 eV [18, 89]. However, the conversion efficiency does not set a strict limit on the photon flux of HHG sources since the generated flux scales with the average power of the driving laser. Recent works in high power laser development demonstrated femtosecond fiber laser systems with more than 3 kW average power [90]. This progress together with pulse compression schemes at high average powers increasingly compensate for the low conversion efficiency of HHG processes and mW class HHG sources are already available [18]. A high photon flux HHG source is used in the CDI experiments discussed in this work. In the following sections, a brief discussion of the principle of HHG processes and phase matching is presented. Details about the high power lasers used to drive the HHG process will be discussed in the next chapter.

2.4.2 Principle of HHG

The interaction of light with matter is mostly dealt with in the realm of linear optics. The response of the material media to the incoming electric field, known as the electric polarization, is considered to vary linearly with the electric field strength in this regime. When the intensity of the incoming field is high enough, the medium starts to respond in a non-linear fashion and additional non-linear terms have to be considered in the description of the light matter interaction. With the advent of high power ultrashort pulsed lasers, peak intensities on the order of 10^{16} W/cm^2 were reachable which are intense enough to ionize an electron from its parent atom [91]. In this scenarios, the commonly used perturbative approach to the non-linear response of the media is not valid anymore. High-order harmonic generation (HHG) is one such process where an electron is tunnel ionized by an intense electric field and subsequently recombines to generate multiple harmonics of the driving laser field. Although observed in solids as well, HHG sources mainly use noble gases to generate coherent XUV/soft X-ray flux as is also the case in this work.

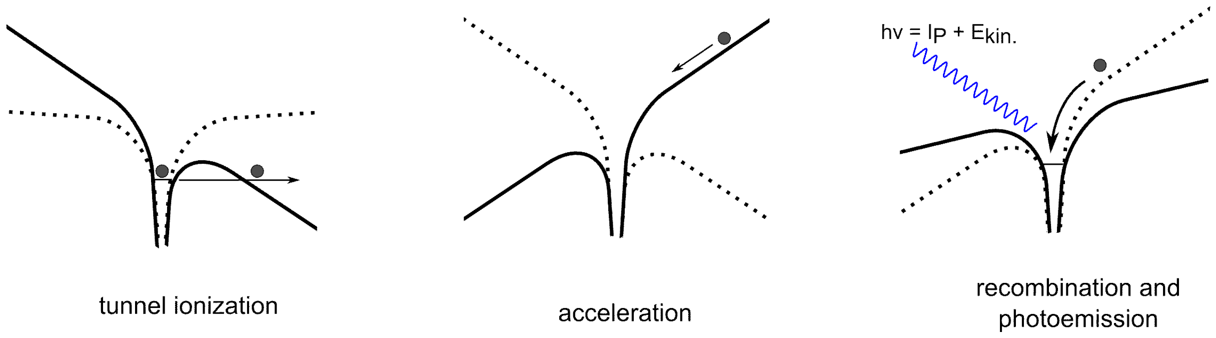

tunnel ionization

acceleration

recombination and photoemission

FIGURE 2.9: An illustration of the three step model of high harmonic generation.

A semi-classical model known as the three-step model that nicely explains the process of HHG was developed by Kulander and Corkum [92, 93]. Without the laser field, the electron is bound by the Coulomb potential of the atom shown by the dotted line of Fig. 2.9(a). The high intensity of the laser field modifies this potential and tunnel ionization of the electron is possible (dark curve of Fig. 2.9(a)). The electron is then accelerated by the laser field as shown in Fig. 2.9(b). Upon a change in polarity of the field, it has a certain probability of being accelerated back and recombining with its parent ion (Fig. 2.9(c)) thereby generating a high energy photon.

A typical spectrum of an HHG source is depicted in Fig. 2.10 and shows three distinct regimes. The first few harmonics show a reduction of generated flux as the harmonic order increases as predicted in perturbative theory. However, the harmonic orders above a certain value have a nearly constant intensity in the so called plateau regime [94]. The HHG flux then drops dramatically after a certain cut-off frequency and no harmonic flux is observed afterwards. The intensity of the HHG signal depends on the response of a single noble gas atom to the laser field (known as the single atom response) and the total number of atoms within the laser field [95]. Phase matching of the photons generated with those of the driving laser and re-absorption effects are additional factors that determine the generated photon flux.

The energy of the generated photon is the sum of the ionization potential (I_p) and kinetic energy of the electron. The spacing between successive harmonics is twice the fundamental frequency (Fig. 2.10) because harmonic signal is generated at every half cycle of

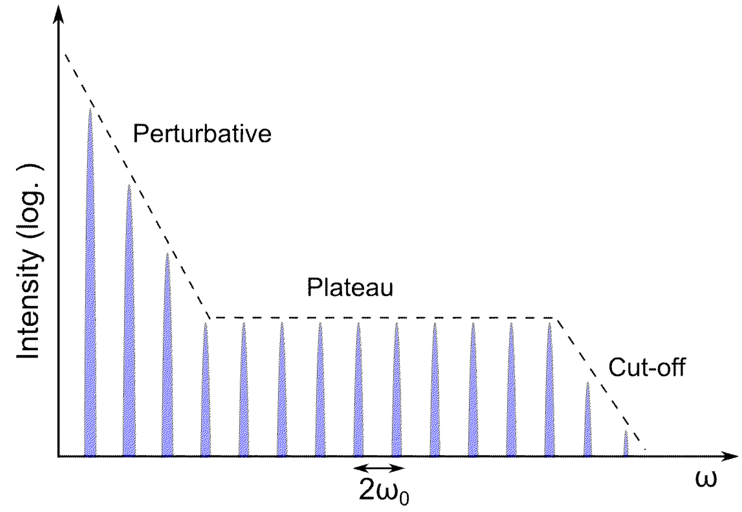

FIGURE 2.10: Typical spectrum of an HHG source.

the laser field. Computation of electron trajectories for different ionization time points showed that only electrons ionized in the first quarter cycle of the laser field can recombine and thus contribute to the HHG signal. The kinetic energy of the electrons can be computed as a function of ionization time and the maximum is found to be $3.18U_p$ where U_p is the ponderomotive potential. Therefore, the cut-off frequency(ω_c) of the HHG signal can be written as [94]

$$\hbar\omega_c = I_p + 3.18U_p \qquad \text{where} \quad U_p = \frac{e^2E_0^2}{4m_e\omega_0^2} \tag{2.33}$$

where e and m_e are the electron charge and mass respectively, E_0 is the electric field strength and ω_0 is the frequency of the driving laser. From Eq. 2.33, one approach to increase the cut-off frequency is to use noble gases with a higher ionization potential. However, this comes at the cost of harmonic yield since the single atom response decreases as we go to lighter noble gases (from Ar to Ne, for example). Another approach can be seen if we rewrite U_p in Eq. 2.33 in terms of the optical intensity I as

$$U_p = 9.33\ I\ \lambda_0^2 \tag{2.34}$$

It can be seen from the above equation that either the intensity or central wavelength of the driving laser can be increased to generate photons with higher energy. Accumulation of ionization could limit the use of higher intensities for cut-off scaling and the duration of the pulses has to be short enough to avoid it. Using longer wavelength driving lasers also comes at a cost due to the experimentally observed λ^{-6} scaling of the HHG yield [96]. Therefore, a careful choice of noble gas target and laser parameters is necessary to achieve the desired flux at the XUV/soft X-ray photon energy of interest.

Besides the Abbe limit, the photon flux of the XUV/soft X-ray source determines the resolution in CDI techniques. This is because a diffraction fringe at a given spatial frequency has to be above the noise floor so as to contribute to the reconstruction. If the source flux is not high enough, increasing the exposure time doesn't result in better resolution because both the signal intensity and the noise floor are increasing. Alternatively, XUV/-soft X-ray flux of the source also determines the measurement time for a given resolution, especially for ptychography. Therefore, generating harmonics with higher efficiency is critical in an HHG process besides increasing the cut-off energy. Phase matching is an important condition that needs to be fully or partially fulfilled in generating harmonics with usable flux. Phase matching refers to the mechanism of compensating the mismatch between the phase velocities of the fundamental and high-harmonic fields so that photons generated at different points in space can add up coherently [97]. The phase mismatch, $\varDelta k$, in HHG using noble gas targets from a gas jet can be expressed as

$$\begin{aligned} \varDelta k &= q \cdot k_0 - k_q && \text{(2.35a)} \\ &= \varDelta k_n + \varDelta k_{pl.} + \varDelta k_{geo.} + \varDelta k_{int.} && \text{(2.35b)} \end{aligned}$$

where q is the harmonic order, k_0 and k_q are the wave-vectors of the fundamental and the q^{th} harmonic. The first two contribution to the phase mismatch, $\varDelta k_n$ and $\varDelta k_{pl.}$, are pressure dependent and originate from dispersion in the neutral gas atoms and the plasma [98]. In the HHG source used in this work, the driving laser is focused in front of a gas jet backed by a noble gas at pressures up to a few bars. This setup is known as gas-jet HHG and the third contribution for the phase mismatch, $\varDelta k_{geo.}$, is the Gouy phase shift around the focus. The last contribution is the intrinsic phase that the free electron wavepacket acquires after ionization and this term is intensity dependent. Provided that the fraction of atoms ionized doesn't exceed a certain critical value, the dispersion term will have a positive sign while the geometrical term is always negative for high q values. Thus, the first three terms can compensate each other by choosing an appropriate backing pressure. In general, the wave-vector mismatch can be minimized by an appropriate choice of backing pressure, focusing strength and proper placement of the gas jet along the optical axis. A detailed discussion of phase matching and absorption considerations in HHG can be found in [97–99].

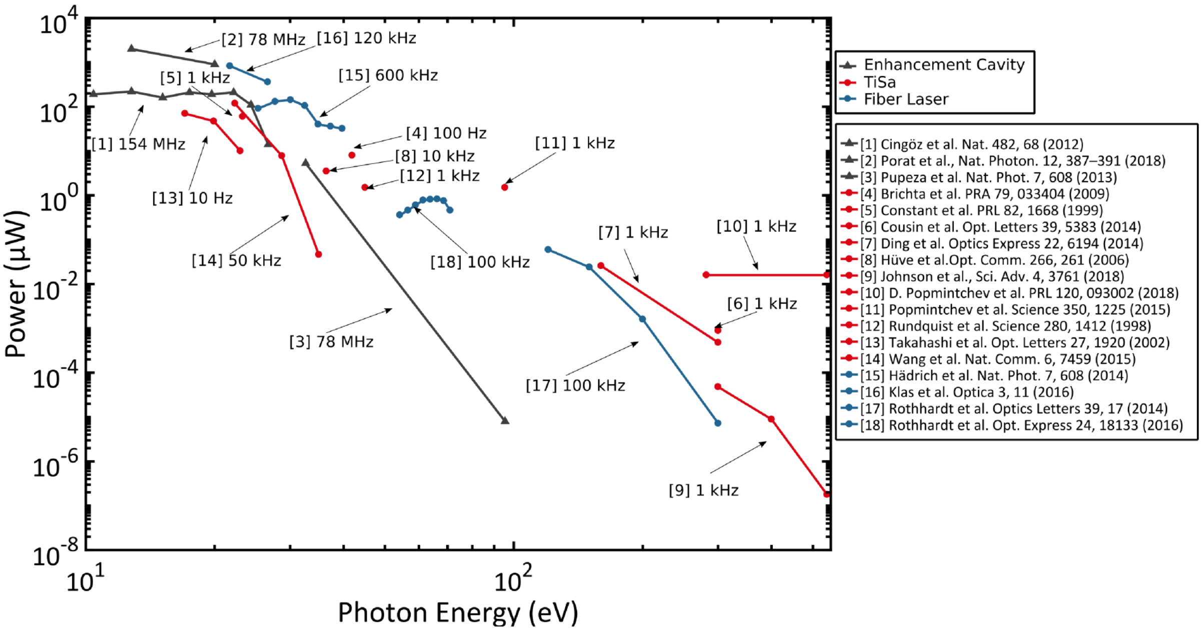

Figure 2.11: An overview of the performance of state-of-the-art HHG sources. The generated power is displayed per single harmonic line. The repetition rate and the corresponding reference for each source is also shown. Note that the citations in the figure only refer to the corresponding reference in the legend and not to the bibliography of this dissertation.

An overview of the highest flux HHG sources in the XUV spectral range are depicted in Fig. 2.11. It can be seen that fiber laser driven sources already generated more flux than established Ti:Sapphire based HHG sources for lower photon energies. Although Ti:Sapphire based HHG sources demonstrated the highest photon flux for higher photon energies, the scalability of fiber laser systems is expected to enable more flux in this spectral range in the near future. Note that other properties of the source besides photon flux e.g. temporal and spatial coherence, need to be taken in to account when comparing HHG sources for imaging applications. A fiber laser driven HHG source similar to reference 18 (according to the legend of Fig. 2.11) is used in this work although at reduced repetition rate for reasons to be explained in the following chapter. This source around 70 eV offers a good compromise between higher photon energy for better resolution and sufficient photon flux for successful imaging application.

Chapter 3

High Resolution CDI

As was briefly discussed in the first chapter, the main objective of this work is to demonstrate high performance diffractive imaging using HHG sources and achieve record-high resolution in different CDI modalities. A detailed discussion of the XUV source used in this work, the imaging setup and results for isolated transmission samples will be the main topics of this chapter. In the first section, the setup and characterization of the high photon flux 70 eV HHG source is presented together with the high power fiber laser system used to drive it. The imaging setup and spatial characterization of the XUV beam is discussed in the next section. These discussions cover the overall setup of the system shown in Fig. 3.1. A sub-wavelength CDI experiment demonstrating record-high resolution for table-top systems is detailed in section 3.3. In the final section, a new CDI-based beam characterization technique applicable for focused XUV/X-ray beams is proposed and a proof-of-principle experiment is presented.

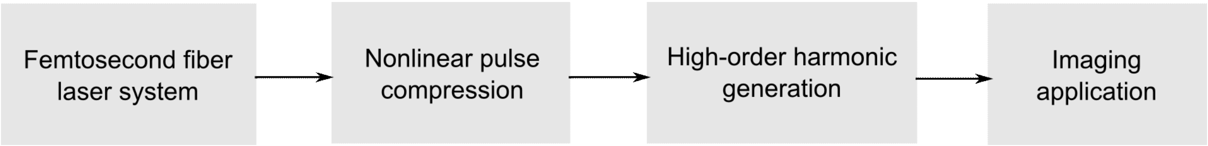

FIGURE 3.1: Overall system block diagram.

3.1 High Photon Flux XUV Source at 70 eV

Throughout this work, a table-top source based on HHG generating coherent flux mainly around 18 nm (68.6 eV) is used. For our driving laser parameters and HHG geometry, this was the shortest wavelength where the photon flux necessary for high speed and high resolution imaging can be generated. In the next subsection, the high power laser system that drives the HHG process together with mechanisms for reducing beam pointing fluctuation are discussed. This is followed by the detailed description of the gas jet HHG source, optimization of photon flux and spectral characterization.

3.1.1 High power femtosecond fiber laser system

Generation of XUV photons using HHG require laser systems that are able to deliver peak powers in the range of $10^{14}\ W/cm^2$. Over the past decade, fiber chirped pulse amplification (FCPA) systems were shown to deliver high peak power femtosecond pulses at high repetition rate mainly due to their ability to handle high average powers and novel fiber design for increased mode field diameter [100, 101]. Further scaling of their pulse energy was achieved by coherent combination of the output of multiple parallel fiber amplifiers [102]. This approach, known as coherently combined FCPA (CC-FCPA), recently demonstrated kW-level femtosecond laser system with mJ-level pulse energy and excellent beam quality by using eight parallel amplifier channels [103]. In this work, a two channel CC-FCPA system was used to generate femtosecond pulses with mJ-level energy and few tens of kHz repetition rate. A schematic diagram of this laser system is shown in Fig. 3.2 and is similar to that reported in [100, 104].

A femtosecond fiber oscillator spliced with a fiber integrated pre-amplifier gives pulses at 1030 nm central wavelength and 19 MHz repetition rate. A stretcher based on dielectric grating stretches the pulses to few nanosecond durations followed by a spatial light modulator for pulse shaping (Fig. 3.2). A series of fiber coupled pre-amplifiers amplify the pulses and the integrated acousto-optic modulators were used to reduce the repetition rate to the desired value. A large pitch fiber (LPF) amplifier [101] further amplifies the pulses to $\sim 60\ \mu$J of pulse energy at a repetition rate of 30 kHz to 35 kHz. The pulses were then split into two beam paths by a polarization beam splitter (PBS) and used as a seed for the main amplifiers. Each of the two LPF amplifier channels deliver ~ 0.6 mJ of pulse energy and their output was combined by a thin film polarizer (TFP). In the

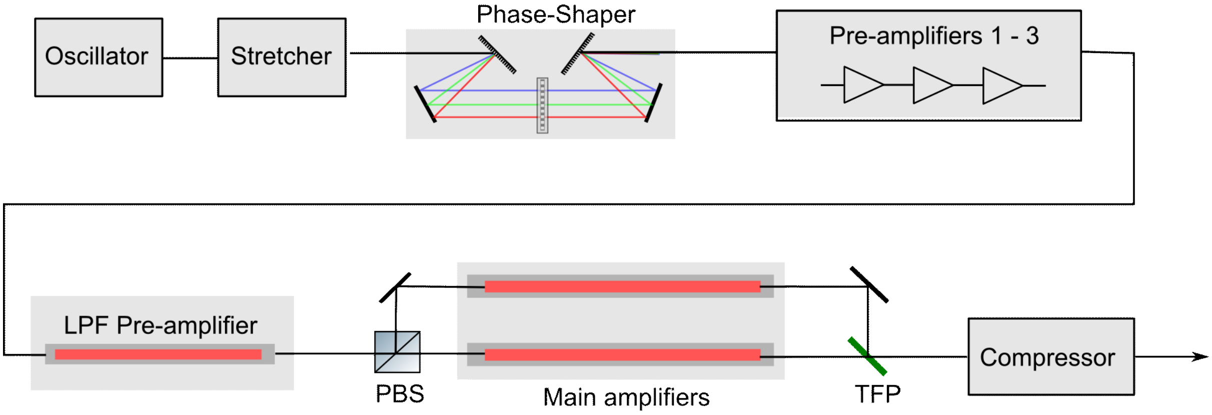

FIGURE 3.2: A schematic diagram of the coherently combined fiber CPA system.

last step, a grating compressor compresses the output pulses to ∼ 300 fs duration with an energy of ∼ 1 mJ.

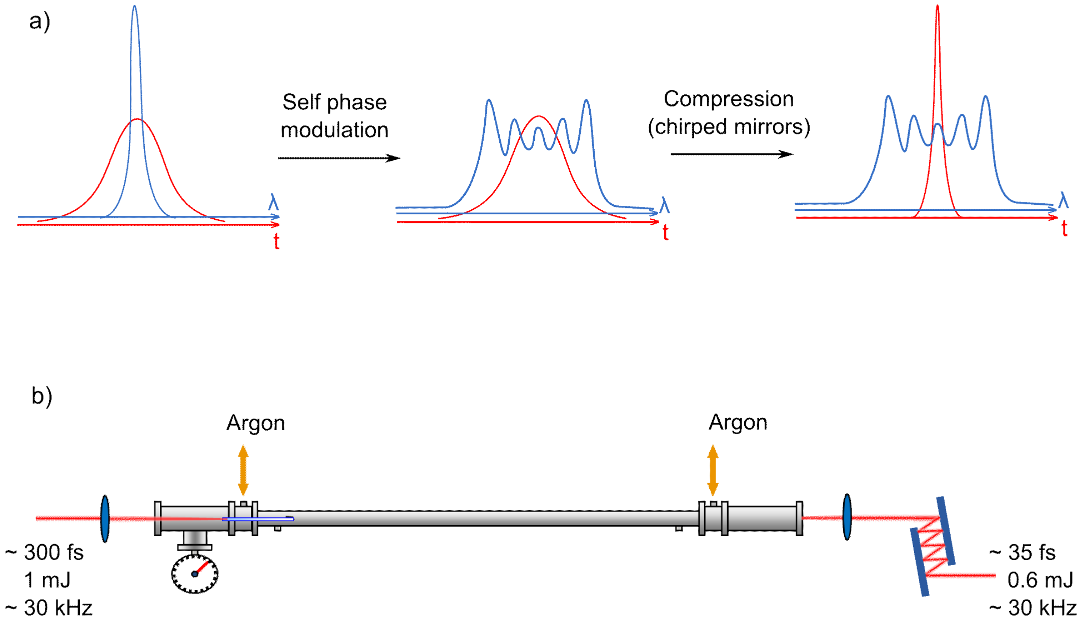

FIGURE 3.3: (a) The principle of nonlinear compression. (b) The hollowcore compression stage used in this work together with the input and output pulse parameters.

Pulses from the CC-FCPA were not short enough to be used for efficient HHG and further pulse compression was therefore necessary. This was accomplished by a nonlinear compression technique illustrated in Fig. 3.3(a). It is based on self phase modulation (SPM) of a high intensity pulse as it propagates through a nonlinear medium that results in spectral broadening. It is then followed by the use of dispersive elements (e.g. chirped mirrors) to remove the chirp introduced during SPM which gives pulses with a much shorter duration [105, 106]. In this work, a hollow-core fiber (HCF) filled with noble gas followed by multiple bounces from a pair of chirped mirrors was used for nonlinear compression (Fig. 3.3(b)). An HCF with a core diameter of 250 μm filled with argon gas at a pressure of $\sim$2 bars was used to compress the pulses from the CC-FCPA system to $\sim$ 35 fs of pulse duration. The transmission of the HCF compression stage was 60 % resulting in 0.6 mJ pulses at 35 kHz repetition rate. This laser system is used to drive the HHG process and it already delivers an order of magnitude more power than established Ti:Sa based driving lasers for HHG [107]. In addition, this fiber laser system has the advantage of being average/peak power scalable compared to other solid state laser architectures. The scalability of the driving laser power, and therefore the HHG flux, is mainly due to the suitability of fiber lasers for coherent combination of multiple amplifier outputs [100] which recently demonstrated $>$ 3 kW of average power [90].

Efficient coupling of the high intensity pulsed beam into the HCF compressor is quite sensitive to beam pointing instabilities. Small pointing fluctuations can lead to reduced transmission, bad beam quality and fluctuations of the output pulse duration. In addition, the HHG process also requires stable beam pointing of the IR beam for stable pointing of the generated XUV beam and small temporal fluctuations of the photon flux. Therefore, a beam stabilization (BS) system was incorporated in the beam path for position and angular stability. A commercial system (TEM Messtechnik) was used in this work and the basic arrangement is depicted in Fig. 3.4. The BS system consists of two motorized mirrors (M1 and M3), a position sensitive detector (PSD) and a feedback control module with connection to a computer. The beam is sampled from the leakage through mirror M4 and its positioning is determined by the PSD. There are two detectors in the PSD (right side of Fig. 3.4), one for xy position (P) and another for the angle (A). The beam position (xy and angular) is sent to the control module which in turn sends a feedback to the motorized mirrors so that the positioning of the beam is fixed to a given point of the 'A' and 'P' detectors. One such BS system was used before the HCF compression stage and enabled a stable transmitted power through the HCF with an excellent beam profile. A second BS system before the HHG setup (to be discussed next) also resulted in a more stable XUV flux and improved beam pointing. In addition to eliminating long term beam drifts, the pointing fluctuation at the focus of the IR beam after the second BS system was $< 2\mu$rad in angle and $< 4\mu$m in position over a 2 minutes time period.

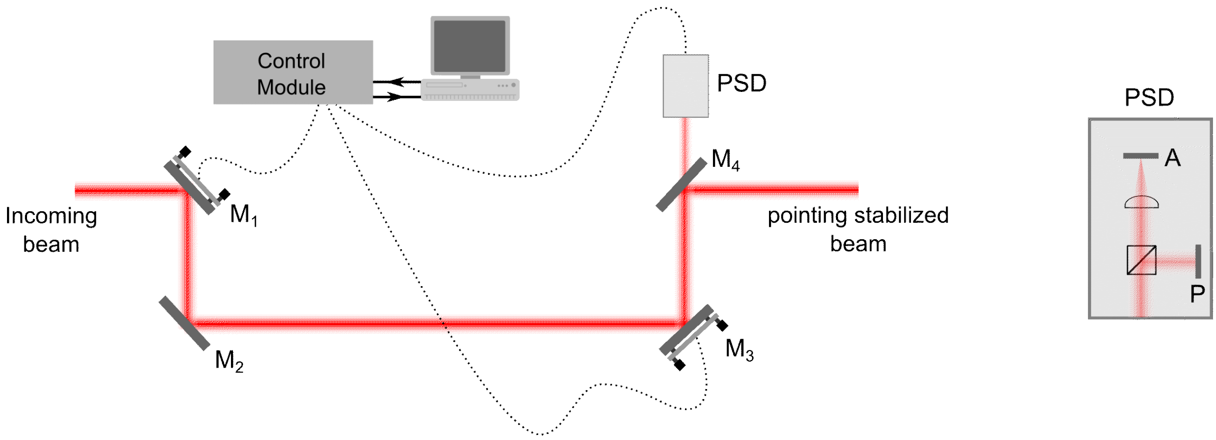

FIGURE 3.4: Setup of the beam stabilization system used in this work. The PSD (shown on the right) consists of a beam splitter and two detectors (angle and position). The angle detector 'A' is placed at the focus of a lens to convert angular shifts to position changes.

3.1.2 High-order harmonic generation setup

Pulses from the HCF compressor were short enough to be used for driving the HHG process. Since XUV photons are highly absorbed in air, the HHG setup and the subsequent imaging experiments were performed inside a vacuum chamber. Noble gas targets from a gas jet provide the nonlinear medium and the setup is shown in Fig. 3.5. To reach the required intensity for efficient HHG, the pulsed beam was focused in front of the gas jet using a lens with a focal length of 250 mm. The beam size before the focusing lens was 6 mm and the FWHM beam diameter at the focus was 50 μm. Assuming the pulses have a Gaussian shaped spatial and temporal profile, the peak intensity at the focus becomes 3×10^{14} W/cm^2. The generated XUV light co-propagates with the driving laser and it has to be separated so that we can use it for imaging applications. This issue of IR/XUV separation is not straightforward because of the large differences in power levels between the IR (tens of watts) and the XUV ($< 1\ \mu$W). A pair of grazing incidence plates (GIPs) together with metal filters were used as separation elements in this work. GIPs are glass plates that are anti-reflection coated for the driving wavelength (1030 nm) and aligned at grazing incidence (angle of incidence close to 90°) [108]. The driving laser beam is mostly transmitted while the XUV beam is Fresnel reflected due to the high incidence angles. At 70 eV, the GIPs have a combined reflectivity of 40% when put at 82° of angle of incidence. The remaining IR beam ($<$ 1W of average power) was absorbed by a 200 nm thick Al filter that has a transmission of 72% at 70 eV. Neither the GIPs nor the Al filters introduce large wavefront distortions in the XUV beam which is critical for imaging applications.

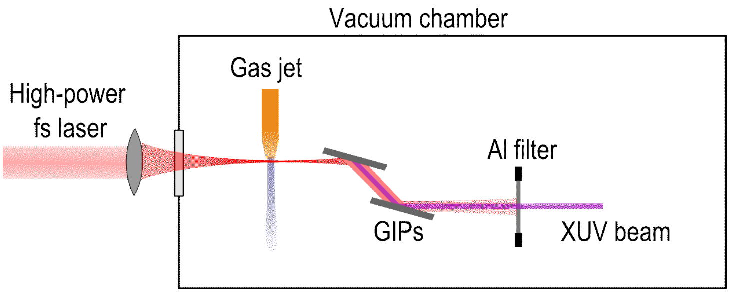

FIGURE 3.5: A schematic diagram of the HHG setup.

As discussed in Eq. (2.33) and (2.34), the cutoff photon energy in HHG is determined by the noble gas target, intensity (with pulse duration) and driving wavelength. For our driving laser parameters, argon gas offers the best compromise between cutoff photon energy and generated photon flux. Gas jets with opening diameters from 200 μm to 600 μm delivering argon at few bars of backing pressure were used in the different experiments performed. The jet diameters were chosen based on the guidelines for optimal HHG [99] so that the flux is mainly limited by re-absorption in the vacuum chamber and the gas load on the vacuum pumps. In addition, the peak intensity and Gouy phase at the IR focus is controlled for better phase matching by an aperture located before the focusing lens (Fig. 3.5). An iterative optimization of the aperture opening, the backing pressure and the position of the gas jet relative to the IR focus was performed for the highest photon flux.

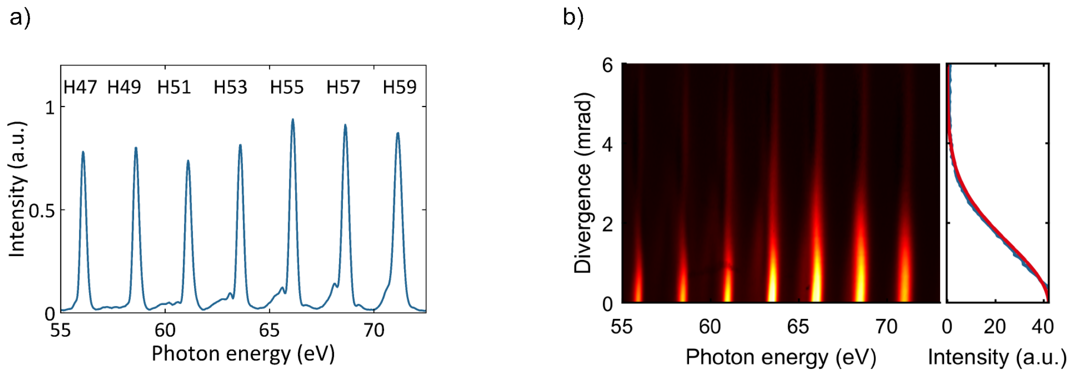

FIGURE 3.6: (a) Spectral intensity and (b) divergence of the generated harmonics.

The spectral and spatial properties of the HHG source were characterized by a flat field grating spectrometer consisting of a grating (1200 lines/mm) and a CCD camera. The spectra were calibrated using the absorption edge of Al at 72.5 eV and the results are shown in Fig. 3.6. The generated harmonic spectrum spans the photon energies up to 71 eV but only the last few harmonics are shown for convenience. Fig. 3.6(a) shows clearly separated harmonic lines with comparable intensity and narrow line widths. The relative bandwidth of the 57^{th} harmonic (68.6 eV or 18 nm), for example, was found to be $\sim$1/200 in optimized cases. The generated photon flux at 68.6 eV is estimated from the total counts to be $\sim 10^{10}$ photons/second at a repetition rate of 35 kHz. In doing so, the GIP reflectivity, metal filter transmission, grating efficiency and sensitivity (with quantum efficiency) of the CCD were taken into account. The divergence of the harmonic lines (Fig. 3.6(b)) was measured to be $\sim$ 5 mrads and the integrated profile on the right shows a Gaussian-like behavior. At a repetition rate of 100 kHz, this HHG setup generated a photon flux of $\sim 10^{11}$ photons/second per harmonic which is the highest from any HHG source in this spectral region [17, 104]. Lack of components for separation of the generated harmonics from the driving laser at high powers hindered usage of these higher repetition rates in the current work. The recently demonstrated scaling in average power to multi-kW levels is expected to increase the HHG flux by two orders of magnitude when combined with the development of efficient XUV/IR separation techniques [109]. This source will enable even more significant improvements in imaging performance than the record-high resolution and fast imaging results to be discussed next.

3.2 CDI Experiment with Sub-wavelength Resolution

Because it avoids imaging optics between the sample and detector, CDI enabled ultrahigh resolutions both at large scale facilities and HHG sources. Takahashi et al. demonstrated resolution of 2 nm for thick samples using hard X-rays at $\sim$ 0.1 nm wavelength while Chapman et al. performed the first single-shot CDI at a soft X-ray FEL source [7, 110]. Seaberg et al. showed that table-top CDI can also achieve high resolution of 22 nm using an HHG source together with the possibility of extracting 3D information [12]. The first sub-wavelength CDI experiment with a resolution of 0.8λ was demonstrated by Zürch et al. using an HHG source at 33.2 nm wavelength [111]. In addition, single-shot CDI which is interesting for time-resolved investigations was demonstrated with a moderate resolution of 119 nm using an HHG source [112]. While these table-top CDI results were performed in the transmission geometry, moderate resolutions of $<$ 1 μm were demonstrated in the reflection geometry which is relevant for applications e.g. semiconductor mask inspection [113, 114]. In this work, a CDI experiment with a half-pitch resolution of 13 nm which represents the highest resolution for table-top setups [87] is presented.

3.2.1 Experimental setup

As discussed in section 2.2, the allowed size of the exit wave in CDI techniques is limited by the oversampling and far field criteria. As a result, the beam from the HHG source has to be focused into a small area which also increases the photon flux available for imaging. For conventional CDI in particular, focusing was necessary also because the wavefront is assumed to be flat in the reconstruction algorithms and this is fulfilled only at the focus of the XUV beam. The overall imaging setup is depicted in Fig. 3.7 and uses two spherical multilayer mirrors to focus the XUV beam onto the sample. Refractive optics is not available for the XUV spectral range and zone plates are lossy as well as inconvenient for typical collimated XUV beam sizes ($\sim$ 10 mm). The diffracted field was then recorded with a CCD detector and the central bright section of the diffraction pattern can optionally be blocked by a beam stop. While CDI requires a small spectral bandwidth, the HHG source discussed in the previous section delivers multiple harmonics from 30 eV to 71 eV. Spectral filtering was therefore necessary before using the source for CDI applications. The multilayer mirrors in Fig. 3.7(a) are designed to reflect the desired photon energy (68.6 eV) and filter out all other harmonic orders in addition to focusing the beam. The mirrors (available from optiX fab.) have a peak reflectivity of 50 % each at 68.6 eV for normal incidence. Their energy bandwidth is 2.2 eV and suppresses the neighboring harmonics by two orders of magnitude after two reflections. The filtered spectrum after the multilayer mirrors is shown in Fig. 3.7(b).

The first mirror (focal length of 1.2 m) of Fig. 3.7(a) collimates the beam while the second one (focal length of 0.5 m) focuses it onto the sample. This arrangement offers a demagnification of the source point by a factor of two. Due to the off-axis arrangement, the focusing setup introduces astigmatism to the focused beam. Since the astigmatism

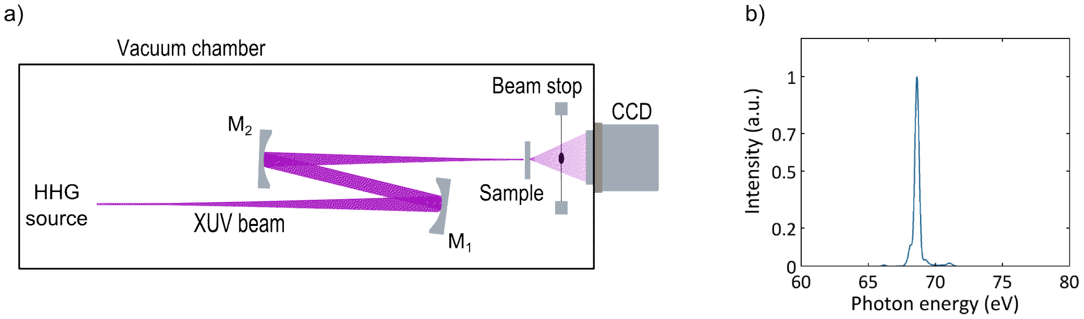

FIGURE 3.7: (a) Schematic diagram of the imaging setup. (b) Spectrum of the HHG beam after filtering by the two multilayer mirrors.

gets worse for larger angles of incidence (AOI), the mirrors were positioned for the smallest AOI by increasing their on axis (along the z-axis) separation allowed by the size of the vacuum chamber. In addition, the smallest possible separation along the x-axis was used and this was limited by the diameter of the XUV beam on the first multilayer mirror (Fig. 3.8(a)). A scan across the XUV focus was simulated for the parameters shown in Fig. 3.8(a) using the optical design software Zemax. The spot diagram for the z range of ± 100 μm is shown in Fig. 3.8(b) and a slight change in beam profile from vertical elongation to a horizontal one can be observed. The beam profile gets a pronounced elongation at deviations of 500 μm both before and after the focus (Fig. 3.8(c)). These highly elongated profiles can be problematic for CDI since the beam might not have uniform intensity all over the sample. The focal point along x and that along y occur at different points along the propagation direction separated by about 1 mm. In between the two foci, the beam has comparable focal diameters along x and y which is taken as the overall focus (at $z = 0$ in Fig. 3.8(b)and (c)). The phase profile is also expected to be strongly curved at these points which also violates the main assumptions in CDI. Therefore, the sample was always positioned as close as possible to the focus (both longitudinally and transversally) by maximizing the flux through a small pinhole. The highly elongated profiles of Fig. 3.8(c) bring a different challenge for ptychographic CDI which will be discussed in chapter 5.

To estimate the size of the XUV focus, a 1 μm pinhole was scanned across it and the transmitted intensity was integrated. This revealed a full width at half maximum (FWHM) focal diameter of 10 μm. The XUV beam recorded with a CCD at the far field of the focus (Fig. 3.9(a)) shows a good beam quality with a Gaussian-like profile. Note that

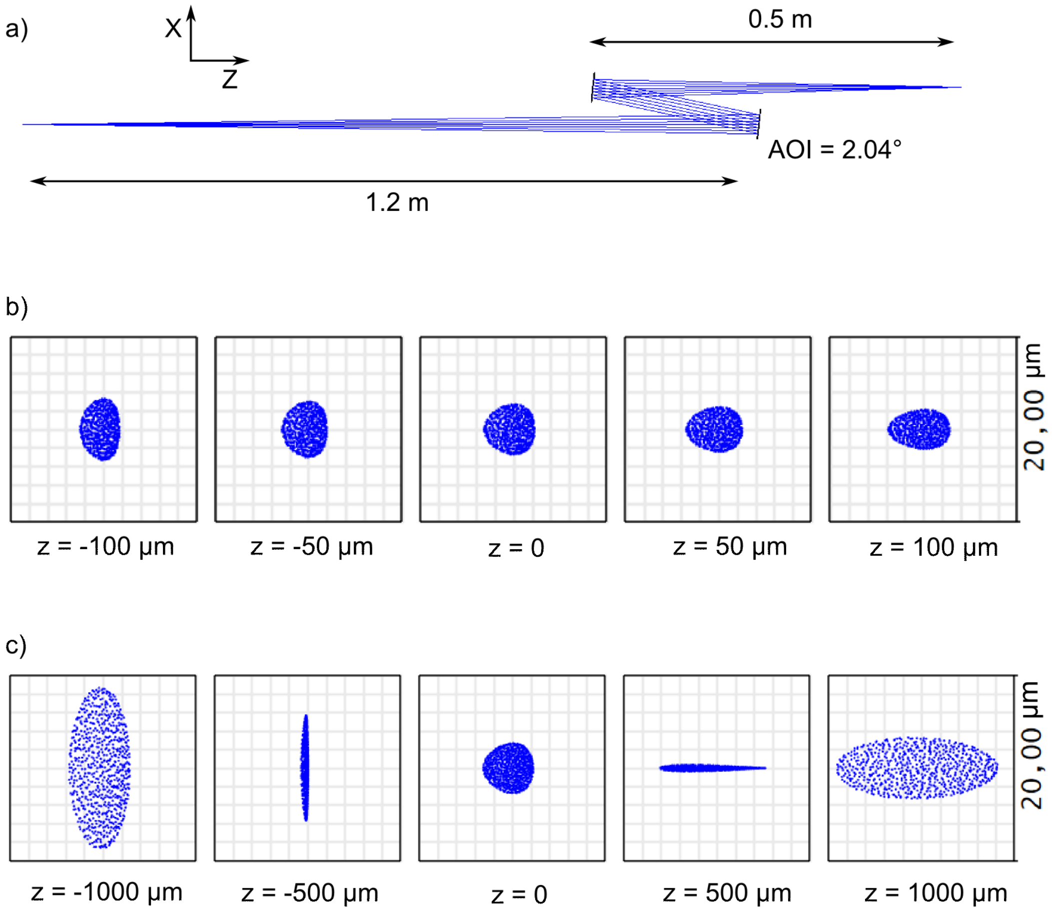

FIGURE 3.8: Simulation of the imaging system using Zemax. (a) The layout of the mirrors and dimensions used in the simulation. Through-focus spot diagram at (b) 50 μm steps around the focus and (c) 500 μm steps around the focus.

both the photon flux and the beam profile can be optimized by varying the HHG parameters (intensity, gas jet position, backing pressure, ...). To have a measure of the spatial coherence of the beam, a double slit with a 1.5 μm separation was placed at the XUV focus and its fringe visibility was analyzed. It was placed as a sample at the XUV focus (Fig. 3.7(a)) and the far field diffraction was recorded by a CCD placed 20 mm away. The measured diffraction pattern (Fig. 3.9(b)) and its cross section (Fig. 3.9(c)) show clear fringes with a visibility of 90 %. This means that two wave fields diffracted from features at the opposite ends of a 1.5 μm sized sample can interfere with 90 % visibility. This demonstrates the HHG source has a high degree of spatial coherence that is essential for CDI applications.

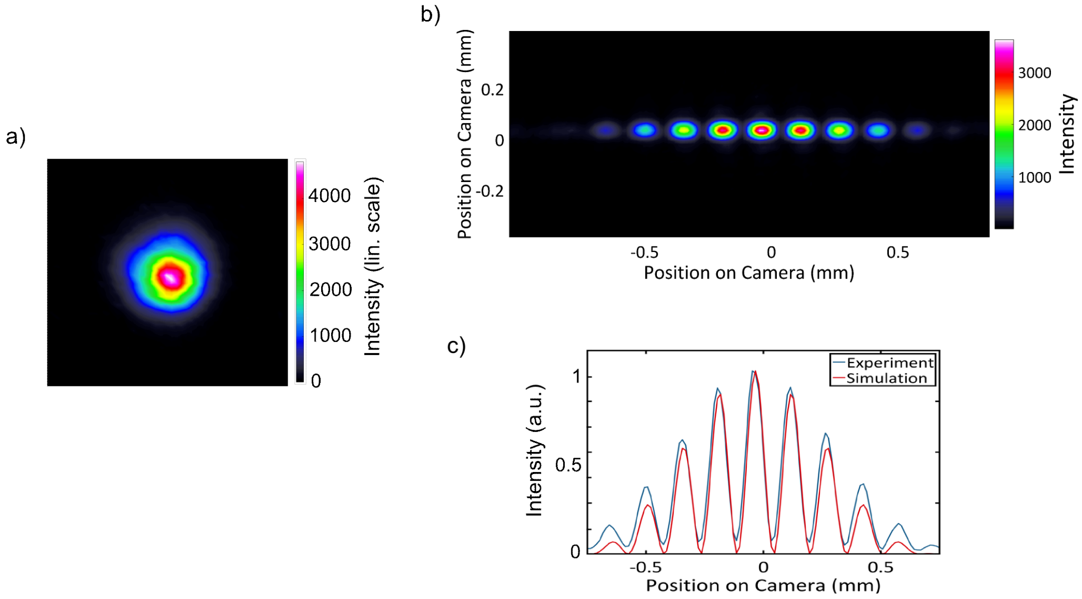

Figure 3.9: Beam profile and spatial coherence. (a) Far field beam profile of the XUV beam (at a distance of 13.6 mm from the focus). Window size is 0.6 mm by 0.6 mm. (b) Diffraction pattern from a double slit with 1.5 μm separation. (c) Comparison of a horizontal cross-section across the center of the diffraction pattern in (b) with a simulation for a perfectly spatially coherent source.

3.2.2 Imaging results

Data acquisition

The transmission sample shown in Fig. 3.10(d) was fabricated by FIB milling the desired features into 50 nm silicon nitride membrane and thermally evaporating 150 nm of gold layer on top. It was placed at the focus of the XUV beam to have an illumination with a flat wavefront and the maximum available photon flux for imaging. It has an overall size of 1 μm which is smaller than the double slit used for characterizing the spatial coherence. Therefore, a fringe visibility greater than 90 % is expected between opposite edges of the sample's features. Diffraction patterns were acquired using an XUV CCD camera (Andor iKon-L) having 2048 by 2048 pixels with a pixel size of 13.5 μm. The sample was placed as close as possible to the camera to achieve the highest NA. The sample-camera distance was 13.6 mm and it was limited by physical constraints of the sample holder and vacuum chamber. For the size of the XUV camera, this gives an NA of 0.71 which can be fully exploited if the photon flux is high enough. Using Eq. 2.12, the resolution limit from the NA of the setup (the Abbe limit) is 11.7 nm. As explained in Eq. 2.32, the achievable resolution in CDI is also limited by temporal coherence for a given sample size and oversampling degree. The maximum oversampling degree for the sample size and sample-camera distance is 18. Although a higher oversampling degree results in robust reconstruction, the signal to noise ratio (SNR) of the measurement can be increased if the neighboring pixels are summed up (binned) together. A total of 8×8 pixels were binned together on-chip for the measurement thereby reducing the oversampling degree to 2.3 without affecting resolution. The resolution limit due to temporal coherence is then calculated to be 11.5 nm for the relative bandwidth ($\Delta\lambda/\lambda$) of 1/200 and a 1 μm sample. Therefore, the resolution in our experiment was ultimately limited by the NA of the setup.

In diffraction measurements, the central (low spatial frequency) fringe usually has orders of magnitude higher intensity than the highest frequency components having fringes at the edge of the camera. Therefore, in measurements with moderate exposure times, the central pixels saturate at the highest count set by the bit depth of the camera (16 bit in this case). For even longer exposure times, the accumulated electrons in a pixel overflow to the neighboring pixels in what is known as blooming. These phenomena limit the dynamic range of a single measurement to about three orders of magnitude in the current setup. To extend the dynamic range, multiple measurements were taken with or without a central beam stop and subsequently merged together. The beam stop was made of borosilicate glass spheres with diameters of about 200 μm attached to an ultra-thin wire with 7.5 μm diameter. It was then placed between the sample and the camera as shown n Fig. 3.7(a). Three measurements with exposure times of 4 sec., 1 min. and 15 mins. were taken (Fig. 3.10 (a-c)) where a beam stop was used in the last two.

Data processing and reconstruction

The 4 sec. measurement captures the low spatial frequency information faithfully while the 15 min. measurement contains those at the highest spatial frequencies. The 1 min. measurement was used to find the correct scaling values in merging the diffraction patterns since the 4 sec. and 15 min. measurements only have a small region in common where both have a valid intensity value. In the first step, background subtraction and hot pixel removal was performed on all three diffraction patterns. In all three measurements, a mask was defined representing regions in the diffraction patterns with valid intensity values. These are regions where the diffraction is above the noise threshold for the 4

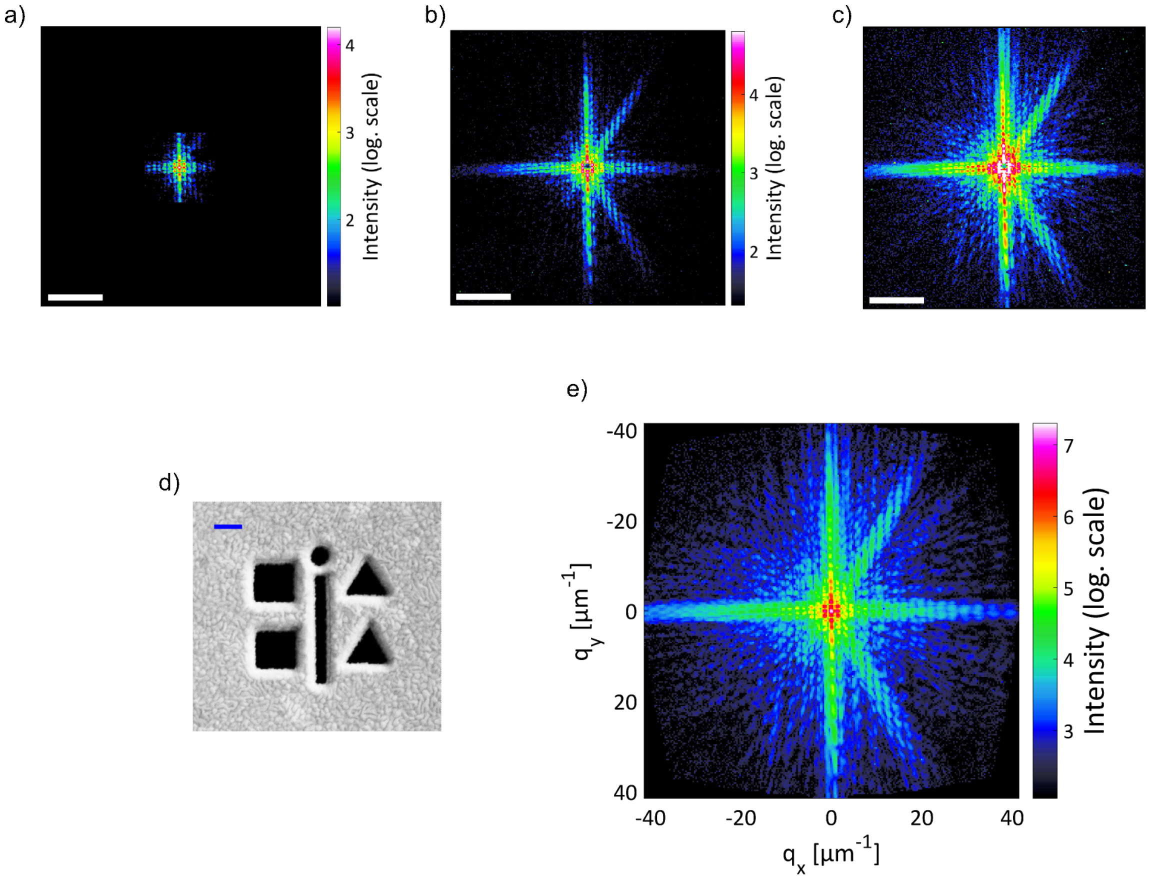

FIGURE 3.10: CDI sample and diffraction patterns. (a) Diffraction patterns acquired with exposure times of (a) 4 seconds, (b) 1 minute and (c) 5 minutes. Scale bar is 10 μm^{-1}. (d) Scanning electron microscope image of the sample (scale bar is 200nm). (e) A composite diffraction pattern obtained by merging diffraction patterns with exposure times from 4 seconds to 15 minutes.

sec. measurement. For the longer exposure times, the masked areas are those below the saturation count and outside the beam stop shadow (central regions of Fig. 3.10 (b) and (c)). In merging the 4 sec. and 1 min. measurements, the ratio between corresponding usable pixels (inside the mask) in both patterns was taken and the average of these ratios was computed to get the scaling factor between the two patterns. A simple ratio of the exposure times was found to be inaccurate potentially due to nonlinearities in the camera and small changes in photon flux of the source. A scaled version of the 4 sec. measurement then replaces the saturated and beam stop regions of the 1 min. measurement. An average between the 1 min. and scaled 4 sec. measurements was used in regions where both have valid intensities. A similar procedure was performed in merging the 15 min. measurement with the composite diffraction pattern of 4 sec. and 1 min. measurements. Due to the high NA of the measurement, curvature correction was performed on the composite diffraction pattern. The final diffraction pattern (Fig. 3.10(e)) has an increased dynamic range of more than seven orders of magnitude and the fringes extend up to the edge of the camera.

Image reconstruction was performed using the RAAR algorithm (β-parameter of 0.95) without any a priori information except that the sample is isolated. For more robustness, the guided version with multiple independent reconstructions and multiple generations was employed as discussed in section 2.2.2. The initial estimate for the support was taken by thresholding the autocorrelation of the sample (computed by the inverse Fourier transform of diffraction pattern) to 4% of its peak value. The support was then updated every 50 iteration using the shrink-wrap algorithm. The evolution of the support every three updates (Fig. 3.11) shows that the centro-symmetry of the first estimate (autocorrelation) is broken in the first stages. Note that an overly tight update of the support shrinks the object estimate beyond its actual size and results in artificial ripple patterns in the image. Here, shrink-wrap was loosely applied by convolving a Gaussian function with the current object estimate and thresholding the result to 20% of the peak value. The reconstruction starts with 12 independent reconstructions each with 2000 iterations and the best one was selected by comparing the reconstruction error (Eq. 2.20). This reconstruction was mixed with all the rest and used as a seed for the second generation [41]. The same procedure was repeated for 20 generations after which the 12 reconstructions were quite similar. In mixing two reconstructions, a registration algorithm was used for accurate alignment within $1/20^{th}$ of a pixel [115] to account for the shift invariance of the phase retrieval algorithms.

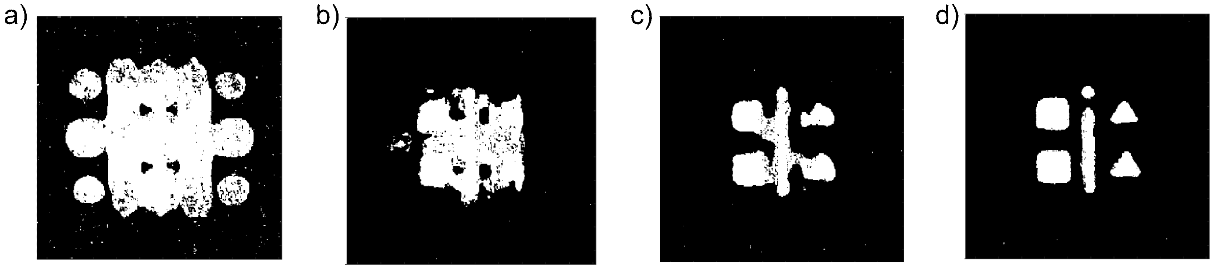

FIGURE 3.11: Evolution of the object support. (a) The initial support which is the autocorrelation. Support after (b) 150 iterations (c) 300 iterations and (d) 450 iterations.

The reconstructions in the last generation were aligned and averaged to give the final image. The amplitude and phase profiles of the reconstruction are displayed in Fig. 3.12 (a) and (b). The amplitude profile shows that all features of the sample are faithfully reconstructed. The phase profile of Fig. 3.12 (b) is shown for regions where the amplitude is above 5% of its peak value. The phase profile is flat as is expected from a pure amplitude sample where the transparent areas do not introduce any phase shift in the exit wave. Slight linear gradient can be observed from the bottom-left to the top-right corner of the phase profile that originates from a shift of the center of the diffraction pattern from the center of the detector. The intensity fluctuations (for example in the two squares of Fig. 3.12(a)) are reconstruction artifacts from the non-perfect measurement conditions. These are mainly the background noise, non-linearities of the detector and errors in merging multiple diffraction patterns. In addition, it is interesting to see that the central bar in the amplitude profile has two bright lines. This two-line feature is the result of waveguiding in the structure due to the high aspect ratio of this feature. Waveguiding effects will be discussed in more detail in the next chapter with the aid of numerical simulations. To estimate the achieved resolution, a cross-section along the edges of the reconstructed amplitude can be taken to perform a knife-edge test. The distance between the points where the amplitude is 10% and 90% of the maximum value is known as the 10-90 resolution. A cross-section along the white line at the lower square of Fig. 3.12(a) is shown in Fig. 3.12(c) and the 10-90 resolution value was found to be 13 nm.

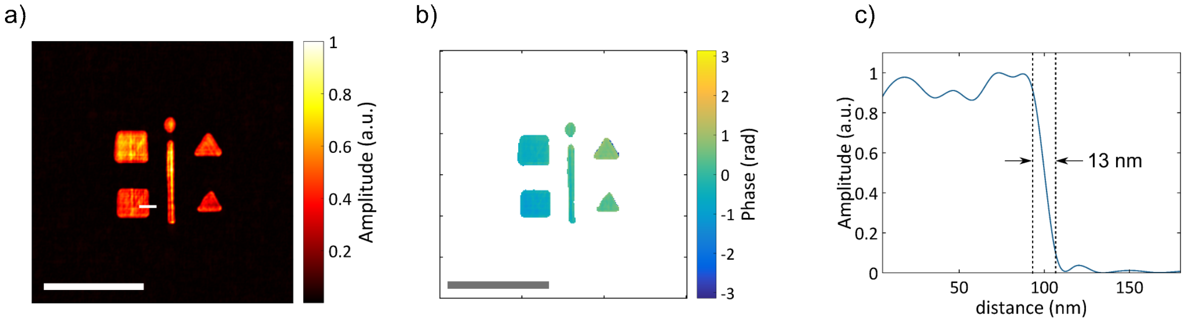

FIGURE 3.12: (a) Reconstructed amplitude. (b) Reconstructed phase. (c) Cross-section along the white line at an edge in (a). Scale bars in (a) and (b) are 1 μm in size.

Knife-edge test represents resolutions achieved across an edge of the object in a particular direction. In reconstructions where the support constraint is too tight, the reconstruction algorithm may give solutions that show sharp oscillatory behavior across an edge. A knife-edge test across these types of edges could result in 10-90 resolution values that overestimate the actual feature sharpness. An effective way of avoiding these issues is to use a criterion that represents the overall performance across the whole object. Phase retrieval transfer function (PRTF) is a Fourier space criterion that quantifies how faithfully the phase of the diffraction fringes is retrieved [27]. It gives a measure of the highest spatial frequency that contributes to the reconstruction and this can be interpreted into a real space resolution estimate. It is defined as

$$\mathrm{PRTF}(\mathbf{q}) = \frac{|\langle U_{rec.}(\mathbf{q})e^{i\phi_0}\rangle|}{\sqrt{I(\mathbf{q})}} \tag{3.1}$$

where $U_{rec.}(\mathbf{q})$ is the retrieved complex diffraction field (Fourier transform of the reconstructed object) and $\sqrt{I(\mathbf{q})}$ is the measured diffraction amplitude. PRTF computes the average of the reconstructed field over multiple independent reconstructions (12 in this case) and normalizes it to the measured amplitude. In doing so, a constant phase factor ϕ_0 is added to each retrieved field to compensate for differing constant phases between reconstructions. Diffraction fringes that don't have a consistent phase in multiple reconstructions vanish during averaging while those consistently retrieved retain their amplitude. The PRTF analysis for our reconstruction is shown in Fig. 3.13 (blue line). It shows the characteristic behavior of reduced PRTF for higher frequencies where phasing becomes less consistent due to reduced SNR. Since the diffraction intensity had good contrast until the edge of the detector (Fig. 3.10(e)), the PRTF is above 0.2 for almost all spatial frequencies. The half-pitch resolution is the feature size that corresponds to

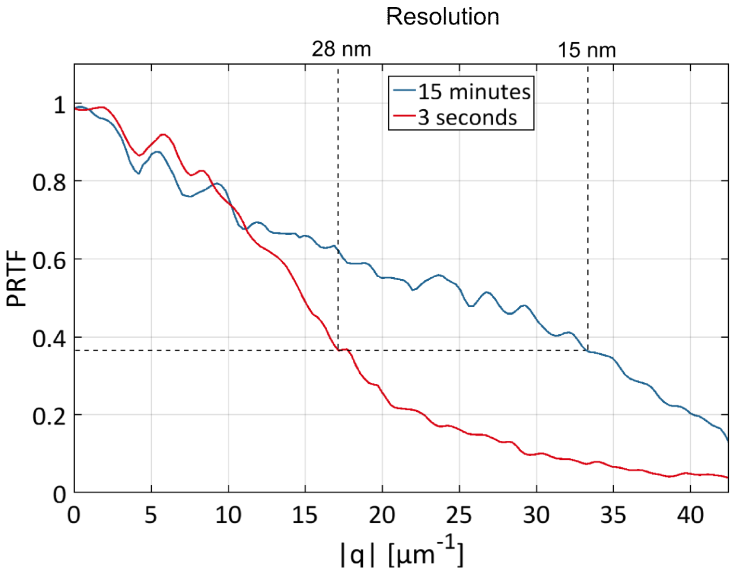

Figure 3.13: PRTF of the reconstruction for the short (3 seconds) and long (15 minutes) acquisition time measurements.

the highest spatial frequency with PRTF value above a certain threshold (commonly 1/e [110]). Spatial frequencies up to 33.2 μm^{-1} satisfy the PRTF 1/e criterion and the corresponding resolution is therefore 15 nm. This result is the highest resolution achieved for a table-top CDI setup and represents a factor of 2 improvement from previous results using the PRTF criterion [12].

Reconstruction with short exposure times

An equally important performance measure besides resolution is measurement speed. In this context, meaningful resolutions need to be achieved with short exposure times in order to have a reasonable overall measurement time. This metric is particularly critical for ptychography where multiple diffraction patterns have to be recorded to image a larger field of view. A single diffraction pattern with an exposure time of just 3 sec. is shown in

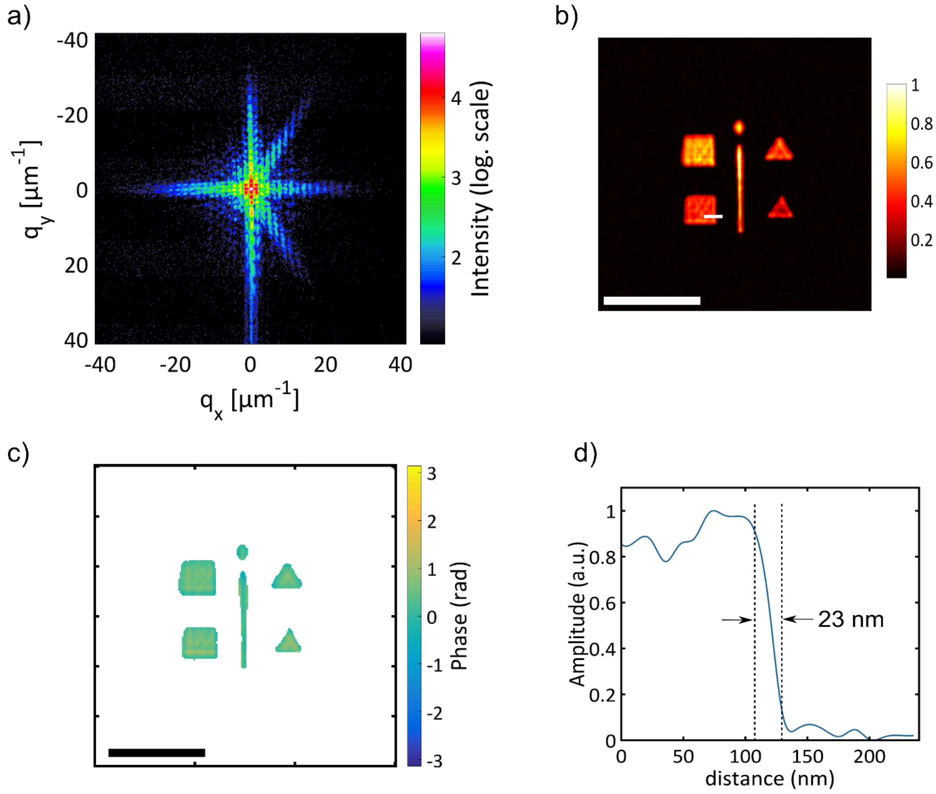

FIGURE 3.14: CDI result with a single short acquisition time measurement. (a) Recorded diffraction pattern with an acquisition time of 3 seconds. The reconstructed object (b) amplitude and (c) phase. Scale bars in (b) and (c) are 1 μm in size. (d) Cross-section along the white line at an edge in (b).

Fig. 3.14(a) where the fringes are above the noise floor until about half the detector. All other measurement parameters are the same as the high dynamic range result discussed previously. The guided RAAR algorithm was also used here for phase retrieval with 15 generations and 12 independent reconstructions. The reconstructed amplitude (Fig. 3.14(b)) shows that all features are clearly visible with good contrast. A cross-section along the white line in the lower square reveals a 10-90 resolution of 23 nm (Fig. 3.14(d)). The reconstructed phase (Fig. 3.14(c)) also shows the flat profile expected from a pure amplitude sample. The PRTF of the 3 sec. measurement is plotted in Fig. 3.13 (red line) and the resolution according to the PRTF 1/e criterion is 28 nm. This result demonstrates that achieving sub-30 nm resolution is possible using table top HHG setups with only few seconds of exposure time which qualifies it for high resolution ptychography and 3D tomography. It also represents a reduction of the required exposure time for previous results that achieved comparable resolutions on a table top setup [12].

3.2.3 Towards CDI at soft X-ray wavelengths

As it follows from the Abbe limit, a direct approach to scale the resolution of CDI setups is employing sources with shorter wavelengths. In addition, imaging using sources in the soft X-ray spectral range ($\lambda < 10$ nm) is interesting due to the presence of absorption edges that can be accessed for higher contrast. So far, table-top CDI setups used sources in the XUV spectral range mainly because the photon flux at shorter wavelengths was insufficient for CDI. In a first attempt towards CDI at soft X-ray wavelengths, high harmonics at 8 nm wavelength (150 eV photon energy) were generated using few cycle pulses where neon gas was used as a non-linear medium for HHG. A fiber CPA system together with two hollow-core fiber compression stages were used to deliver sub-10 fs pulses at 1 μm central wavelength with 0.25 mJ pulse energy at repetition rates of up to 150 kHz [16]. In the current experiment, the repetition rate was reduced to 43 kHz in order to avoid heating of the silver filters used for separating the generated harmonics from the driving infrared laser. The driving laser was focused by a pair of mirrors in front of a 150 μm diameter gas jet releasing neon at 9 bars of backing pressure for HHG. The generated spectrum was measured by a grating spectrometer and is depicted in Fig. 3.15(a). At 150 eV, a photon flux of $\sim 2 \times 10^8$ photons/(sec.*eV) were generated that corresponds to $\sim 3 \times 10^8$ photons/sec. in a 1% bandwidth.

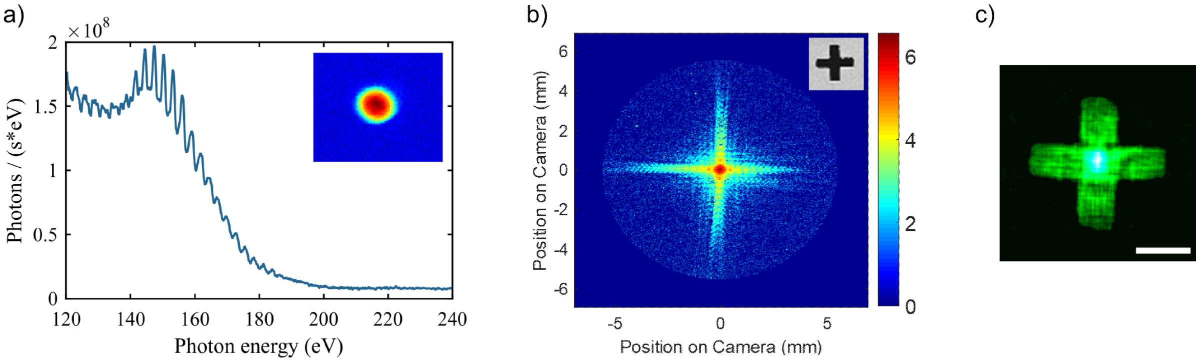

FIGURE 3.15: CDI at soft X-ray wavelengths. (a) Photon flux of the HHG source around 150 eV (8 nm). Inset shows the far-field profile of the beam at 8 nm wavelength. (b) Diffraction pattern acquired for a transmission sample shown in the inset. Overall size of the sample is 2.5 μm. (c) The amplitude of the reconstructed object (scale bar is 1 μm).

The imaging setup is similar to that depicted in Fig. 3.7(a) and two multi-layer mirrors with peak reflectivities of 33% at 150 eV (FWHM bandwidth of 1.4 eV) were used for focusing and spectrally selecting a single harmonic. The far-field beam profile of the harmonic at 8 nm (inset of Fig. 3.15(a)) shows an excellent Gaussian-like shape. The HHG flux at 150 eV is among the highest generated from table-top sources in this spectral range [17]. Although the overall transmission of the metal filters and multi-layer mirrors is $\sim$ 5%, the flux combined with the excellent beam quality was sufficient for demonstrating the feasibility of CDI at soft X-ray wavelengths. A simple transmission sample (inset of Fig. 3.15(b)) fabricated by focused ion beam milling of a 200 nm copper coated Si_3N_4 membrane was used in the experiment. A composite diffraction pattern (Fig. 3.15(b)) with higher dynamic range was obtained by merging measurements with 2 seconds, 30 seconds and 15 minutes. The reconstruction was performed using the RAAR and shrink-wrap algorithms that were already used in the 68.6 eV result presented earlier. The reconstruction (Fig. 3.15(c)) was successful although the quality is lower and the resolution is limited by the available flux to $\sim$ 50 nm (half-pitch). After this experiment was conducted, the average power of the few cycle laser was increased by more than one order of magnitude [116]. Together with novel methods for separation of generated harmonics from the driving infrared laser [109], imaging at 150 eV can deliver significantly improved image quality and resolution.

3.3 CDI-based Wavefront Sensor

3.3.1 Principle of operation

The application of CDI discussed so far is in imaging of an unknown isolated sample assuming that the illuminating beam has a flat amplitude and phase profile. This follows from the principle of CDI (section 2.2.1) where the exit surface wave (ESW) is the profile that is reconstructed in real space. The ESW itself is a product of the sample complex transmission function and the illuminating beam profile in the projection approximation. This means if a sample with a known transmission function is used, CDI can also be applied in extracting the amplitude and phase profile of the illuminating beam. In the following, this idea is used to develop a wavefront sensor for characterizing XUV beams at focus and a proof-of-principle experiment in the visible spectral range is presented. First indication of the feasibility of an XUV wavefront sensor was observed when an extended periodic grid of pinholes was used as a CDI sample (Fig. 3.16(a)). Measurements at three different on-axis points along the XUV focus were taken and the reconstructions (Fig. 3.16(b)) show sections of the pinhole grid with the correct period. More interesting is the profile of the reconstructed area that is elongated vertically at z = -2.25 mm, becomes symmetric at zero and then elongated horizontally at z = 2.25 mm. This progression follows that of the astigmatic beam already simulated using Zemax (Fig. 3.8).

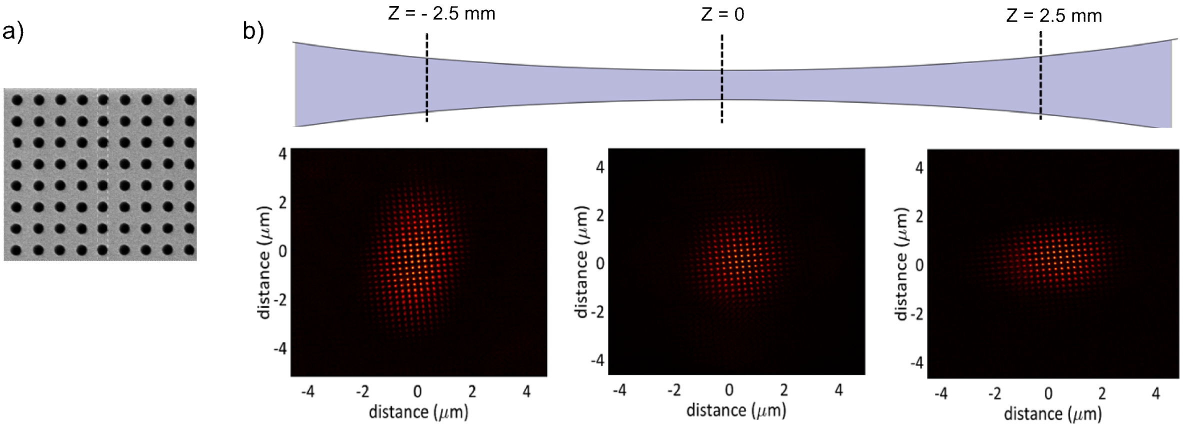

FIGURE 3.16: Performing a CDI experiment on an extended sample. (a) Layout of the sample which is a grid of pinholes with 100 nm diameter (200 nm pitch). The overall sample size is 25 μm × 25 μm. (b) Amplitudes of CDI reconstructions at three planes across the focus of the XUV beam.

The reconstructed pinholes also have higher transmitted intensity in the center which is expected from a focused illuminating beam. Since the sample has a uniform transmission (T = 1) at the pinholes and zero transmission outside, what is reconstructed is the XUV beam profile sampled by the pinholes at a particular plane. A 2D amplitude and phase profile of the XUV beam can then be extracted by interpolating between the reconstructed pinholes.

Beam characterization using an extended periodic grid, however, has some issues that could make the results unreliable. These are

- The size of the reconstructed area is determined by the threshold used in the shrink-wrap algorithm. If a higher threshold is used, the reconstructed area will get smaller since the outer pinholes will be out of the support. The central reconstruction in Fig. 3.16(b), for example, has a FWHM size of $\sim 3\ \mu$m which is smaller than the estimated size of 6 μm for the current experimental setup.
- It is difficult to limit the illuminated area which could be larger than the size allowed by the far-field criterion of Eq. 2.9. In cases where the beam is larger than that allowed by the far-field criterion, the diffraction pattern is not taken in the far-field and the reconstruction fails.
- The twin-image problem already discussed in section 2.2.2 where two possible reconstructions are valid for a given diffraction measurement. So the actual beam orientation cannot be known and, in the worst case, a mixture of the two orientations could be reconstructed.

A reliable wavefront sensor can be developed by modifying the design of the sample (referred to as mask from now on) so that each of the above issues are dealt with. The validity of the far-field criterion can be insured by limiting the size of the transmitting region of the mask to a range where the far-field condition is fulfilled. The beam will then be characterized within the area covered by the designed mask. The challenge in choosing the shrink-wrap threshold can be solved by having a fixed support from the mask design (SEM image) thereby avoiding the shrink-wrap algorithm altogether. This also makes the reconstructions much faster. The twin image and beam orientation problems can also be addressed by having a non-centrosymmetric mask where a reconstruction and its complex conjugate are different. In this case, the orientation is clearly identifiable and

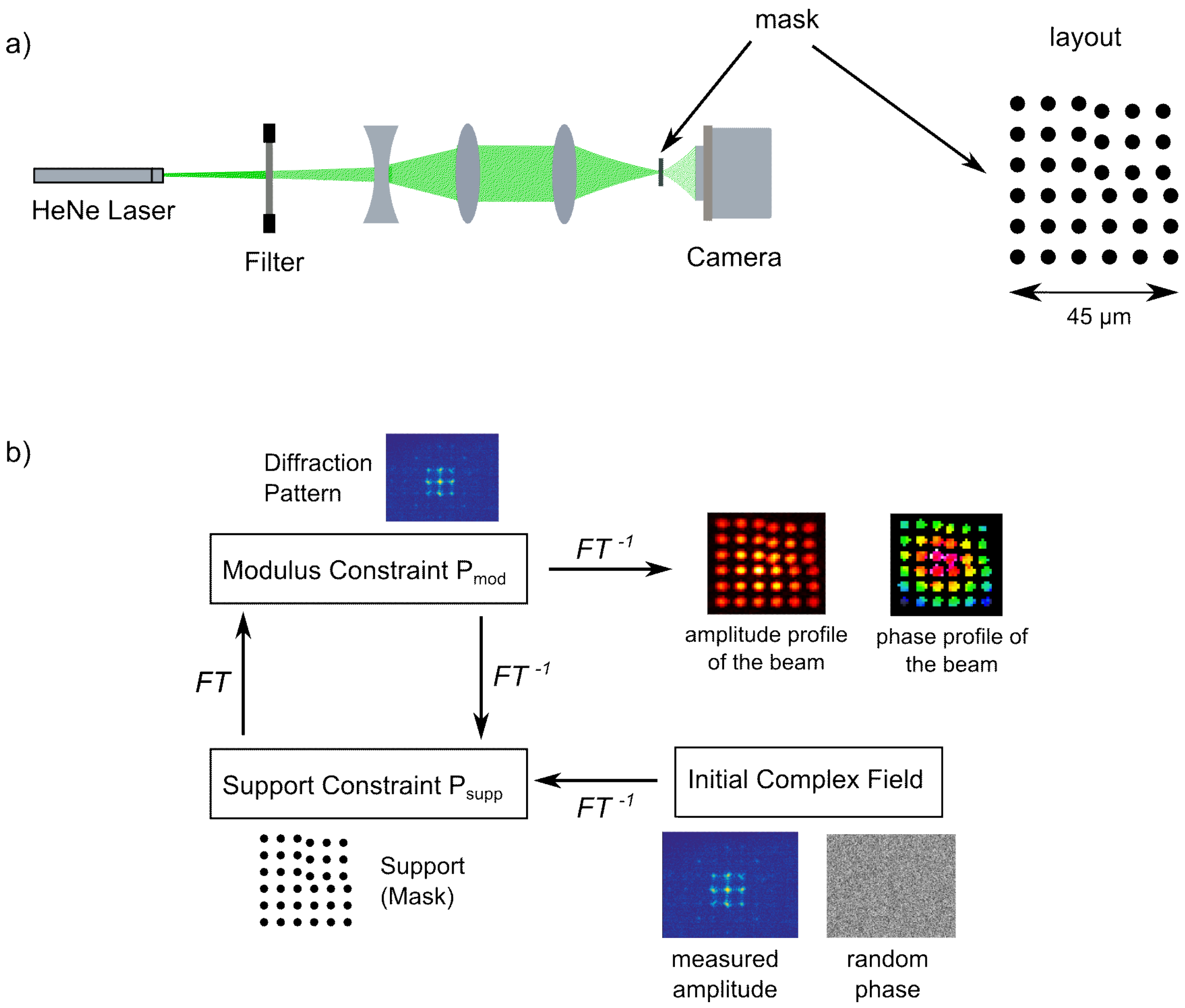

FIGURE 3.17: Principle and setup of a CDI-based wavefront sensor. (a) A schematic diagram of the experimental setup on the left and the layout of the mask on the right. The beam expander consists of a concave lens (focal length 20 mm) and a convex lens (focal length of 25 mm) while the focusing lens has 75 mm focal length. (b) The modified phase retrieval procedure with a fixed support.

reconstructions that are a mixture of the two orientations are effectively avoided. A mask design that satisfies the above three points is shown in Fig. 3.17(a) (right side). The mask has a periodic grid of pinholes but with one quadrant shifted to avoid centrosymmetry. It is also limited in size and the known layout can be used as a support during reconstruction.

3.3.2 Proof-of-principle experiment

The setup of a proof-of-principle experiment for characterizing the focus of a HeNe laser is shown in Fig. 3.17(a). The output of the laser (2 mW CW at 632.8 nm) was attenuated, expanded and subsequently focused on the mask where diffraction patterns were recorded by a CMOS camera placed in the far-field. The CMOS camera (Imaging-Source DMK 33UP5000) has 2595 × 2048 pixels with a pixel size of 4.8 μm and a bit-depth of 8 bits. Due to the fixed cover of the camera, the mask-camera distance was limited to 20 mm which gives an Abbe limit of 1.3 μm. Therefore, the pinholes in the mask layout were chosen to be 5 μm in diameter to have them clearly resolved. To have a meaningful sampling of the beam focus, a total of 6 by 6 pinholes were included and the overall mask size was 45 μm. The Fresnel number for a sample-camera distance of 20 mm then becomes 0.16. Although at the edge of the far-field criterion of Eq. 2.9, the camera can still be considered in the far-field by more relaxed far-field criteria [20]. The mask was fabricated by focused ion beam milling of 50 nm thick Si_3N_4 membrane coated with 200 nm copper. Because the beam intensity around the focus was high, the shortest acquisition times in the range of milliseconds were used in recording the diffraction patterns. The reconstruction procedure (Fig. 3.17(b)) is similar to that of conventional phase retrieval algorithms discussed in section 2.2.2. The only difference is that the support is not updated by the shrink-wrap algorithm in the present case. It is instead taken from the layout of the mask (SEM image) and used for all iterations. A total of 1000 iterations were used that alternated between 150 iterations of the RAAR algorithm and 100 iterations of the error reduction (ER) algorithm. At the output, the amplitude and phase values at each pinhole is retrieved and the values at the regions in between can be interpolated later on.

The mask was scanned at multiple points before and after the beam focus while diffraction patterns were recorded at each of these points. All reconstructed amplitudes (Fig. 3.18(a)) show a higher value at the center that decreases as we go to the edges which is expected from the focus of a Gaussian beam. At z values of ±1.5mm, all pinholes are visible since the beam was large enough to fill the mask. But at z points of zero and ±0.5 mm, only pinholes around the center are visible because the beam is smaller than the mask. Interpolating between the pinholes and taking a cross-section across the center gives a FWHM focal diameter of 16μm. The interpolated phase plots for amplitudes above 20% of the maximum are shown in Fig. 3.18. The phase is assumed to be flat within a pinhole and the average phase value in a pinhole is taken as a single sampling point during interpolation. The phase curvature evolves from a converging to a flat profile and later to a diverging profile after the focus. A more quantitative comparison is plotted for seven points across the focus by taking the cross-section along the center of the interpolated phase profiles (Fig. 3.18(c)). Immediately after the focus which shows a flat phase profile, the curvatures on both sides (at ±0.75 mm) are shown to be the strongest. The radii of curvature at ±1.5 mm and ±2.25 mm are then progressively larger than the values at ±0.75 mm. This is consistent with Gaussian optics where the

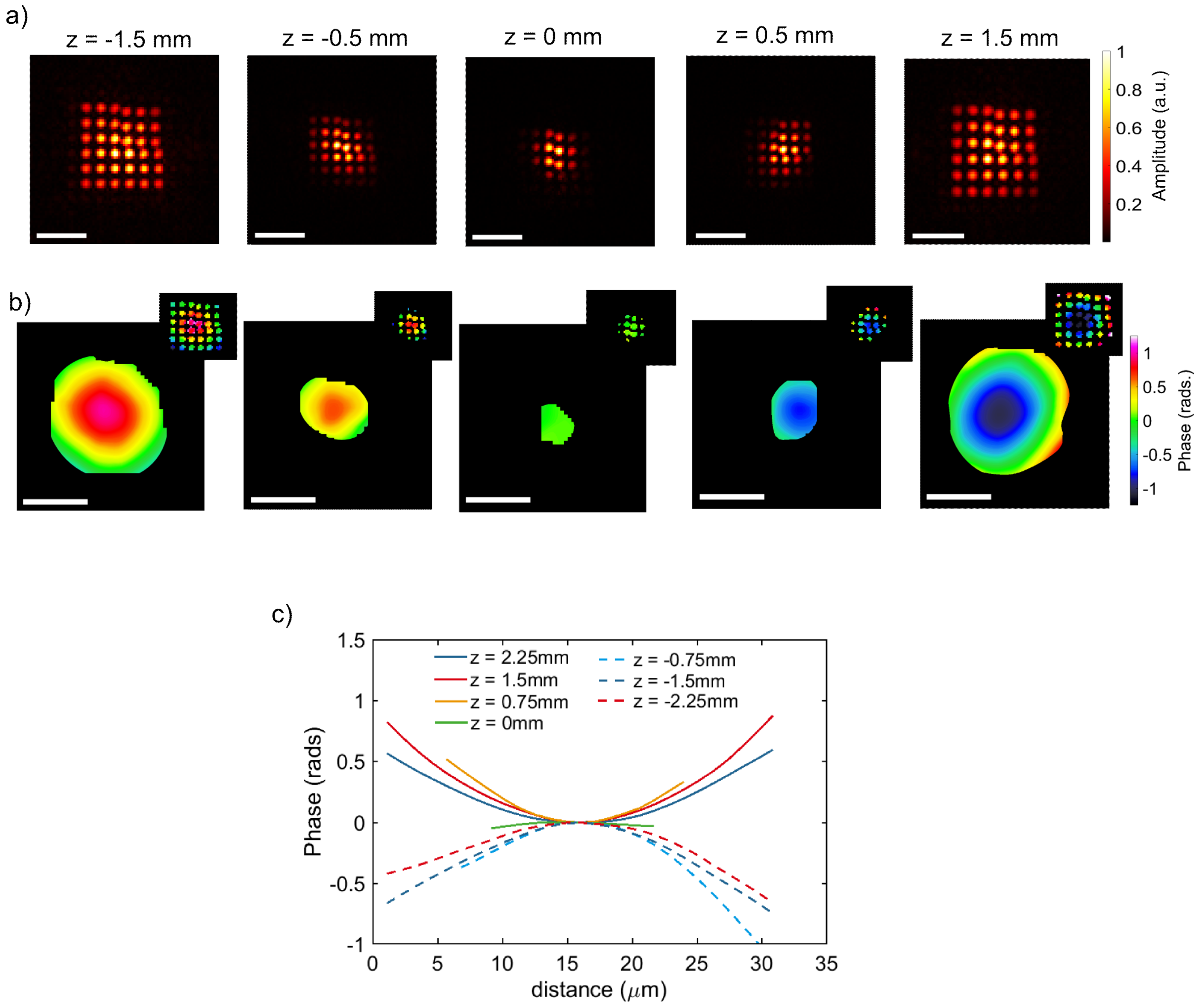

FIGURE 3.18: Amplitude and phase reconstructions of the illuminating beam focus. (a) The reconstructed amplitude at five different planes across the focus. The profiles are shown here before interpolation for better illustration of the procedure. All scale bars are 30 microns. (b) Interpolated phase profiles at the planes corresponding to (a). each inset shows the phase profiles before interpolation for illustration purposes. (c) A cross-section along the center of interpolated phase profiles at seven planes across the focus.

phase curvature is strongest at the Rayleigh length and progressively gets flat towards infinity. Further numerical comparison with Gaussian optics is not included here due to non-precise knowledge of the waist radius.

The above experiment proves that a CDI-based wavefront sensor is indeed feasible. Compared to the commonly used Shack-Hartmann wavefront sensor (SHWS), the CDI-based wavefront sensor (CDI-WS) can give the absolute phase at each sampling point (pinhole) whereas the SHWS measures the local gradient [117]. Therefore, the maximum measurable phase curvature is limited by the period of the mask in a SHWS. In the CDI-WS presented here, there is essentially no limit except for the extremely curved wavefronts where the far-field criterion might not be fulfilled. Even in these special cases, the mask-camera distance can be increased to satisfy the far-field criterion. Commonly, beam characterization is performed at planes where the beam has larger size on a collimated or diverging beam. In the CDI-WS, on the other hand, the measurements are taken at the beam focus where XUV imaging experiments are conducted. This has the advantage that the beam is characterized just before its use in an imaging experiment and the output wavefront includes the influence of all focusing optics. The current CDI-WS experiment had limitations due to lack of large detectors in the visible spectral range for higher resolution and the low bit-depth that limited the dynamic range of the experiment. In the XUV, CCD chips with large sizes are available with a bit-depth of 16 bits. Therefore, finer sampling of the beam focus is possible and a reconstructed wavefront with better quality and sampling is expected in the XUV. The CDI-WS can find applications in characterization and online beam monitoring during imaging experiments in the XUV and soft X-ray spectral range.

In this chapter, a table-top CDI experiment with a half-pitch resolution of 13 nm was demonstrated using a high photon flux HHG source at 18 nm wavelength. The achieved resolution is the highest for a table-top CDI setup and is comparable to zone-plate-based X-ray microscopes operated at large scale facilities [4]. In addition, sub-30 nm resolution was achieved using a single measurement with only 3 seconds of exposure time which shows the feasibility of imaging modalities that require multiple diffraction patterns. These include imaging of extended samples by scanning across them or imaging 3D structures using tomographic approaches. The potential for performance scaling was also shown by performing the first soft X-ray table-top CDI experiment at 8 nm wavelength. In the near future, the high scalability of fiber laser driven HHG sources is expected to deliver the required photon flux at soft X-ray wavelengths for imaging with sub-10 nm resolution. A wavefront sensor based on CDI was also developed which can have applications for live beam monitoring in XUV imaging setups. As discussed in section 2.2.2, convergence speed and reliability are major issues with phase retrieval algorithms in CDI especially for low contrast samples with higher complexity. In the next chapter, high performance imaging using Fourier transform holography is presented which provides more robust and straightforward image reconstruction.

Chapter 4

XUV Fourier Transform Holography

It was shown in the previous chapter that sub-wavelength resolutions can be achieved using conventional CDI employing iterative phase retrieval algorithms. However, there are limitations on the reconstruction speed which, for example, took minutes on a standard PC for our CDI results in section 3.2. The reconstruction time could get longer for noisy diffraction data and samples with higher complexity or low amplitude contrast. Each reconstruction also gives a slightly different output owing to the non-perfect diffraction data and random starting phases. Therefore, multiple generations with parallel reconstructions and a subsequent averaging becomes necessary which further increases the reconstruction time. In addition, the twin image problem discussed in section 2.2.2 could result in stagnation of the phase retrieval algorithms especially for samples with centrosymmetric or loose support.

Fourier transform holography (FTH) is a more robust alternative that overcomes the above limitations of CDI (see section 2.2.3 for a detailed discussion). Previous imaging experiments using FTH at synchrotron facilities achieved resolutions limited by the reference structure size to $\sim$ 50 nm [54, 118]. The highest resolution reported for a table-top XUV/soft X-ray setups is 89 nm with hours of acquisition time [11]. In this chapter, an experiment that demonstrated the highest resolution of 34 nm in FTH for any light source [119] is presented. Refinement of resolution by iterative phase retrieval that enabled resolving of the smallest features in table-top XUV/soft X-ray setups is also discussed. Finally, propagation effects that impact imaging of wavelength-scale features at high aspect ratios are investigated both numerically and experimentally.

4.1 High Resolution FTH

The overall experimental setup is similar to that used for the 70 eV CDI result of section 3.2. In the following experiment, the repetition rate of the laser was increased to 35 kHz and two beam stabilization (BS) systems were used instead of just one. The first BS system was placed in front of the HCF compression stage in order to stabilize the coupling which improved the beam profile and stability of the compressed pulse duration. Another one was placed before the HHG chamber to stabilize the position and incoming angle of the focused IR beam in front of the argon gas jet. To increase the photon flux per unit area for imaging, the focal length of the second multilayer XUV mirror was reduced from 0.5 m to 0.3 m and the FWHM beam diameter at the XUV focus was measured to be $\sim 6\ \mu m$.

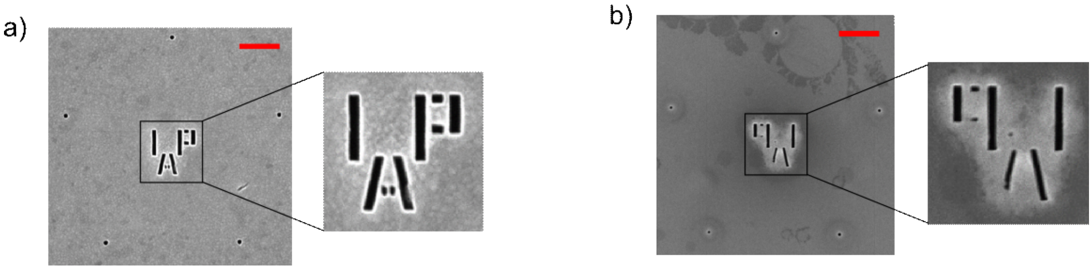

FIGURE 4.1: Helium ion microscope (HIM) image of (a) the front (gold coated) side and (b) the back side of the sample used in the FTH experiment.

4.1.1 Imaging setup

The sample is shown in Fig. 4.1 and is an amplitude-only transmission sample consisting of the letters 'IAP'. Five reference structures (holes) can be seen around the sample equidistant from one another. Both the sample and reference holes were fabricated by electron beam evaporation of 200 nm gold on top of a 50 nm silicon nitride membrane. Patterning of the features was done by a helium ion microscope (HIM) Zeiss Orion plus using structured milling with 30 keV He^+ ions. The same HIM with lower energy was used to image the fabricated sample which are shown in Fig. 4.1. It can be seen in Fig. 4.1(b) that some features of the back side are not fully etched through. HIM was necessary to etch fine features of the sample ($\sim$ 50 nm in size) but, most importantly, to fabricate the smallest reference holes possible. As discussed in section 2.2.3, the achievable resolution in FTH is $\sim$ 70% of the reference structure size. Therefore, the straightforward approach for high resolution FTH is to use small reference structures (but at the cost of image contrast). The smallest reference holes that could be fabricated reliably were 50 nm in diameter. Previous attempts to fabricate 30 nm diameter holes didn't succeed since the holes couldn't be etched through the entire membrane in a repeatable manner. The five reference holes were positioned far enough (1.5 μm) from the sample to avoid overlap of the autocorrelation and cross-correlation terms during reconstruction.

The distance between the sample and the camera was 20 mm which enabled diffraction measurement at an NA of 0.57. The interference between waves diffracted from the sample and those from the reference holes forms a hologram in the far field as shown in Fig. 4.2(a). The acquisition time was 20 sec. and it was long enough to record a diffraction pattern with corresponding resolution below the limit imposed by the reference hole size. Thus, longer acquisition times will not result in a better resolution value. The inset of Fig. 4.2(a) shows the honey-comb type ripple patterns resulting from the modulation of a particular diffraction fringe with waves from the five reference holes. The diffraction pattern is above the noise level up to $\sim$ 20 μm^{-1} corresponding to an NA-limited resolution of 25 nm while the reference-limited resolution is 35 nm (70% of the reference hole diameter).

4.1.2 FTH reconstruction results

Holographic reconstruction was performed by inverse Fourier transforming the measured hologram and the result is shown in Fig. 4.2(b). It shows five independent cross-correlations of the sample with the reference holes and their five complex conjugates. The autocorrelation of the sample and those of the references are located at the center of the field in Fig. 4.2(b). Since these autocorrelations are much brighter than the cross-correlations, they are masked out in Fig. 4.2(b) for a better illustration. Although much dimmer, the cross-correlation of the reference holes among themselves can be seen at the farthest edges of Fig. 4.2(b). Among the five independent reconstructions, the standard deviation averaged over each pixel is $< 15\%$ for the amplitude profile and $< \pi/20$ for the phase. This demonstrates the robustness of image formation in FTH. An average over these five independent reconstructions is shown in Fig. 4.2(c) and clearly displays all features of the sample. Only one of the two central dots of the letter 'A' in the front-side image of Fig. 4.1(a) is visible in the averaged reconstruction. Since this dot is not visible in the back-side HIM image of Fig. 4.1(b), this feature is imaged through the gold/silicon

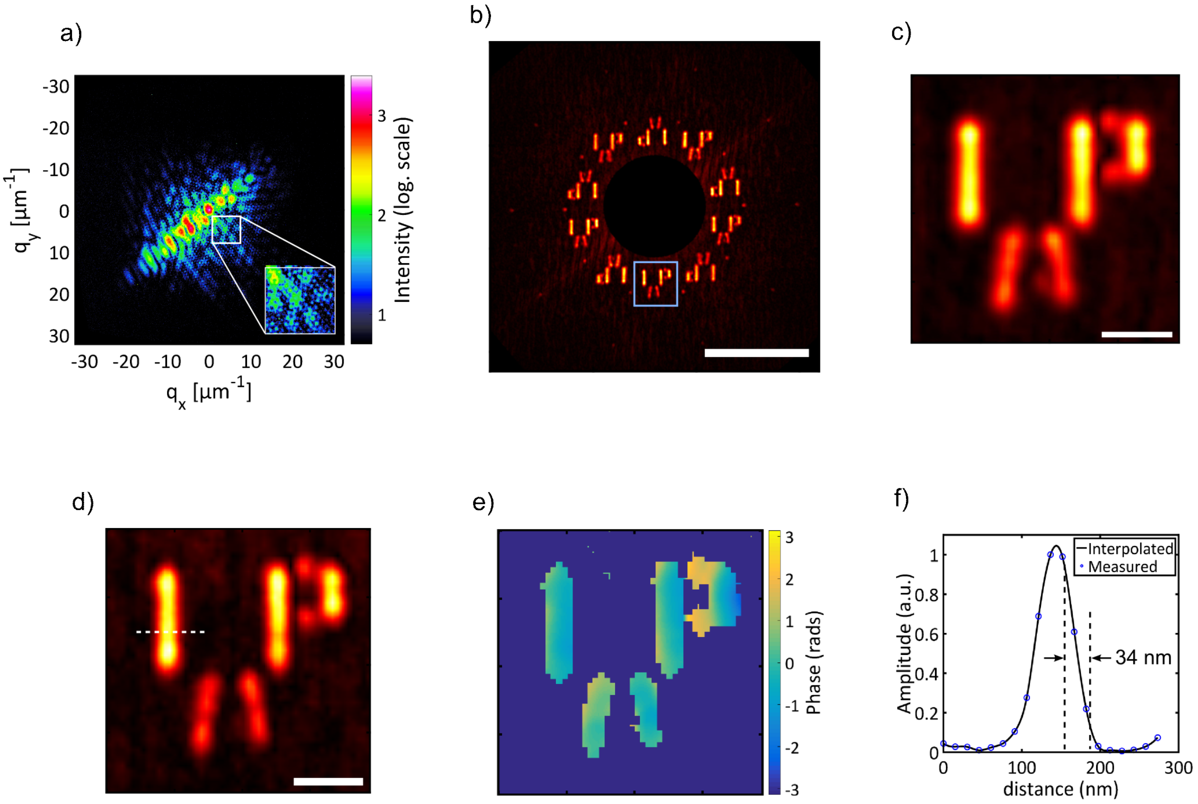

Figure 4.2: Results of the FTH experiment. (a) The recorded diffraction pattern (hologram) with acquisition time of 20 seconds. (b) The inverse Fourier transform of (a) showing multiple copies of the sample. (c) An average of the five independent reconstructions in (b). The reconstruction with the best resolution shown in (d) amplitude and (e) phase taken from the blue square in (b). (f) A cross-section along the dotted line in (d).

nitride membrane. Note that the five reference holes could have slightly different sizes upon fabrication which could result in differing resolution for the five reconstructions in Fig. 4.2(b). The amplitude profile of one of these reconstructions (inside the blue square of Fig. 4.2(b)) that showed sharper features that the averaged profile is displayed in Fig. 4.2(d). The SNR of this reconstruction is however worse than the averaged profile demonstrating the advantage of averaging. A knife-edge test along the dotted white line of Fig. 4.2(d) showed the reference-limited resolution of 34 nm (Fig. 4.2(f)). The achieved resolution is the highest obtained for an FTH setup using any light source including synchrotrons and X-ray free electron lasers. The phase profile (Fig. 4.2(e)) is non-flat with values ranging between $\pm 0.75\pi$. This non-flat phase profile could be a consequence of propagation effects through the thick sample and non-perfect fabrication of the sample's features. A phase jump is noticeable between the longer bars and the two dots of the letter 'P' further strengthening the conclusion that propagation effects play a role in defining the exit wave profile. These issues will be discussed in detail in section 4.3.

4.2 Refinement using Phase Retrieval

The resolution of the FTH measurement above is limited by the reference hole size and not the effective NA of the measurement. This can be improved if the experiment is set up so that the overall diffracting area satisfies the oversampling criterion discussed in section 2.2.1. The diffracting are in FTH includes both the sample and all reference structures. If the oversampling criterion is fulfilled, iterative phase retrieval can be used to retrieve images with resolution limited by the highest diffraction angles measured. In this case, two measurements with acquisition times of 1 minute and 5 minutes were merged together using the procedure described in section 3.2 to have an increased dynamic range. The merged diffraction pattern is shown in Fig. 4.3(a) and shows fringes above the noise level until the edge of the detector. This corresponds to an Abbe limit of 15 nm.

4.2.1 Data processing and reconstruction

The gold coating applied to make the opaque part of the sample was not thick enough to absorb all the incoming XUV light. Half as many counts as the central peak count of the hologram were recorded when the opaque part is illuminated. To overcome this issue, the width and peak count of this directly transmitted beam were estimated and a Gaussian function with these parameters was subtracted from the measured hologram. Hot pixels were then removed and curvature correction was performed on the processed hologram. A numerical binning of 4 by 4 was used during the measurement resulting in an oversampling degree of 3.2 for a sample-detector distance of 20mm. This is above the minimum oversampling degree of $\sqrt{2}$ required for successful phase retrieval. The guided RAAR algorithm already used in the CDI reconstructions of the last chapter was used in performing phase retrieval. A β parameter of 0.95, 12 independent reconstructions and 5 generations were used. Phase retrieval was successful but a parametric run of reconstruction variables like thresholds and update intervals was necessary to get a high quality image. In addition, few thousands of iterations are required which takes few

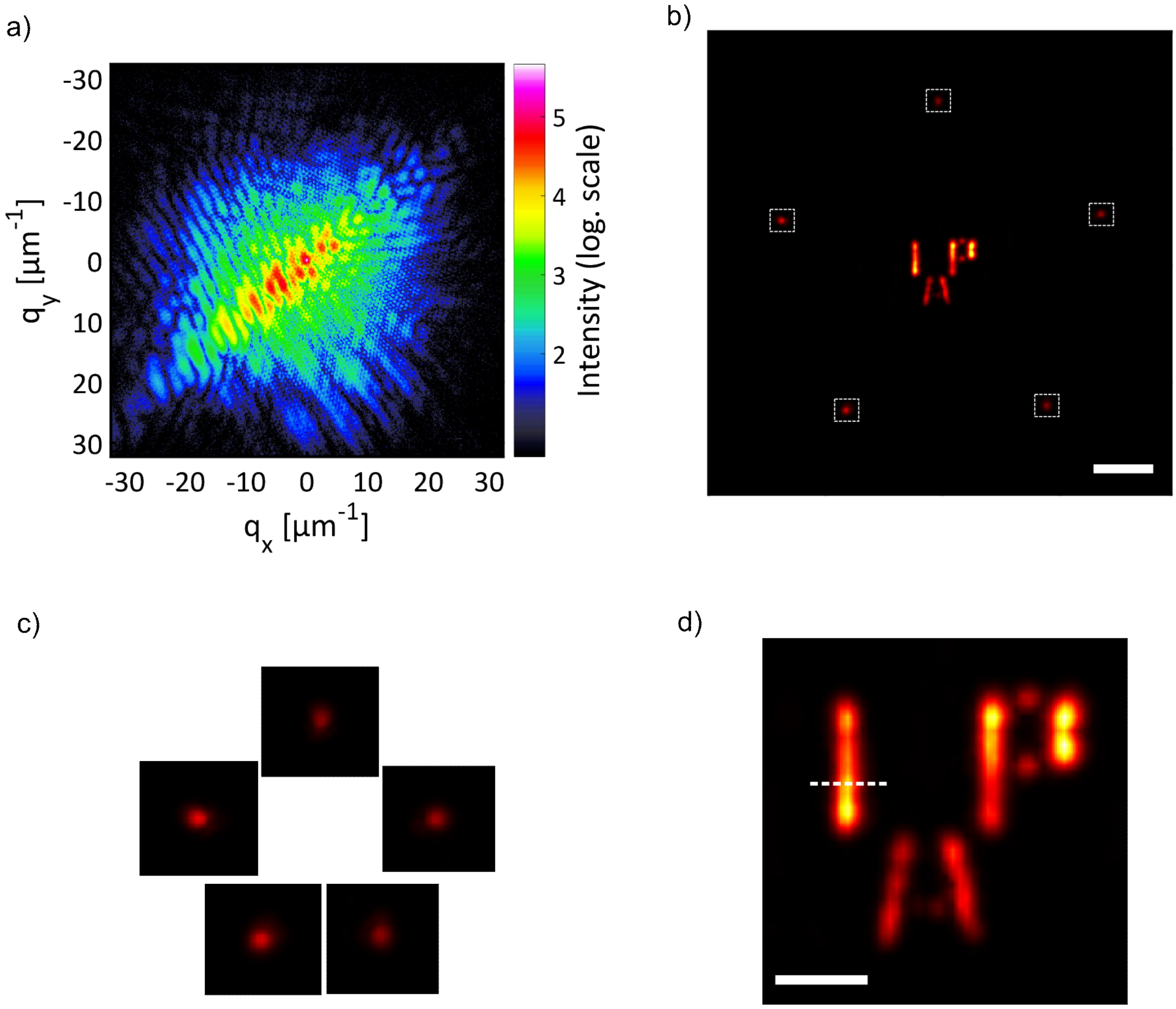

FIGURE 4.3: Iterative phase retrieval on an FTH reconstruction. (a) A composite diffraction pattern (hologram) recorded with acquisition times of 1 minute and 5 minutes. (b) A CDI reconstruction of the hologram in (a) using an FTH reconstruction as an initial guess (scale bar is 500 nm). (c) A close-up look into the five reconstructed holes shown in dotted squares in (b) arranged accordingly. (d) A close-up look of the sample area in (b) showing modulated exit wave profile (scale bar is 200 nm).

minutes on the standard PC (Intel Core i5 6500, 4 cores) that was used. On the other hand, an image of the sample is already available from FTH. This image (Fig. 4.2 (c)) was taken as a first guess instead of using the object autocorrelation as is normally done in phase retrieval. The shrink-wrap algorithm was then used to update the support once the updating interval is reached. Seeding the reconstruction with the FTH image increases the reliability since the rough sample features are already present in the object estimate. It also significantly reduces reconstruction time to few seconds because the algorithm only incorporates the high angle diffraction information to refine the image resolution. The exit wave from the reference holes is dimmer than of the sample area due to propagation effects to be discussed in the next section. Therefore, differing threshold were used in performing the shrink-wrap procedure for the seeded area (that includes the sample) and the region outside (that includes the reference holes).

The result of the iterative phase retrieval refinement is displayed in Fig. 4.3(b) and shows the sample area together with the five reference holes. It can be seen that the reference holes are dimmer than the sample's features and the reason will be discussed in the next section. The reference holes (insets displayed in Fig. 4.3(c)) have differing FWHM diameters ranging between 48 nm and 56 nm which agrees well with the nominal value of 50 nm. The standard deviation among the diameters estimated from the 12 independent reconstructions of each reference holes is ±1nm . This gives an indication of the precision with which the hole sizes are being estimated. The FTH image shown in Fig. 4.2(d) corresponds to the reference hole with the smallest diameter of 48 nm which explains why it gave the best resolution. A close-up look at the sample area (Fig. 4.3(d)) shows the features are sharper than those in Fig. 4.2(c) and (d) with modulated intensities at the longer bars. A knife-edge resolution test across the white dotted line revealed a half-pitch resolution of 24 nm, an improvement compared to the 34 nm found with FTH only. It will be shown in the next section that the resolution is limited by propagation effects and not by the Abbe limit.

4.2.2 Imaging through a membrane

The reconstruction of letter 'A' and comparison with front and back side HIM images is shown in Fig. 4.4 (a-c). It can be seen that the two central dots are not visible in the back side HIM image because they are not etched all the way through. However, these dots are visible in the holographic CDI image of Fig. 4.4(c). This illustrates the penetrative capability of imaging with XUV light in comparison with electron/ion microscopy. In addition, the dot on the right side has higher transmission than the one on the left although the front side HIM image shows comparable sizes. This indicates that the right dot is etched deeper in the gold/silicon-nitride membrane. A cross-section taken along the two dots is displayed in Fig. 4.4(d) and shows that the half-distance between the two dots is 23 nm. The half-distance between the dots and the neighboring legs of the letter 'A' is also 23 nm. The resolving power of the imaging setup is better than these reported values since the dots are clearly separated. In addition to being imaged through a membrane, these are the smallest features resolved in a table-top XUV/soft X-ray setup to date. The thickness of the remaining gold/Si$_3N_4$ membrane at the two central dots can be estimated from the relative transmitted intensities and the transmission of gold and Si$_3N_4$ at 18.1 nm. Neglecting other propagation effects, it is estimated that both dots have the entire 50 nm of Si$_3N_4$ membrane unetched. Additionally, the dot on the left side has an estimated 25 nm of gold layer while the one on the right has 8 nm of gold layer left unetched.

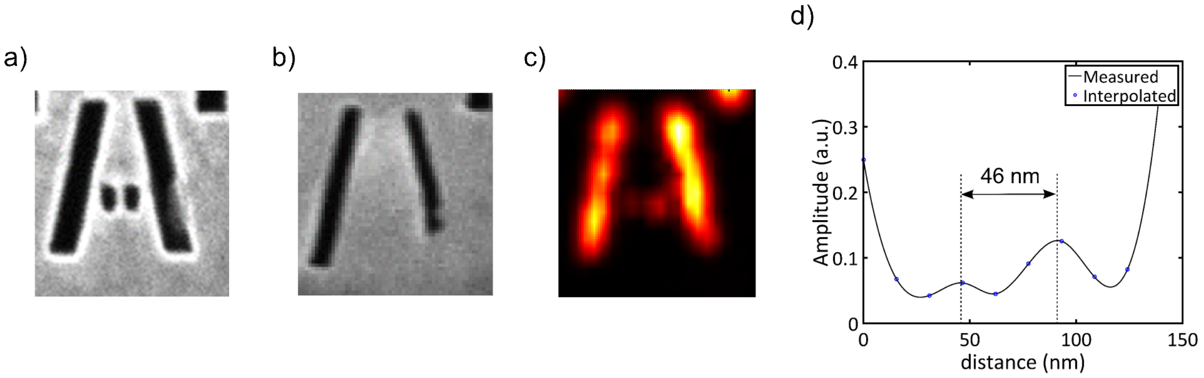

FIGURE 4.4: Imaging though a membrane. Helium ion microscope (HIM) image of the (a) front (gold coated) side and (b) back side of the letter 'A' of the sample. (c) A close-up look of the reconstruction of the letter 'A' from Fig. 4.3(d). (d) A horizontal cross-section along the two central dots of (c).

4.3 Waveguiding Effects

It was mentioned in the previous section that the ESW profile of the sample doesn't exactly follow its geometrical shape from the HIM image. Amplitude variation can be observed along the long bars of 'I' and 'P' of Fig. 4.3(d) that follows width variation of the back side HIM images of the same bars. Larger width in the HIM image (at the lower part of letter 'I' and upper part of letter 'P') corresponds to higher ESW amplitude in the holographic CDI image. In addition, modulation of amplitude in the longer bars with peaks at the edges and decrease in ESW amplitude of the small features (horizontal bars of 'P' for example) are observable in Fig. 4.3(d). From the projection approximation, the feature size doesn't influence ESW amplitude and modulations in amplitude are not expected for a binary sample. These observations suggest the existence of other physical effects that arise in such sub-wavelength imaging systems. To further investigate this, a finite difference time domain (FDTD) simulation was performed in collaboration with our colleague M. Zilk from the Nano Optics group of the Insitute of Applied Physics, Jena.

The sample was modeled as a 3D layered structure considering the thicknesses and refractive indices of gold and Si_3N_4 at 18.1 nm. The commercial simulator Lumerical FDTD solutions 2016b was used. Thicknesses of 200 nm for the gold layer and 50 nm for the Si_3N_4 layer were included similar to the fabricated sample. An area of 1.5 μm by 1.5 μm that includes the 'IAP' feature was simulated where the transversal profile of the 'IAP' feature was taken from the front side HIM image. The simulated area was discretized in a uniform grid with resolution of 0.714 nm ($\lambda/25$) and perfectly matched layers (PMLs) were used as a boundary condition to absorb the scattered fields. The structure was excited by a plane wave centered at 18.1 nm from the Si_3N_4 side as was the case during the experiment. Choice of a plane wave as illumination is justified since the XUV beam ($\sim$ 6 μm) in the experiment was much bigger in size than the simulated structure ($\sim$ 0.6 μm). The intensity distribution and phase front of the XUV beam at the sample can, therefore, be assumed to be flat. The exciting field was normally incident on the structure and was linearly polarized with a tilt of 45° with respect to the x-direction similar to the experiment. The refractive indices of gold and Si_3N_4 were taken from the X-ray database of the center for X-ray optics (CXRO)[120].

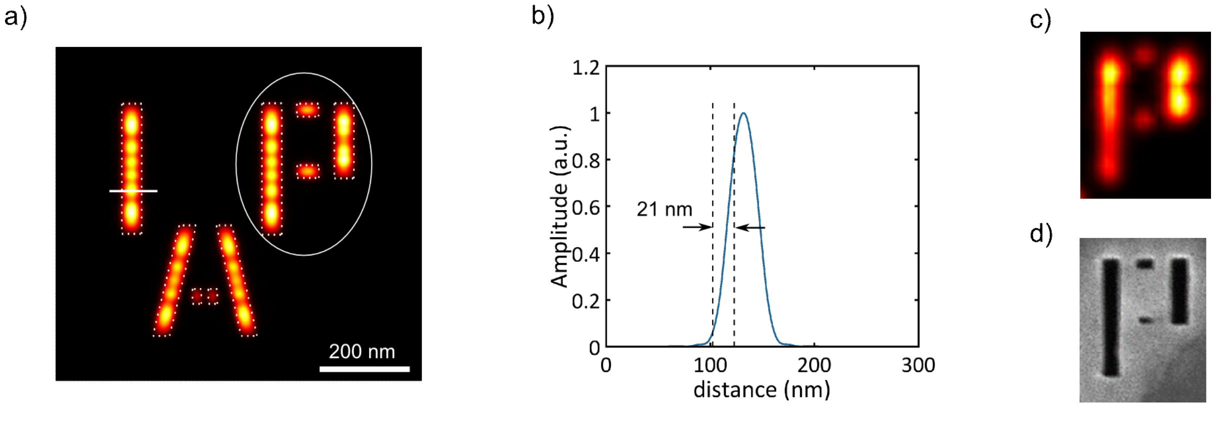

FIGURE 4.5: (a) Exit wave of the 'IAP' structure computed using the FDTD method. (b) Cross-section along the white line on the letter 'I' in (a). (c) Close-up looks at the reconstruction of the letter 'P' in Fig. 4.3(d). (d) Close-up look at the HIM image of the letter 'P' in Fig. 4.1(b).

The result of the FDTD computation (Fig. 4.5(a)) shows that the simulated ESW amplitude also doesn't follow the geometrical profile (shown by the white dotted line). The modulations observed in the simulation as well as the experiment demonstrate that the ESW is no longer a product of the sample profile and the illuminating beam profile. The samples features are $\sim$ 50 nm (2.5λ) in size while the thickness of its absorbing gold layer is 200 nm. This gives an aspect ratio of $1 : 4$ which is high enough to cause the features to act as a waveguide to the illuminating XUV beam. The ESW in this case is a superposition of waveguide modes of the particular feature in consideration. These waveguide modes have size-dependent propagation losses which explains the lower transmission of smaller features that was observed both in the simulation and experimental results. The FDTD result also shows the modulations in ESW amplitude at the longer bars with peaks at the edges that was observed in the experimental result of Fig. 4.3(d). A cross section along the white line of the letter 'I' (Fig. 4.5(b)) shows a 10/90 distance of 21 nm although the discretization step used for the FDTD computation was 0.714 nm. Under the projection approximation, the 10/90 distance should have been comparable to the discretization step for such a binary sample. This shows that the achievable resolution in imaging wavelength-scale features with high aspect ratio is mainly limited by waveguiding instead of the Abbe limit. Comparison of the letter 'P' in Fig. 4.5(a) and the experimental result in Fig. 4.5(c) shows a similar ESW profile especially at the shorter vertical bar. A look at the longer bar of letter 'P' in the Fig. 4.5(c) and the HIM image in Fig. 4.5(d) shows amplitude of holographic CDI image decreases as the bar width in the HIM image gets narrower as is expected in the presence of waveguiding.

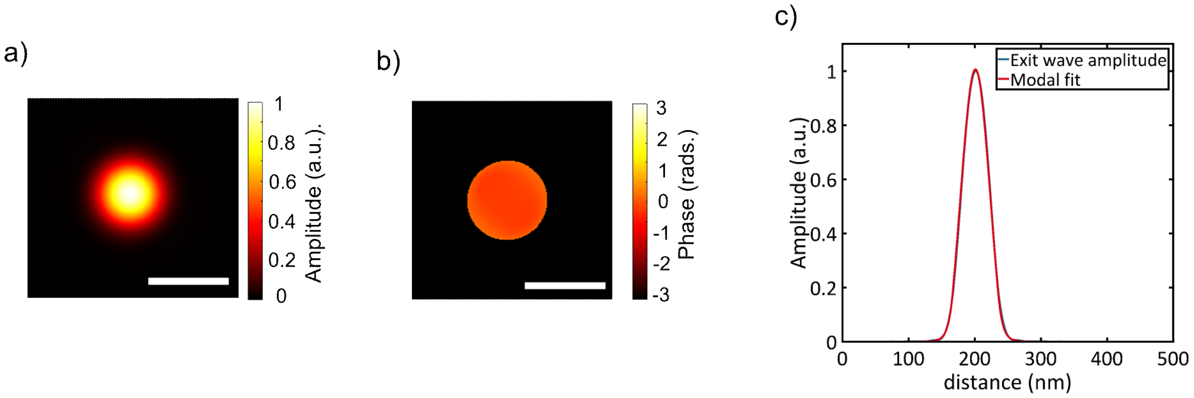

FIGURE 4.6: Exit wave of 50 nm diameter reference holes computed using the FDTD method shown in (a) amplitude and (b) phase. (c) Horizontal cross-section along the center of (a) and comparison with a fit from modal analysis.

Waveguiding also affects the field exiting the reference holes since their aspect ratio is also high (1 : 4 like the samples's features). This could influence resolution and/or contrast of the FTH image although the refinement using phase retrieval overcomes the issue. FDTD simulation of the same multilayer structure (200 nm gold and 50 nm Si_3N_4) for a 50 nm wide pinhole is depicted in Fig. 4.6(a) and (b). Amplitude of the ESW (Fig. 4.6(a)) shows a deviation from the circular, flat-top feature expected under a simple projection approximation. It is now rather a Gaussian-like profile with blurred edges. The phase profile is displayed for amplitude values above 10% of the maximum (Fig. 4.6(b)). It is relatively flat with slight curvature along the polarization direction. To demonstrate that the ESW is indeed a superposition of multiple waveguide modes, a modal analysis of the simulated pinhole structure was performed. The modal analysis was implemented using a commercial mode solver, Lumerical Modal solutions 2017b, with discretization the same as the FDTD simulation. In a 50 nm diameter hole, only three waveguide modes were excited at normal incidence for linearly polarized illumination at 18.1 nm (see supplementary material of [119]). Fitting these modes to the result of the FDTD simulation gave residual error below 8%. The comparison between cross sections along the center of the fields of the the modal fit and the FDTD result is shown Fig. 4.6(c) and shows an almost perfect fit. The transmission of the reference holes was computed from FDTD to be 75% for the 50 nm pinholes used and it goes down to 1% for 20 nm pinholes. This explains the observation in Fig. 4.3(c) where smaller reference holes also showed lower transmission. The ESW of the reference holes in the FDTD simulation extend beyond the 50 nm diameter set by the actual feature size and this seems to modify the resolution limit in FTH due to reference hole size. However, a cross-correlation of the ESW from FDTD with a sharp edge showed that the resolution limit of 70% of reference hole size is not changed. This is because the larger extension of the Gaussian-like exit wave beyond the geometrical size is compensated by the fact that it is pointed (peaking towards the center).

A Fourier transform holography (FTH) experiment achieving a half-pitch resolution of 34 nm, which is the highest resolution in FTH from any light source, was presented in this chapter. Issues with reliability and convergence speed that were observed in conventional CDI were avoided in FTH by directly encoding the phase of the diffracted field. In addition, the high photon flux of the HHG source enabled the reduction of exposure times to record a hologram from hours to tens of seconds compared to previous table-top results [11]. Iterative phase retrieval algorithms were still relevant to overcome the resolution limit of FTH imposed by the size of the reference structure. Features separated by a half-distance of 23 nm were resolved by employing phase retrieval algorithms on the recorded hologram and using the FTH reconstruction as a seed. These are the smallest features ever resolved by a table-top CDI setup in addition to being imaged through a membrane. Waveguiding through the wavelength-sized features of the sample were also found to influence image quality and impose a limit on the achievable resolution. Combined implementation of FTH and iterative phase retrieval can enable the realization of a high resolution and robust lensless imaging scheme for a broad range of sample types.

Chapter 5

Wavelength-scale Ptychographic CDI

The basic implementation of coherent diffractive imaging (CDI) covered in chapter 3 forces the sample to be isolated and uses this a priori information to solve the phase retrieval problem. In Fourier transform holography (FTH) discussed in chapter 4, the sample also needs to be isolated and placed at a proper distance from the reference structures. Both of these techniques have the main disadvantage of having to isolate the sample in a region that is few microns in size for typical setups in the XUV spectral range. This is not convenient for real world applications like imaging of biological specimen or semiconductor mask inspection where the samples are extended over areas that are hundreds of microns in size. An approach to image extended samples is to record multiple diffraction patterns by scanning a sample relative to the illuminating beam as was introduced in section 2.2.4. Ptychography extends the field of view for imaging to hundreds of microns while maintaining the nanoscale resolutions achievable in conventional CDI [57, 121]. Since the illuminating probe is reconstructed together with the sample, it is also applicable as a beam characterization method. Ptychography can also be integrated with other imaging modalities like 3D tomography to image integrated circuits [9] and whole unstained cells [10] in 3D with nanoscale resolutions.

Ptychography experiments were mainly performed at synchrotron facilities with limited availability that hindered a wider scientific/commercial application. With the recent progress in table-top XUV/soft X-ray sources, ptychographic imaging experiments with 10/90 resolutions of 40 nm [122] and 58 nm [123] were reported for non-periodic samples.

Sub-20 nm resolutions were claimed for periodic samples [13] although there are still some discussions on the reliability of reconstructions for such samples. This issue originates from the lack of diversity between consecutive scan positions on a periodic sample and will be dealt in an upcoming publication. In this chapter, the ptychographic setup together with the additional requirements in comparison to conventional CDI setups are discussed. Spatial characterization of the illuminating XUV beam using ptychography is also demonstrated. Resolving the smallest features in any table-top ptychographic imaging setup [124] with sizes of just 2.5λ is presented in section 5.4. Finally, the unique challenge waveguiding effects bring to ptychographic imaging of wavelength-scale features is discussed with some suggestions to account for it in the reconstruction process.

5.1 Experimental Setup

The HHG source used in the ptychography experiment was the same as that used in the holography experiment of the previous chapter. The setup of the HHG and imaging chambers, focusing arrangement, location of the sample, beam stop and camera is similar to what was presented in section 3.2. The $1/e^2$ intensity of the focused XUV beam at the circle of least confusion was estimated to be 10 μm. In ptychography, the size of the diffracting region is set by the illuminating beam size at the sample and not by the sample size itself (as was the case in CDI and FTH). Therefore, having a beam size at the sample that is small enough to satisfy the far-field criterion is mandatory for a successful reconstruction. In addition, it is reported that a defined (constrained) illumination with no intensity outside a given area results in a better convergence than a slowly decaying illumination [125]. To fulfill these two conditions, beam constraining pinholes with sizes between 3 μm and 7 μm were placed $\sim 400\mu m$ upstream of the sample. The pinholes were fabricated by depositing 200 nm gold layer on a 50 nm thick Si_3N_4 membrane and subsequently etching using focused ion beam (FIB) milling. The sample and the beam constraining pinhole were mounted on two independent sensor-enabled XYZ positioners (Smaract SLC-1740s). The positioners were capable of closed-loop position control and have a resolution of few nanometers. The sample was transversally scanned across the XUV beam and diffraction patterns were recorded at each scan point (see Fig. 2.7).

The increased capability of ptychography also brings new requirements on the source, positioning system and computational resources necessary for reconstruction. Limits on the coherence of XUV sources, shifts in scan positions caused by beam pointing fluctuation or long term positioner drifts can cause degradation of performance that needs to be quantified properly. Stray light from the sensors of the XY positioners caused a non-uniform background that reduced the SNR of the measured diffraction patterns. Shielding the positioners reduced the stray light but it was not enough to remove the non-uniform background. Disabling the sensors during measurement caused a drift of both the sample and pinhole positioners by $\sim 5\ \mu m$ along the vertical and $\sim 3\ \mu m$ along the horizontal in a time period of 5 minutes. This drift is not acceptable since a high resolution measurement could take tens of minutes to record. Another option provided by the positioner software is a power-save mode where the sensors are enabled in defined intervals and turned off most of the time. This operation mode was a good compromise between stray light and positioner drift. Thermal drift is another source of sample/pinhole positioning error and a drift of $\sim 2\ \mu m$ was measured mainly along the vertical direction over a time period of one hour. This error was reduced by insuring the system reaches thermal equilibrium before starting a measurement. As described in section 3.1.1, two beam stabilization systems (BSS) were incorporated in the setup. The second one was placed just before the HHG chamber and stabilized the focus of the driving laser to $< 4\ \mu m$ of position and $< 2\ \mu rads$ of angular fluctuations. From a ray-optical analysis, these values correspond to < 100 nm of position and $< 1\ \mu rads$ of angular fluctuations of the XUV beam focus.

5.2 Beam Characterization

The first step in choosing the right parameters for the ptychographic experiment is characterizing the beam profile at the XUV focus. The size of the beam-constraining pinhole, the distance between consecutive scan points (the scan step) and the binning of the detector are among the parameters influenced by the beam size. Although a rough beam size estimate of 10 μm was found by scanning a 1 μm pinhole vertically and horizontally, a proper characterization was not done so far. Here we use ptychography to characterize the XUV focus in both amplitude and phase. It has been mentioned in section 2.2.4 that ptychography retrieves the complex amplitudes of both the object and the illumination function (probe). The ptychographic algorithms do not differentiate whether a constrained beam is scanned across an object or a constrained (isolated) object is scanned across the beam. In both cases, the algorithms work as long as the exit waves have a defined extent. In doing beam characterization, an isolated object (for example, a pinhole) is used as the probe and the extended beam is taken as the unknown object (Fig. 5.1(a)). A 3 μm pinhole is used as the probe and it was scanned across the XUV focus with a scan step of 1 μm. Diffraction patterns at a total of 154 scan points were taken with an acquisition time of 0.1 second/scan point. Since rectangular scan patterns were shown to result in reconstruction artifacts [59, 60], a spiral pattern covering an area $\sim$ 12 μm by 12 μm was used (Fig. 5.1(b)).

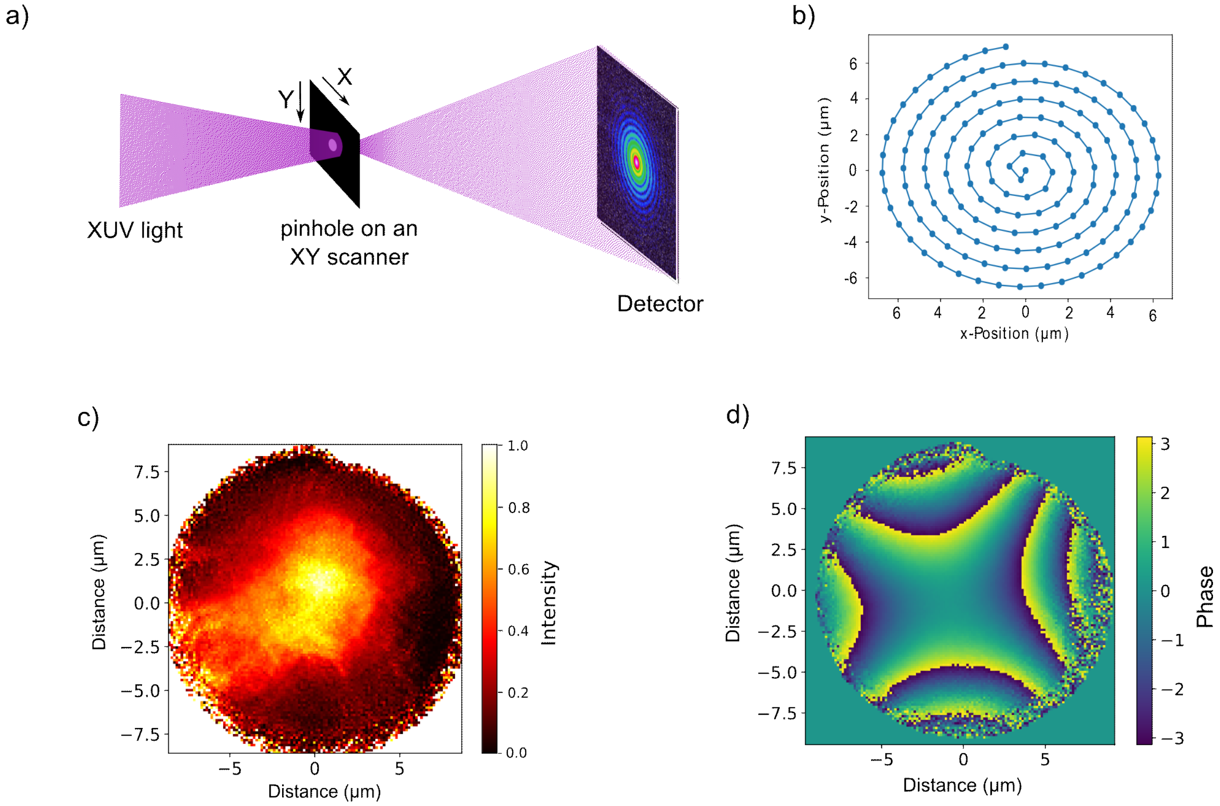

FIGURE 5.1: XUV beam characterization using ptychography. (a) The experimental setup involving a movable pinhole and a detector. (b) The spiral scan path used in the ptychographic measurement. The reconstructed (c) intensity and (d) phase profile of the XUV beam.

For the reconstruction, 500 iterations of the ePIE algorithm were used followed by 100 iterations of the maximum likelihood (ML) algorithm. A flat-top circular profile with a 3 μm diameter was taken as an initial guess for the probe since we know the size of the pinhole from SEM measurements. After 20 iterations, the probe function was updated to relax the constraint and accommodate for some experimental inaccuracies (exact shape of the pinhole, positioning errors among others). The reconstructed XUV beam profile at the focus is shown in Fig. 5.1(c) for the intensity and Fig. 5.1(d) for the phase. Although the probe function was freely evolving during the reconstruction, a circular function with the expected size of 3 μm was reconstructed as the probe. It can thus be concluded that the reconstruction was successful and drifts were only minor during this scan. The intensity profile (Fig. 5.1(c)) shows a round beam that is extended mainly towards the horizontal direction. This is to be expected from the astigmatism of the setup (Fig. 3.7) and it can be concluded that the measured profile lies slightly after the circle of least confusion where the horizontal beam diameter is larger than the vertical. A cross-section taken through the center of the intensity profile gave a FWHM diameters of 10 μm along the horizontal and 7.5 μm along the vertical direction. The edges of the reconstructed intensity and phase profiles are noisy due to the lower illumination overlap in these regions (as it is the last round of the spiral scan). The reconstructed phase (Fig. 5.1(d)) shows a clear saddle-shaped profile characteristic of astigmatism. The fact that the overall beam size is $> 10\mu$m is the reason for incorporating a beam-constraining pinhole before the actual sample. Besides fulfilling the far-field criterion, using a smaller section of the XUV beam relaxes the constraint on spatial coherence and gives a better resolution for a given spectral bandwidth (Eq. 2.32). Lower flux available for imaging (resulting in longer exposure times) and smaller scan step (resulting in smaller field of view) are the disadvantages of using a pinhole. In addition, it adds complexity to the setup and puts a strict limit on the stability of the positioners to avoid a shifting illumination.

5.3 High Performance Ptychography

Previous results in table-top ptychography reported resolution values on the order of the illuminating wavelength although the feature sizes imaged were much larger ($> 10\lambda$). However, the goal of any high resolution imaging system is to resolve small features that are too close to be separable by a lower resolution imaging system. For example, the feature sizes in potential applications of high resolution ptychography (mask inspection, integrated circuits or biological samples) are just few tens of nanometers. Therefore, the ability to resolve these closely-spaced small features is a requirement in contrast to imaging an isolated sharp edge. In comparison with synchrotron sources delivering similar flux, resolving small features is more challenging for table-top sources. This is mainly due to the longer wavelengths used ($>$ 10 nm) which are on the order of the feature sizes to be resolved. In this case, propagation effects like waveguiding become more pronounced and need to be taken into account in image reconstruction (see section 4.3). In addition, previous works on table-top setups relied on the knife-edge test (10%-90% criterion) to estimate the achieved resolution. While this criterion is well justified when used together with a Fourier space analysis [126] of the highest spatial frequency consistently retrieved, it can lead to erroneous resolution estimates in the absence of one. These inaccurate estimates can arise from numerical artifacts in the reconstruction that show artificially sharp edges not found in the actual sample. To clarify these issues, application of the Rayleigh-type criteria on a standard Siemens star type sample has been suggested for coherent imaging [127]. A Siemens star sample provides progressively smaller features in every in-plane direction making comprehensive resolution analysis possible.

5.3.1 Measurement with high resolution

For this experiment, an ultra-high resolution chart (NTT-AT:ATN/XRESO-20) that is commercially available was used as a transmission sample. It contains a Siemens star pattern with a smallest feature size of 20 nm (Fig. 5.2(a)). The absorber is a 100 nm thick Ta while the membrane has three layers : 20 nm Ru, 200 nm SiC and 50 nm Si_3N_4. Unfortunately, the sample is designed for hard X-rays and its overall transmission was just 1.7 % at 68.6 eV. The distance between the sample and the XUV camera was 27 mm resulting in an Abbe limit of 20 nm. The first ptychographic measurement was aimed at achieving the highest resolution possible with the setup. Two measurements with acquisition times of 1 sec. and 10 sec. were taken at each scan point to capture the low and high spatial frequency information respectively. In the 10 sec. datasets, a beam stop with a diameter of 200 μm was used to block the central bright diffraction fringe and avoid blooming of the camera pixels. The dynamic range of the measurement was increased by merging the two diffraction patterns similar to the CDI and FTH experiments in the previous chapters. One such high dynamic range diffraction pattern is shown in Fig. 5.2(b). A spiral scan pattern was followed to record diffraction patterns at a total of 51 scan points with a scan step of 1.5 μm. The ptychographic reconstruction was performed using Ptypy, a framework implemented in python for use across diverse types of setups [64]. The Ptypy framework has all basic ptychographic algorithms implemented and users can additionally include their own features or modifications. One such addition is a position correction algorithm to compensate for small position drifts between the original and actual scan points. It was implemented by W. Eschen during his Master thesis which I supervised. In the position correction algorithm used here [63], the original scan points are randomly shifted within a certain distance and the set of shifted positions that result

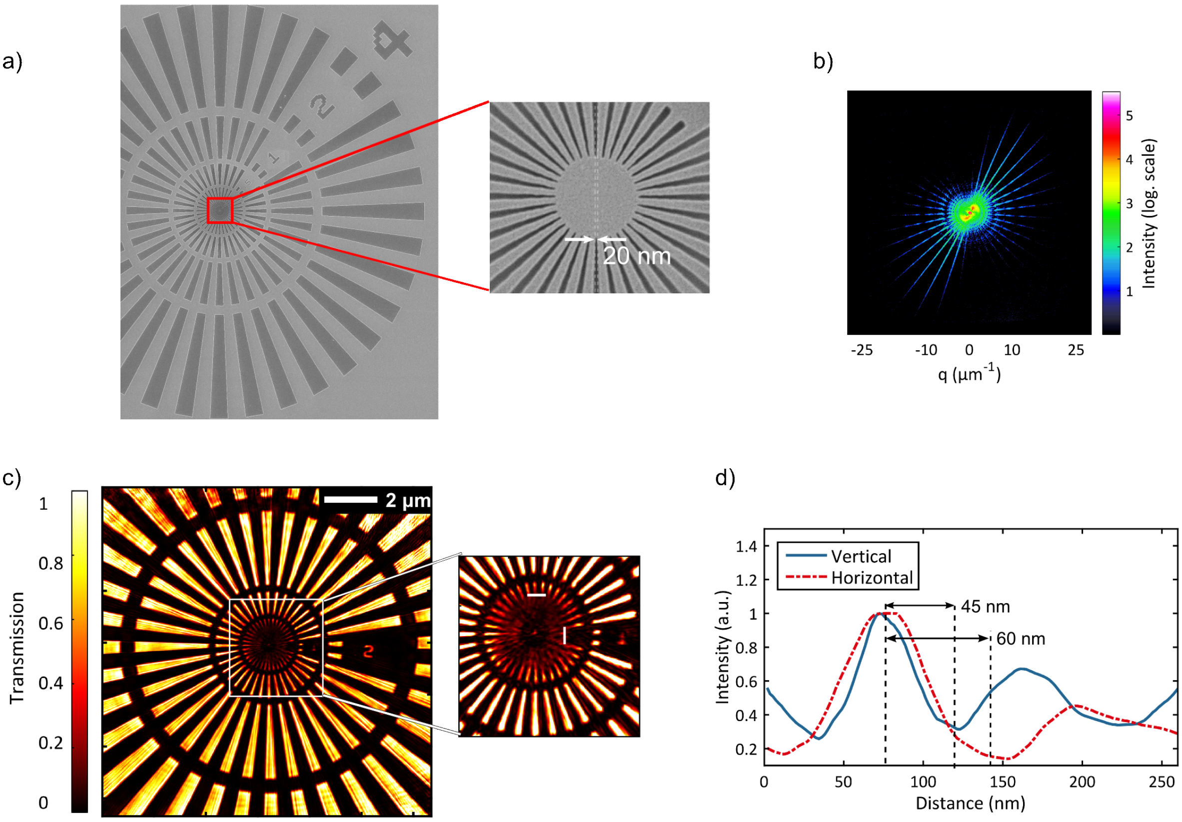

FIGURE 5.2: Results of a high resolution ptychographic measurement. (a) Scanning electron microscope (SEM) image of the Siemens star sample used. Inset shows the innermost ring with a smallest feature size of 20 nm. (b) One of the 51 composite diffraction patterns recorded. (c) The reconstructed intensity over an area $> 10\mu m \times 10\mu m$. The inset shows a rescaled close-up image of the innermost ring within the white square. (d) A horizontal and vertical cross-section along the white lines in the inset of (c).

in the smallest error compared to the measured diffraction pattern are taken. For the reconstruction, 3300 iterations of the difference map (DM) algorithm followed by 950 iterations of the maximum likelihood (ML) algorithm were used. The position correction algorithm was applied in the last 600 iterations of the DM algorithm. No constraints were applied neither on the sample nor on the probe in performing the reconstruction.

The reconstructed object is displayed in Fig. 5.2(c) and shows multiple rings of the Siemens star pattern clearly resolved in a field of view $> 10\ \mu m \times 10\ \mu m$. The inset shows the innermost ring of the Siemens star pattern resolved until about half its radius. The number '1' in the inset with a size of ~ 50 nm $\times$ 250 nm is resolved which gives a rough indication of the achieved resolution. For a more precise resolution estimation, circular cross-sections were taken to identify the minimum radius of the Siemens star pattern where features are resolved. From the Rayleigh criterion, two features are considered resolved if the contrast between the peaks and valleys, $(I_p - I_v)/I_p$, exceeds 0.264. Since we are interested in resolution along different axes for extended samples, the classical Rayleigh criterion had to be modified from its original formulation for point-like objects. The expected number of features have to be identified at a given radius (36 within 360° for our sample). The varying resolution along the horizontal (X) and vertical (Y) directions were accounted for by restricting the range of angles considered to $\pm 20°$ of +X, +Y, -X and -Y. For each direction, cross-sections were taken at the minimum radius where the expected number of features (4 in this case) are resolved. These radii are shown as white lines in the inset of Fig. 5(c). The corresponding cross-sections are displayed in Fig. 5(d) and reveal a half-pitch resolution (the half-distance between two resolved features) of 45 nm along the vertical and 60 nm along the horizontal direction. Although the contrast is larger than 0.264 in both cross-sections, a smaller radius couldn't be taken because the peaks were not faithfully reconstructed anymore. In comparison, a knife-edge test along the sharpest edges gives half-pitch resolutions of 29 nm along the vertical and 45 nm along the horizontal. This validates the discussion earlier that for wavelength-scale features, knife-edge tests could overestimate the achieved resolution unless accompanied by a Fourier space analysis.

5.3.2 Factors limiting the achieved resolution

The intensity of the retrieved probe (Fig. 5.3(a)) shows a horizontally elongated profile and diffraction rings from the beam-constraining pinhole are also visible. The probe beam has a size ($1/e^2$ of the intensity) of 2 μm vertically and is four times larger horizontally. This ellipticity is a result of the astigmatism introduced by the mirror arrangement used to focus the XUV beam on the sample (Fig. 3.7(a)). The phase of the probe beam (Fig. 5.3(b)) is well defined for the high intensity regions of the probe despite the astigmatism of the setup. The circle of least confusion of the astigmatic focus is placed at the beam-constraining pinhole to have the maximum transmission through it. Therefore, the XUV beam propagates few hundred microns after the circle of least confusion to reach the sample resulting in a beam elongated along the horizontal direction. This ellipticity is the reason why the achieved resolution is not isotropic in all directions. Here, the anisotropic resolution results from the dependence of resolution on the longitudinal coherence length of the source as discussed in section 2.3. The relative bandwidth $(\Delta\lambda/\lambda)$ of our source

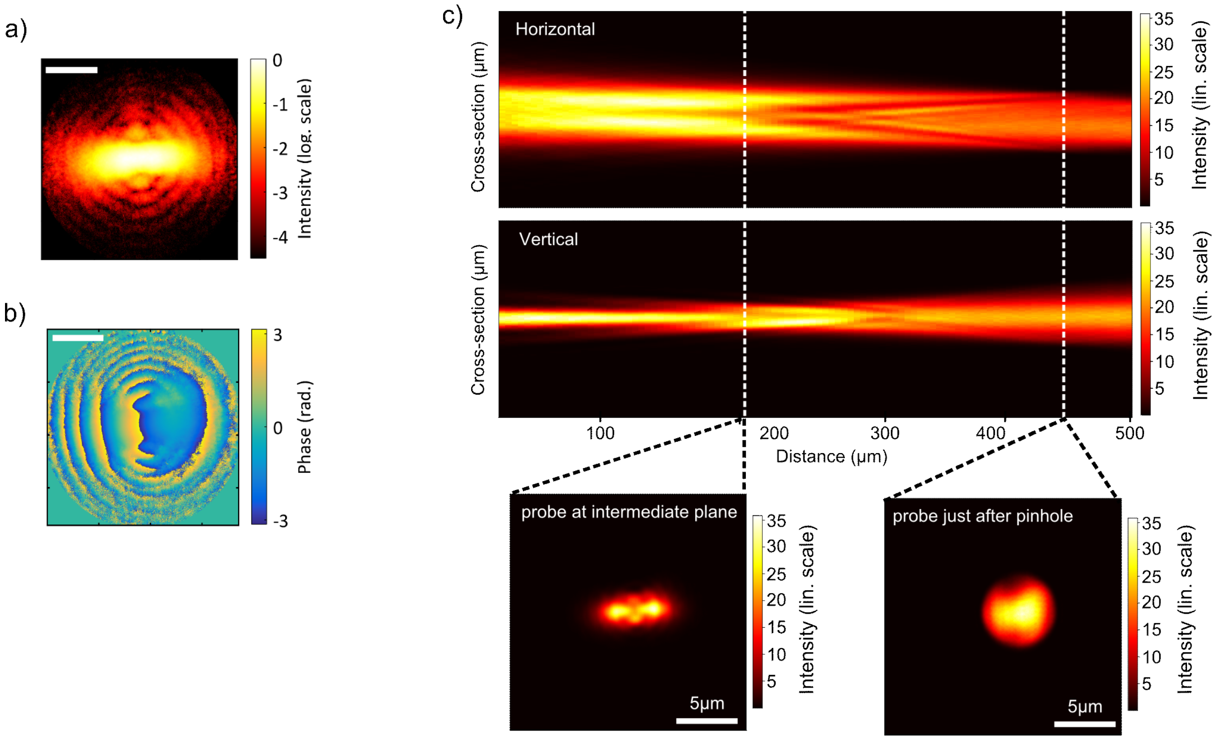

FIGURE 5.3: (a) The intensity profile of the reconstructed probe for the measurement in Fig. 5.2 (shown in log scale for better visibility of the diffraction rings). (b) The reconstructed phase profile. Scale bars in (a) and (b) are 5 μm. (c) Horizontal and vertical cross-sections of the back propagation of the probe beam from the sample plane (z = 0) to the pinhole plane (z = 450 μm). Insets show intensity profiles at an intermediate plane and the pinhole plane.

is limited by the linewidth of the harmonic lines and is estimated to be $\sim 1/150$ for this experiment. Besides bandwidth, the temporal coherence limited resolution is also dependent on the size of the diffracting area (sample size in CDI and probe size in ptychography) as shown in Eq. 2.32. Thus, the resulting temporal coherence limited resolutions are 13 nm for the vertical and 53 nm for the horizontal direction given the current set of parameters. To further illustrate this conclusion, two reconstructions for diffraction patterns cropped to a half and a quarter of the camera size were performed. These reconstructions resulted in comparable resolutions along X and Y directions of $\sim$ 77 nm and $\sim$ 100 nm respectively. The effect of temporal coherence appears at higher diffraction angles which became negligible in the cropped reconstructions.

The evolution of the probe beam can be computed by back-propagating the probe complex amplitude at the sample plane to the beam-constraining pinhole. The angular spectrum

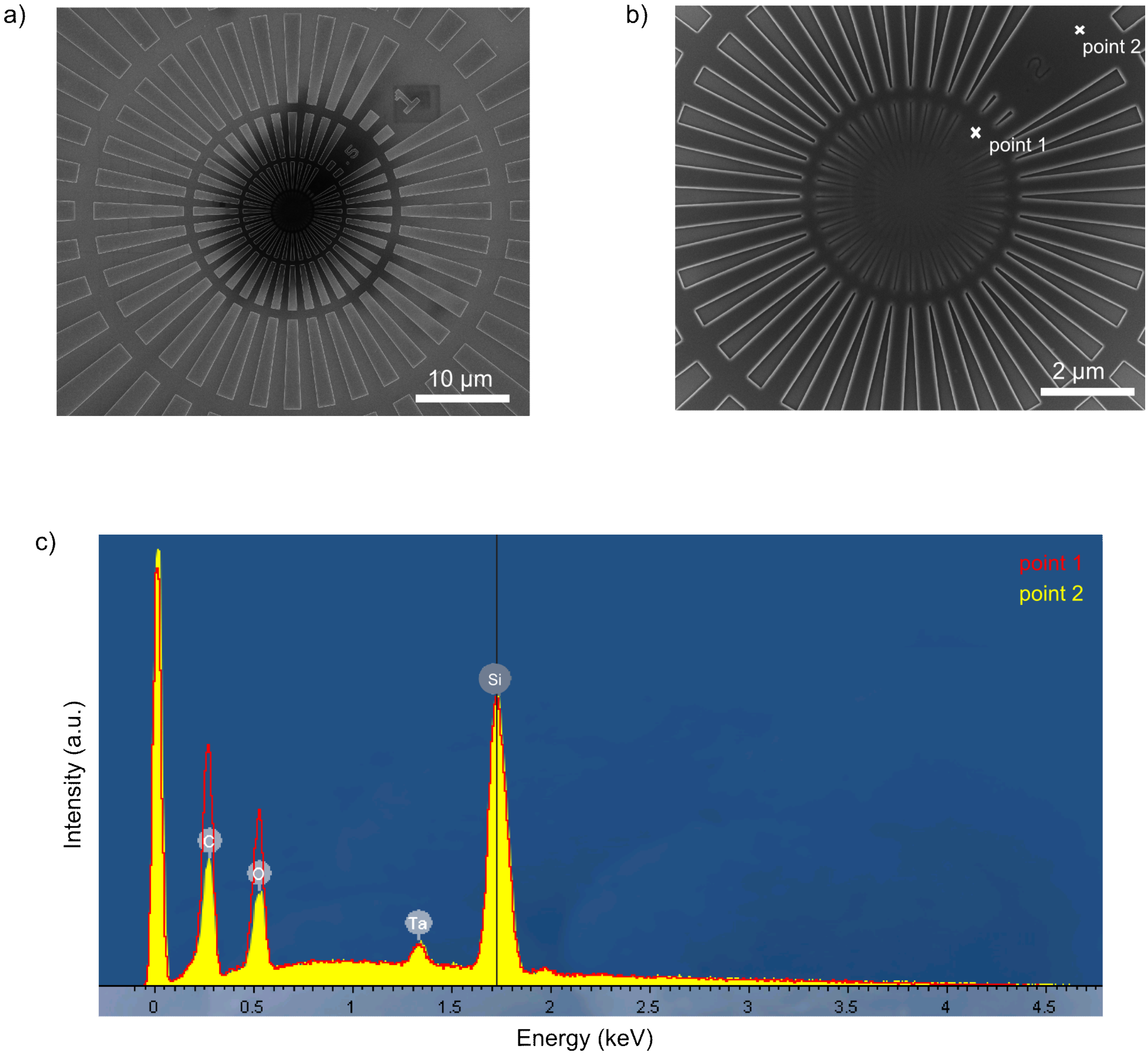

FIGURE 5.4: (a) SEM image of the Siemens star sample after a measurement period of few tens of hours. (b) A close-up look of (a) also showing two markers for the points where energy dispersive X-ray spectroscopy (EDXS) measurements were taken. (c) EDXS measurement at the two points marked in (b) showing different concentrations of oxygen and carbon.

method (section 2.1.1) was used for back-propagation and the vertical/horizontal cross-sections are shown in Fig. 5.3(c). The sample plane is located at a distance of zero and the probe has a diameter of 6 μm at a distance of $\sim$ 450 μm which corresponds to the pinhole plane. It can be seen that the probe will have comparable sizes along X and Y if the sample is placed about 300 μm closer to the pinhole. The sample-pinhole distances was > 400 μm in the experiment due to geometrical constraints of the pinhole/sample holders. More compact designs of XY positioners and sample holders can resolve this issue in the future. The achieved resolution is not limited neither by the Abbe limit (20 nm) nor by the spectral width of the source ($\sim$ 13 nm in the vertical direction). One factor that contributes to limited resolution is waveguiding and it will be discussed in the next section. Uncorrected pointing fluctuations in the XUV beam as well as drifts in the sample/pinhole positioners are also expected to result in performance degradation. While small drifts (< 0.5 μm) in the sample positioner can be compensated by position correction algorithms, drifts in the pinhole positioner result in different probe beam (in amplitude and phase) for different scan points which can't be corrected easily. This violates the formulation of ptychography where the probe is assumed to be constant (Eq. 2.25a) and lowers the reconstruction quality. Scanning Electron Microscopy (SEM) examination of the sample after the experiment shows signs of contamination at its illuminated section (Fig. 5.4(a)). Additional examination using Energy-dispersive X-ray Spectroscopy (EDXS) shows higher accumulation of carbon and oxygen close to the center of the sample compared to outer (less frequently illuminated) regions (Fig. 5.4(c)). As a result, the innermost lines of the Siemens star could be more absorbing and narrower than what is designed thus limiting us from resolving them.

5.3.3 Measurement with higher speed

The high resolution result presented above took a total measurement time of 20 minutes which corresponds to a scanning speed of 5 μm^2/min. The exposure time is the main contribution to the total measurement time in addition to the readout time and the time required for moving the positioners during the scan. The scanning speed can be increased to image a larger area with moderate resolution. This can be applied, for example, to identify regions of interest in a sample that can later be imaged with higher resolution. For faster scanning speed, a single diffraction pattern with an exposure time of 3 seconds was taken at each scan point. Diffraction patterns were taken at 200 scan points and the outer camera pixels were cropped during acquisition to reduce the readout time. Since the diffraction intensity didn't reach these outer pixels, cropping didn't affect the achievable resolution and the new Abbe limit was 51 nm. An area $> 25\ \mu m \times 25\ \mu m$ was imaged with a scanning speed of 20 μm^2/min and the reconstruction is shown in Fig. 5.5(a). The inset shows that the features of the innermost ring are not resolved due to the lower exposure times used. However, its non-zero transmission is visible in comparison to the opaque central region demonstrating the benefit of using a direct resolution test sample like a Siemens star. All features of the second innermost ring with a smallest pitch of 200 nm are resolved. Thus, the achieved half-pitch resolution is better than 100 nm. The reconstructed intensity and phase of the probe beam (Fig. 5.5(b) and (c)) show higher quality than those of the high resolution reconstructions (Fig. 5.3(a) and (b)). This is attributed to lower data corruption from merging of diffraction patterns and lower sample/positioner drifts during acquisition (due to reduced exposure time). The scanning speed attained in this measurement is estimated to be comparable to the fastest measurements reported [13, 123] although exact speeds were not stated in these works. For more transparent membranes, at least one order of magnitude increase in the scanning speed is expected given that the transmission of our current membrane is $< 2\%$.

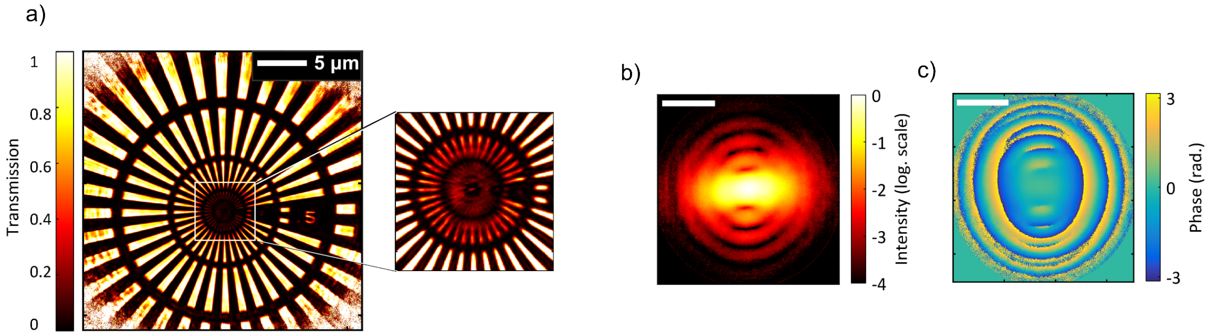

FIGURE 5.5: Ptychographic measurement with a larger field of view. (a) The reconstructed intensity of the Siemens star pattern. Inset shows that the innermost ring is not resolved anymore. (b) and (c) show the intensity and phase of the reconstructed probe respectively (Scale bars are 5 μm).

Previous studies on ptychography have mostly employed periodic or semi-periodic structures (series of lines or zone plates) as a test sample to measure performance of the imaging system [13, 57]. In addition to the issue of using the knife-edge test discussed earlier, ptychographic imaging of periodic structures could give misleading results due to lack of diversity between consecutive scan positions. This is especially relevant when the period of the structure is much smaller than the probe diameter. The diffraction pattern in this case hardly changes for a given scan point and another one shifted by one or more periods of the structure. The reconstruction algorithm can easily find the rough sample features due to its defined periodicity although it might not converge to the correct solution for the sample and probe. Ensuring the probe actually converged by tracking an error metric or characterizing the beam beforehand are suitable methods to improve reliability for periodic samples. Together with my colleagues from the IAP and IOQ Jena, we are preparing a manuscript for publication detailing these issues with particular emphasis on imaging defects in an otherwise periodic sample.

5.4 Beyond the Projection Approximation

As mentioned in the previous section, one physical mechanism limiting the achieved resolution is waveguiding through the features of the sample. Similar to observations in the FTH experiment (section 4.3), waveguiding arises when the sample is not optically thin and the feature size approaches the illuminating wavelength. In this case, the projection approximation is not valid anymore which means the exit wave profile is not simply a product of the sample complex transmission and probe beam complex amplitude. An FDTD simulation of wave propagation through the innermost ring of the Siemens star pattern shows modulations of the exit wave and intensity variations along a single line of the pattern. The fine features of the modulation have sub-pixel sizes beyond the Abbe limit of the setup. In addition, the contrast between consecutive lines decreases towards the center of the pattern making it difficult to resolve them.

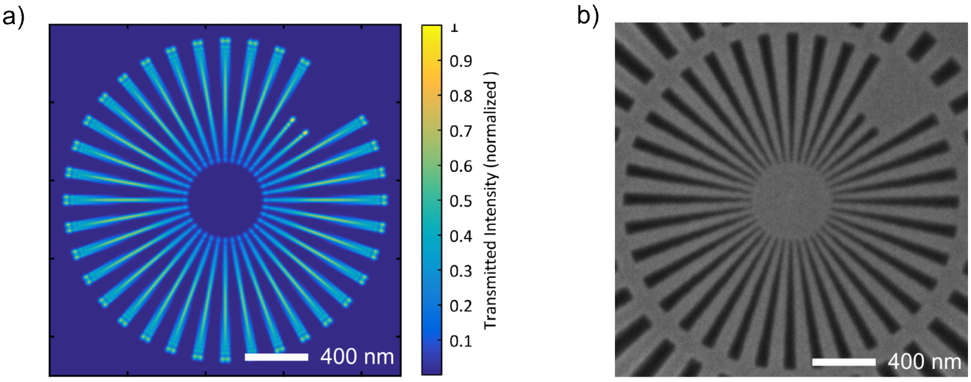

FIGURE 5.6: (a) Exit waves computed using the FDTD method for the etched 100 nm Ta layer on top of a 50 nm Si$_3$N4 layer of the innermost ring of the Siemens star pattern. (b) An SEM image of the innermost ring of the Siemens star pattern used in the measurement shown here for comparison.

However, an even more consequential issue with waveguiding is that it violates the overlap constraint in ptychography described by Eq. 2.25(a). Because the exit wave is no longer given by a multiplication of the probe and sample profiles, decomposition of the exit waves from overlapping illumination regions into a common probe beam and an extended sample region is not accurate anymore. Note that this is not the case in FTH (and CDI) since no such decomposition is necessary and waveguiding doesn't result in an inaccurate reconstruction. It merely modifies the exit wave which is then correctly imaged by FTH or CDI. Models for satisfying the overlap constraint in the presence of waveguiding by propagating through the sample on each iteration of the ptychographic reconstruction will give a more accurate solution. The FDTD method is not practical in this case because of the required complete material model and high computational efforts. A more practical approach is the Multi-slice model suggested by Maiden et al.[66] for transparent samples. The basic idea of the Multi-slice approach method was already proposed earlier by Fleck et al. [128] and was known as fast Fourier transform beam propagation method (FFT-BPM). The 100 nm thick Ta absorber can be modeled by slices of thickness Δz with complex transmission functions computed from the refractive indices of Ta. The illuminating field is multiplied by the complex transmission of a slice and then propagated to the next slice using the angular spectrum method (see supplementary material of [124]). The propagated field is subsequently multiplied by the transmission of the next slice and so on. Comparing the dominant component of the exit wave computed using FDTD and that of the multi-slice approach (Fig. 5.7) shows similar profiles that includes waveguiding effect. However, there is an amplitude error of $\pm 8\%$ introduced by the paraxial approximation inherent in the multi-slice method. This error is pronounced by the strong sample-probe interaction which in turn comes from the strong contrast between the sample's features. In addition, polarization effects (differences between transmissions of the horizontal and vertical features) observed in the FDTD result were not observable in the multi-slice computation. In principle, the multi-slice approach can be incorporated in ptychographic reconstructions for more accurate results (especially for samples with weaker contrast) but this is beyond the scope of this work.

To summarize, a more reliable object space criterion was employed in this work to reliably characterize ptychographic imaging setups. The smallest resolved features in table-top ptychography with sizes of 45 nm were imaged in a field of view $> 10\mu m \times 10\mu m$. Interferometric stabilization of the sample/pinhole positioners and samples on suitable membranes will significantly improve imaging performance in the future. The effect of waveguiding can be reduced by using shorter wavelength illumination which will also improve the achievable resolution. For photon energies $> 120\ eV$, fiber laser driven HHG sources have already demonstrated photon flux $> 10^9$ photons/second. Alternatively, imaging in the reflection mode will also reduce waveguiding and issues with low transmission. Imaging of semiconductor structures and mask inspection will benefit from the ptychographic

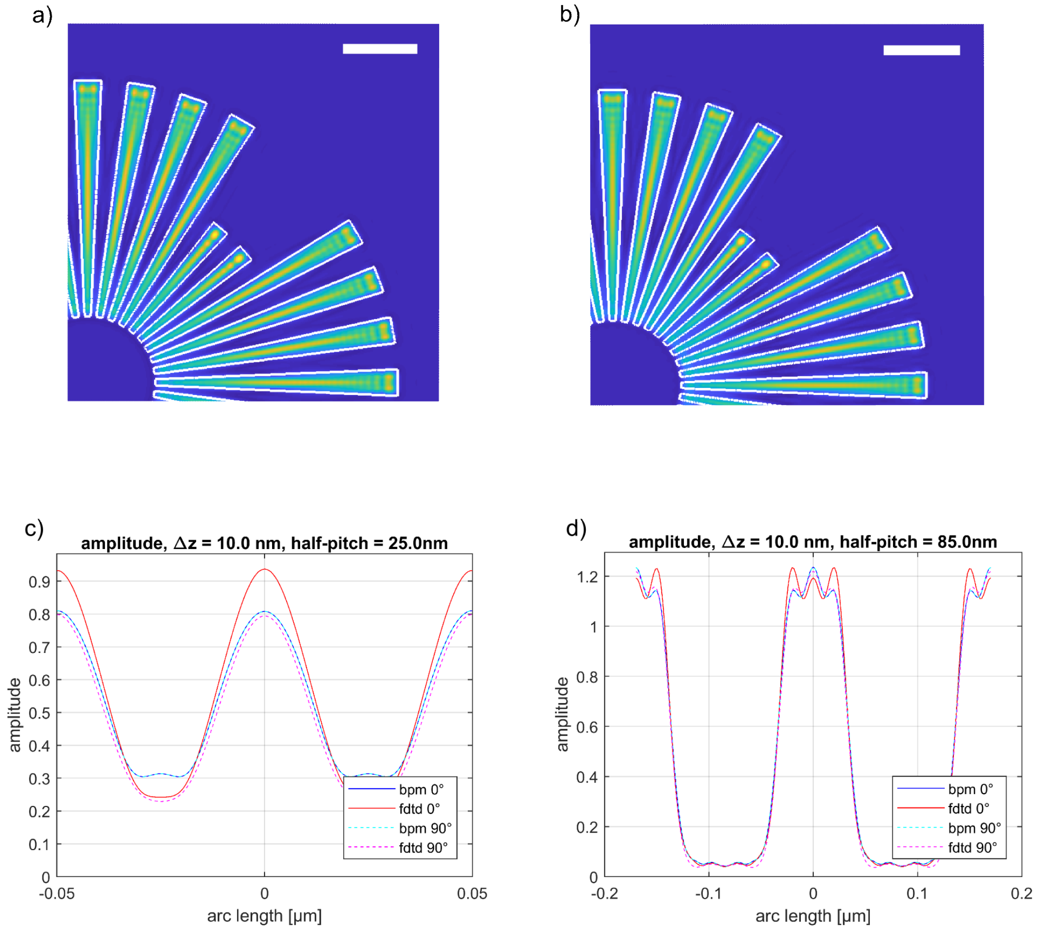

FIGURE 5.7: Comparison of exit waves from the innermost ring of the Siemens star sample computed using (a) the FDTD method and (b) the multi-slice (bpm) approach. (c) Circular cross-sections taken at regions in the sample where the half-pitch feature size is 25 nm for an illumination that is vertically and horizontally polarized. (d) Same as in (c) for regions with half-pitch feature size of 85 nm.

imaging results presented in this chapter since the wavelength (18 nm) lies within the silicon transmission window.

Using HHG sources at 90 eV (13.5 nm), inspection of EUV lithographic masks can be performed at the wavelength with which the masks are used in illuminating the photoresist. This is known as actinic (at-wavelength) imaging of lithographic masks and has advantages over other mask inspection techniques (e.g. SEM, DUV, . . .) [129]. A cross-section of a typical EUV lithographic mask is shown in Fig. 5.8(a) and consists of a patterned absorber on top of a multi-layer structure for efficient reflection at 13.5 nm. An optional pellicle is placed above the absorber for protection purposes. Compared to inspection in

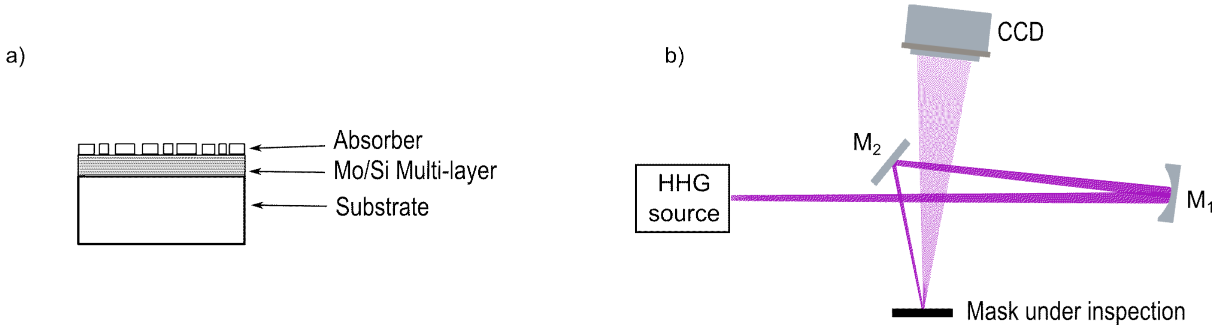

FIGURE 5.8: (a) Cross-section of a typical mask in EUV lithography. (b) Schematic diagram of a reflection-mode ptychographic imaging setup for use in inspection of EUV lithographic masks. M1 and M2 are multi-layer mirrors designed for efficient reflection at 13.5 nm.

the DUV spectral range, the multi-layer has higher reflectivity and inspection through the protective pellicle is also possible in actinic imaging. In addition, ability to detect phase defects and higher resolution are some of the advantages of actinic imaging. However, most actinic mask inspection tools currently used are conventional full-field EUV microscopes operating at 13.5 nm [130, 131]. Employing ptychography in an actinic EUV mask inspection can further improve the resolution in addition to direct identification of amplitude and phase defects [132]. A schematic diagram of such a ptychographic EUV mask inspection tool is shown in Fig. 5.8(b). It is operated in reflection and uses two multi-layer mirrors for spectral selection and focusing (similar to the transmission setup in Fig. 3.7). Together with a high photon flux 13.5 nm HHG source currently under development in our group, this ptychographic setup could deliver a high resolution and table-top EUV mask inspection tool for use in the semiconductor industry.

Chapter 6

Summary and Outlook

Coherent diffractive imaging (CDI) techniques using sources in the XUV/X-ray spectral range are a valuable tool in bridging the gap between visible light microscopes and electron/ion microscopes. These techniques are capable of higher penetration depths compared to electron microscopes while still being able to achieve few nanometers of resolution. Despite these advantages, a high performance table-top setup was not available so far and most CDI experiments were conducted at large scale facilities like synchrotrons and X-ray free electron lasers (XFELs). Achieving higher resolution in a table top and more accessible CDI setup presented challenges that stem partly from limited coherent flux and unique propagation effects in wavelength-sized features. Previous works in table top CDI required impractically high exposure times and relied on knife-edge (10/90) tests for resolution estimation which can be unreliable given the iterative nature of the phasing algorithms. This made it difficult to gauge their improvement in performance and the readiness for real world applications. In this work, I aimed at pushing the performance of table-top CDI setups using high photon flux HHG sources driven by state-of-the-art femtosecond fiber laser systems. The high photon flux and high coherence of the source together with optimized imaging setups and reconstruction algorithms enabled record-high resolutions in the different CDI modalities.

In a conventional CDI experiment, subwavelength resolution of 13 nm was demonstrated using an HHG source at 18 nm wavelength delivering record-high photon flux with excellent coherence properties. This is the highest resolution achieved for a table-top CDI setup in the XUV/X-ray spectral range. In addition, a half-pitch resolution of < 30 nm was achieved using a measurement with only 3 seconds of exposure time which demonstrates the potential of high speed table top imaging. The achieved subwavelength resolution was only limited by the wavelength and detector size since the high photon flux allowed for measurement at high NA. It is, therefore, scalable to even better resolution values by employing shorter wavelength HHG sources. In that regard, the first CDI experiment in the soft X-ray spectral region at 8 nm wavelength was presented and it already achieved a moderate resolution of ~ 50 nm. The resolution in this experiment was mainly limited by the available flux for imaging. Since then, driving fiber laser systems at 1 μm wavelength have demonstrated average powers > 3 kW, pulse energies > 12 mJ using coherent combination of multiple amplifier channels [90, 133] and compressed few cycle pulses at > 200W of average power [116]. With these systems and novel methods for separating the harmonics from the driving laser [109], sub-10 nm resolutions are within reach in the near future. Algorithmic approaches, e.g. reconstructions for limited coherence [71] and deep learning neural networks [134], can also be incorporated to further improve the resolution or reconstruction speed.

Wavefront measurement in the XUV is an important tool in determining whether the XUV beam focus has the required size and phase flatness for a particular CDI modality. This information helps in adjusting the generating conditions during the HHG process or modifying the focusing geometry for lower aberrations. A wavefront sensor suitable for characterizing XUV beams in a single shot was developed using a conventional CDI technique. The proof-of-principle experiment conducted in the visible spectral range was able to recover the phase profile of a HeNe laser beam across its focus. Although a detailed quantitative comparison with an ideal Gaussian focus was not possible, the qualitative evolution of the phase profile across a Gaussian focus was clearly observable. In the XUV, the experimental parameters are more suited for a CDI setup and the developed wavefront sensor can easily be demonstrated using appropriate mask dimensions. This can greatly improve robustness of future imaging setups since the mask can easily be included in an already running experiment for live monitoring of beam properties.

A holographic implementation of CDI, known as Fourier transform holography (FTH), is an elegant approach to increase the robustness and speed of the reconstruction by encoding the phase information on the diffraction pattern itself. The highest resolution achieved in an FTH experiment using table-top sources was 89 nm and required hours of exposure time to record a hologram [11]. By using the latest technology in nanofabrication to etch reference holes with diameters of just 50 nm and the high photon flux available from our HHG source, the highest resolution FTH experiment was conducted with a half-pitch resolution of 34 nm with only seconds of exposure time. Further refinement of the resolution using iterative phase retrieval enabled features with a half-distance of 23 nm to be resolved. These are the smallest features ever resolved in a table-top XUV/X-ray imaging system. The significance of this result lies in the difference between a knife-edge (10/90) test and resolving of small features. This difference originates from propagation effects observed in the reconstructed images that result in modulation of exit wave profiles and reduction in transmission. These propagation effects were found to be a result of waveguiding in wavelength-sized features for optically thick samples and the conclusion was verified by a finite difference time domain (FDTD) simulation. In addition to modifying the image profile, waveguiding was also found to limit the achievable resolution and image contrast in wavelength-sized features. The record-high resolution values and the reduction of exposure times from hours to minutes promises wider application of FTH for samples where conventional CDI might not be robust in image reconstruction. Weak contrast biological samples with complex features as well as time-resolved imaging of magnetization dynamics are some examples where FTH is the preferred modality.

Conventional CDI and FTH are applicable only for samples isolated in a given area that is few microns in size for typical XUV setups. Ptychography is the extension to conventional CDI that enables imaging of extended samples and exciting results were already reported using synchrotron light sources [8, 9]. Although subwavelength resolutions were claimed [13], table-top ptychography setups were not able to resolve sub-100 nm features and reliability was an issue due to the performance metrics chosen. In this work, an extended Siemens star pattern was imaged with wavelength-scale resolution to reliably demonstrate the potential of table-top setups in future applications. Sub-50 nm features were resolved for the first time using a table-top setup on an area larger than 10 μm by 10 μm. The feasibility of imaging thick samples susceptible to waveguiding using the multi-slice approach was also illustrated. An order of magnitude increase in scanning speed or a doubling of the resolution is achievable by replacing the opaque membrane used in the present case. Although a more robust and more general modality, ptychography has additional requirements on the source, positioners and other experimental parameters that contribute in limiting the achievable resolution. Improved focusing geometry for smaller focal sizes, live beam profile monitoring using the wavefront sensor developed here and interferometric stabilization of sample positioners are some of the minor changes that can give significant performance improvements. Integration with tomographic techniques, which is yet to be demonstrated in a table-top setup, will further widen the application of ptychography to imaging 3D structures. Ptychography at 13.5 nm is being investigated for high resolution actinic (at-wavelength) inspection of EUV lithography masks mainly at synchrotron facilities [132]. However, ptychographic EUV mask inspection tools on a table-top setup still require more powerful sources for achieving high resolution in reasonable measurement times [135, 136]. Using Ne gas targets and few cycle driving lasers, a photon flux of $> 3 \times 10^9$ photons/(s·1% BW) has already been demonstrated at 13.5 nm in a fiber laser system similar to that used in this work. With the increase in driving laser power, this source can deliver the required flux to enable ptychography experiments with higher scan speeds. By switching to ptychography in reflection mode, a promising tool for table-top EUV mask inspection can be developed with resolution better than the currently available tools based on conventional EUV microscopy [130, 131].

In a different application area, biological samples can be imaged with higher contrast in the spectral range where water is relatively transmitting and carbon (organic specimen) is absorbing. Commonly known as the water window between 280 eV and 530 eV, coherent sources in this spectral range are of high interest for high resolution imaging of biological samples. First experiments in our group using thulium-doped driving lasers at 2 μm wavelength generated $> 10^4$ photons/second in the water window. Recent demonstrations from Tm-doped fiber laser systems with few cycle pulses at > 40W of average power [137] and femtosecond laser systems with kW level average powers [138] are expected to yield even higher HHG flux for imaging in the water window. From a temporal point of view, HHG sources have the advantage of delivering pulses with femtosecond to attosecond durations that can be used in probing the dynamics of ultrafast processes [139, 140]. In addition, the phases of the driving laser and the generated harmonics are locked which can be exploited in pump-probe type of experiments with temporal resolutions beyond the current capabilities of synchrotron facilities. In combination with the ever increasing spatial resolution of CDI techniques, imaging of ultrafast electron and magnetization dynamics, heat and energy transport as well as dissociation dynamics of variety of molecular species can be studied with femtosecond to attosecond temporal resolutions [14, 15, 141].

Bibliography

[1] Kaulich, B., Thibault, P., Gianoncelli, A., and Kiskinova, M. *Journal of Physics: Condensed Matter* **23**(8), 083002 mar (2011).

[2] Sakdinawat, A. and Attwood, D. *Nature Photonics* **4**(12), 840–848 dec (2010).

[3] Abbe, E. *Archiv für Mikroskopische Anatomie* **9**, 413–468 (1873).

[4] Chao, W., Fischer, P., Tyliszczak, T., Rekawa, S., Anderson, E., and Naulleau, P. *Optics Express* **20**(9), 9777 apr (2012).

[5] Sydor, A. M., Czymmek, K. J., Puchner, E. M., and Mennella, V. *Trends in Cell Biology* **25**(12), 730–748 dec (2015).

[6] Miao, J., Charalambous, P., Kirz, J., and Sayre, D. *Nature* **400**(6742), 342–344 jul (1999).

[7] Takahashi, Y., Nishino, Y., Tsutsumi, R., Zettsu, N., Matsubara, E., Yamauchi, K., and Ishikawa, T. *Physical Review B* **82**(21), 214102 dec (2010).

[8] Shapiro, D. A., Yu, Y.-S., Tyliszczak, T., Cabana, J., Celestre, R., Chao, W., Kaznatcheev, K., Kilcoyne, A. L. D., Maia, F., Marchesini, S., Meng, Y. S., Warwick, T., Yang, L. L., and Padmore, H. A. *Nature Photonics* **8**(10), 765–769 oct (2014).

[9] Holler, M., Guizar-Sicairos, M., Tsai, E. H. R., Dinapoli, R., Müller, E., Bunk, O., Raabe, J., and Aeppli, G. *Nature* **543**(7645), 402–406 mar (2017).

[10] Jiang, H., Song, C., Chen, C.-C., Xu, R., Raines, K. S., Fahimian, B. P., Lu, C.-H., Lee, T.-K., Nakashima, A., Urano, J., Ishikawa, T., Tamanoi, F., and Miao, J. *Proceedings of the National Academy of Sciences of the United States of America* **107**(25), 11234–9 jun (2010).

[11] Sandberg, R. L., Raymondson, D. A., La-o vorakiat, C., Paul, A., Raines, K. S., Miao, J., Murnane, M. M., Kapteyn, H. C., and Schlotter, W. F. *Optics Letters* **34**(11), 1618 jun (2009).

[12] Seaberg, M. D., Adams, D. E., Townsend, E. L., Raymondson, D. A., Schlotter, W. F., Liu, Y., Menoni, C. S., Rong, L., Chen, C.-C., Miao, J., Kapteyn, H. C., and Murnane, M. M. *Optics express* **19**(23), 22470–9 nov (2011).

[13] Gardner, D. F., Tanksalvala, M., Shanblatt, E. R., Zhang, X., Galloway, B. R., Porter, C. L., Karl Jr, R., Bevis, C., Adams, D. E., Kapteyn, H. C., Murnane, M. M., and Mancini, G. F. *Nature Photonics* **11**(4), 259–263 mar (2017).

[14] von Korff Schmising, C., Pfau, B., Schneider, M., Günther, C., Giovannella, M., Perron, J., Vodungbo, B., Müller, L., Capotondi, F., Pedersoli, E., Mahne, N., Lüning, J., and Eisebitt, S. *Physical Review Letters* **112**(21), 217203 may (2014).

[15] Siemens, M. E., Li, Q., Yang, R., Nelson, K. A., Anderson, E. H., Murnane, M. M., and Kapteyn, H. C. *Nature Materials* **9**(1), 26–30 jan (2010).

[16] Rothhardt, J., Hädrich, S., Klenke, A., Demmler, S., Hoffmann, A., Gotschall, T., Eidam, T., Krebs, M., Limpert, J., and Tünnermann, A. *Optics letters* **39**(17), 5224–7 sep (2014).

[17] Ding, C., Xiong, W., Fan, T., Hickstein, D. D., Popmintchev, T., Zhang, X., Walls, M., Murnane, M. M., and Kapteyn, H. C. *Optics express* **22**(5), 6194–202 mar (2014).

[18] Klas, R., Demmler, S., Tschernajew, M., Hädrich, S., Shamir, Y., Tünnermann, A., Rothhardt, J., and Limpert, J. *Optica* **3**(11), 1167 nov (2016).

[19] Zayko, S., Mönnich, E., Sivis, M., Mai, D.-D., Salditt, T., Schäfer, S., and Ropers, C. *Optics Express* **23**(15), 19911 jul (2015).

[20] Goodman, J. W. *Introduction to Fourier Optics.* Third edition, (2005).

[21] Born, M. and Wolf, E. *Principles of Optics : electromagnetic theory of propagation, interference and diffraction of light.* Cambridge University Press, sixth edition, (1998).

[22] Shen, F. and Wang, A. *Applied Optics* **45**(6), 1102 feb (2006).

[23] Sawada, H., Shimura, N., Hosokawa, F., Shibata, N., and Ikuhara, Y. *Microscopy* **64**(3), 213–217 jun (2015).

[24] Bartesaghi, A., Merk, A., Banerjee, S., Matthies, D., Wu, X., Milne, J. L. S., and Subramaniam, S. *Science (New York, N.Y.)* **348**(6239), 1147–51 jun (2015).

[25] Attwood, D. *Soft X-rays and Extreme Ultraviolet Radiation.* Cambridge University Press, (2007).

[26] Rösner, B., Koch, F., Döring, F., Guzenko, V. A., Meyer, M., Ornelas, J. L., Späth, A., Fink, R. H., Stanescu, S., Swaraj, S., Belkhou, R., Watts, B., Raabe, J., and David, C. *Microscopy and Microanalysis* **24**(S2), 272–273 aug (2018).

[27] Chapman, H. N., Barty, A., Marchesini, S., Noy, A., Hau-Riege, S. P., Cui, C., Howells, M. R., Rosen, R., He, H., Spence, J. C. H., Weierstall, U., Beetz, T., Jacobsen, C., and Shapiro, D. *Journal of the Optical Society of America A* **23**(5), 1179 may (2006).

[28] Sandberg, R. L., Song, C., Wachulak, P. W., Raymondson, D. A., Paul, A., Amirbekian, B., Lee, E., Sakdinawat, A. E., La-O-Vorakiat, C., Marconi, M. C., Menoni, C. S., Murnane, M. M., Rocca, J. J., Kapteyn, H. C., and Miao, J. *Proceedings of the National Academy of Sciences of the United States of America* **105**(1), 24–7 jan (2008).

[29] Sayre, D. *Acta Crystallographica* **5**(6), 843–843 nov (1952).

[30] Shannon, C. *Proceedings of the IRE* **37**(1), 10–21 jan (1949).

[31] Bates, R. *Optik (Stuttgart)* **61**, 247–262 (1982).

[32] Barakat, R. and Newsam, G. *Journal of Mathematical Physics* **25**(11), 3190–3193 nov (1984).

[33] Miao, J., Ishikawa, T., Anderson, E. H., and Hodgson, K. O. *Physical Review B* **67**(17), 174104 may (2003).

[34] Gerchberg, R. W. and Saxton, W. O. *Optik* **34**(3), 275–283 (1972).

[35] Fienup, J. R. *Optics Letters* **3**(1), 27 jul (1978).

[36] Fienup, J. R. *Journal of the Optical Society of America A* **4**(1), 118 jan (1987).

[37] He, H., Marchesini, S., Howells, M., Weierstall, U., Hembree, G., and Spence, J. C. H. *Acta Crystallographica Section A Foundations of Crystallography* **59**(2), 143–152 mar (2003).

[38] Marchesini, S., He, H., Chapman, H. N., Hau-Riege, S. P., Noy, A., Howells, M. R., Weierstall, U., and Spence, J. C. H. *Physical Review B* **68**(14), 140101 oct (2003).

[39] Fienup, J. R. *Applied Optics* **21**(15), 2758 aug (1982).

[40] Luke, D. R. *Inverse Problems* **21**(1), 37–50 feb (2005).

[41] Miao, J., Chen, C.-C., Song, C., Nishino, Y., Kohmura, Y., Ishikawa, T., Ramunno-Johnson, D., Lee, T.-K., and Risbud, S. H. *Physical Review Letters* **97**(21), 215503 nov (2006).

[42] Guizar-Sicairos, M. and Fienup, J. R. *Journal of the Optical Society of America A* **29**(11), 2367 nov (2012).

[43] Fienup, J. R. and Wackerman, C. C. *Journal of the Optical Society of America A* **3**(11), 1897 nov (1986).

[44] GABOR, D. *Nature* **161**(4098), 777–778 may (1948).

[45] Bartels, R. A., Paul, A., Green, H., Kapteyn, H. C., Murnane, M. M., Backus, S., Christov, I. P., Liu, Y., Attwood, D., and Jacobsen, C. *Science* **297**(5580), 376 jul (2002).

[46] Genoud, G., Guilbaud, O., Mengotti, E., Pettersson, S.-G., Georgiadou, E., Pourtal, E., Wahlström, C.-G., and L'Huillier, A. *Applied Physics B* **90**(3-4), 533–538 mar (2008).

[47] Denis, L., Fournier, C., Fournel, T., and Ducottet, C. *Measurement Science and Technology* **19**(7), 074004 jul (2008).

[48] Schlotter, W. F. *Lensless Fourier transform holography with soft x-rays.* PhD thesis, Stanford University, (2007).

[49] Schlotter, W. F., Rick, R., Chen, K., Scherz, A., Stöhr, J., Lüning, J., Eisebitt, S., Günther, C., Eberhardt, W., Hellwig, O., and McNulty, I. *Applied Physics Letters* **89**(16), 163112 oct (2006).

[50] Gauthier, D., Guizar-Sicairos, M., Ge, X., Boutu, W., Carré, B., Fienup, J. R., and Merdji, H. *Physical Review Letters* **105**(9), 093901 aug (2010).

[51] Zhu, D., Guizar-Sicairos, M., Wu, B., Scherz, A., Acremann, Y., Tyliszczak, T., Fischer, P., Friedenberger, N., Ollefs, K., Farle, M., Fienup, J. R., and Stöhr, J. *Physical Review Letters* **105**(4), 043901 jul (2010).

[52] Tenner, V. T., Eikema, K. S. E., and Witte, S. *Optics Express* **22**(21), 25397 oct (2014).

[53] Boutu, W., Gauthier, D., Ge, X., Cassin, R., Ducousso, M., Gonzalez, A., Iwan, B., Samaan, J., Wang, F., Kovačev, M., and Merdji, H. *Optics Express* **24**(6), 6318 mar (2016).

[54] Marchesini, S., Boutet, S., Sakdinawat, A. E., Bogan, M. J., Bajt, S., Barty, A., Chapman, H. N., Frank, M., Hau-Riege, S. P., Szöke, A., Cui, C., Shapiro, D. A., Howells, M. R., Spence, J. C. H., Shaevitz, J. W., Lee, J. Y., Hajdu, J., and Seibert, M. M. *Nature Photonics* **2**(9), 560–563 sep (2008).

[55] Hoppe, W. *Acta Crystallographica Section A* **25**(4), 495–501 jul (1969).

[56] Rodenburg, J. M. and Faulkner, H. M. L. *Applied Physics Letters* **85**(20), 4795–4797 nov (2004).

[57] Rodenburg, J. M., Hurst, A. C., Cullis, A. G., Dobson, B. R., Pfeiffer, F., Bunk, O., David, C., Jefimovs, K., and Johnson, I. *Physical Review Letters* **98**(3), 034801 jan (2007).

[58] Bunk, O., Dierolf, M., Kynde, S., Johnson, I., Marti, O., and Pfeiffer, F. *Ultramicroscopy* **108**(5), 481–487 apr (2008).

[59] Maiden, A. M. and Rodenburg, J. M. *Ultramicroscopy* **109**(10), 1256–1262 sep (2009).

[60] Thibault, P., Dierolf, M., Bunk, O., Menzel, A., and Pfeiffer, F. *Ultramicroscopy* **109**(4), 338–343 mar (2009).

[61] Guizar-Sicairos, M. and Fienup, J. R. *Optics Express* **16**(10), 7264 may (2008).

[62] Elser, V., Rankenburg, I., and Thibault, P. *Proceedings of the National Academy of Sciences of the United States of America* **104**(2), 418–23 jan (2007).

[63] Maiden, A., Humphry, M., Sarahan, M., Kraus, B., and Rodenburg, J. *Ultramicroscopy* **120**, 64–72 sep (2012).

[64] Enders, B. and Thibault, P. *Proceedings of the Royal Society A: Mathematical, Physical and Engineering Science* **472**(2196), 20160640 dec (2016).

[65] Zhang, F., Peterson, I., Vila-Comamala, J., Diaz, A., Berenguer, F., Bean, R., Chen, B., Menzel, A., Robinson, I. K., and Rodenburg, J. M. *Optics Express* **21**(11), 13592 jun (2013).

[66] Maiden, A. M., Humphry, M. J., and Rodenburg, J. M. *Journal of the Optical Society of America A* **29**(8), 1606 aug (2012).

[67] Goodman, J. W. *Statistical optics.* John Wiley & Sons,, second edition, (2015).

[68] González, A. I. and Mejía, Y. *Journal of the Optical Society of America A* **28**(6), 1107 jun (2011).

[69] Spence, J., Weierstall, U., and Howells, M. *Ultramicroscopy* **101**(2-4), 149–152 nov (2004).

[70] Clark, J. N. and Peele, A. G. *Applied Physics Letters* **99**(15), 154103 oct (2011).

[71] Thibault, P. and Menzel, A. *Nature* **494**(7435), 68–71 feb (2013).

[72] van der Veen, F. and Pfeiffer, F. *Journal of Physics: Condensed Matter* **16**(28), 5003–5030 jul (2004).

[73] Abbey, B., Whitehead, L. W., Quiney, H. M., Vine, D. J., Cadenazzi, G. A., Henderson, C. A., Nugent, K. A., Balaur, E., Putkunz, C. T., Peele, A. G., Williams, G. J., and McNulty, I. *Nature Photonics* **5**(7), 420–424 jul (2011).

[74] Enders, B., Dierolf, M., Cloetens, P., Stockmar, M., Pfeiffer, F., and Thibault, P. *Applied Physics Letters* **104**(17), 171104 apr (2014).

[75] Bilderback, D. H., Elleaume, P., and Weckert, E. *Journal of Physics B: Atomic, Molecular and Optical Physics* **38**(9), S773–S797 may (2005).

[76] McNeil, B. W. J. and Thompson, N. R. *Nature Photonics* **4**(12), 814–821 dec (2010).

[77] Miao, J., Ishikawa, T., Robinson, I. K., and Murnane, M. M. *Science (New York, N.Y.)* **348**(6234), 530–5 may (2015).

[78] Vartanyants, I. A. and Singer, A. *Synchrotron Light Sources and Free-Electron Lasers: Accelerator Physics, Instrumentation and Science Applications* , 1–38 (2014).

[79] Daido, H. *Reports on Progress in Physics* **65**(10), 1513–1576 oct (2002).

[80] Jansson, P. A. C., Vogt, U., and Hertz, H. M. *Review of Scientific Instruments* **76**(4), 043503 apr (2005).

[81] Legall, H., Blobel, G., Stiel, H., Sandner, W., Seim, C., Takman, P., Martz, D. H., Selin, M., Vogt, U., Hertz, H. M., Esser, D., Sipma, H., Luttmann, J., Höfer, M., Hoffmann, H. D., Yulin, S., Feigl, T., Rehbein, S., Guttmann, P., Schneider, G., Wiesemann, U., Wirtz, M., and Diete, W. *Optics Express* **20**(16), 18362 jul (2012).

[82] Odstrcil, M., Bussmann, J., Rudolf, D., Bresenitz, R., Miao, J., Brocklesby, W. S., and Juschkin, L. *Optics Letters* **40**(23), 5574 dec (2015).

[83] Ferray, M., L'Huillier, A., and Li, X. *Journal of Physics B: Atomic, Molecular and Optical Physics* **21**, L31–L35 (1988).

[84] L'Huillier, A. and Balcou, P. *Physical Review Letters* **70**(6), 774–777 feb (1993).

[85] Popmintchev, T., Chen, M.-C., Popmintchev, D., Arpin, P., Brown, S., Alisauskas, S., Andriukaitis, G., Balciunas, T., Mücke, O. D., Pugzlys, A., Baltuska, A., Shim, B., Schrauth, S. E., Gaeta, A., Hernández-García, C., Plaja, L., Becker, A., Jaron-Becker, A., Murnane, M. M., and Kapteyn, H. C. *Science (New York, N.Y.)* **336**(6086), 1287–91 jun (2012).

[86] Chen, M.-C., Arpin, P., Popmintchev, T., Gerrity, M., Zhang, B., Seaberg, M., Popmintchev, D., Murnane, M. M., and Kapteyn, H. C. *Physical Review Letters* **105**(17), 173901 oct (2010).

[87] Tadesse, G. K., Klas, R., Demmler, S., Hädrich, S., Wahyutama, I., Steinert, M., Spielmann, C., Zürch, M., Pertsch, T., Tünnermann, A., Limpert, J., and Rothhardt, J. *Optics Letters* **41**(22), 5170 nov (2016).

[88] Chini, M., Zhao, K., and Chang, Z. *Nature Photonics* **8**(3), 178–186 mar (2014).

[89] Cousin, S. L., Silva, F., Teichmann, S., Hemmer, M., Buades, B., and Biegert, J. *Optics Letters* **39**(18), 5383 sep (2014).

[90] Müller, M., Klenke, A., Steinkopff, A., Stark, H., Tünnermann, A., and Limpert, J. *Optics Letters* **43**(24), 6037 dec (2018).

[91] Boyd, R. W. *Nonlinear Optics*. Elsevier, second edition, (2003).

[92] Kulander, K. C., Schafer, K. J., and Krause, J. L. 95–110. Springer, Boston, MA (1993).

[93] Corkum, P. B. *Physical Review Letters* **71**(13), 1994–1997 sep (1993).

[94] Krause, J. L., Schafer, K. J., and Kulander, K. C. *Physical Review Letters* **68**(24), 3535–3538 jun (1992).

[95] Lewenstein, M., Balcou, P., Ivanov, M. Y., L'Huillier, A., and Corkum, P. B. *Physical Review A* **49**(3), 2117–2132 mar (1994).

[96] Shiner, A. D., Trallero-Herrero, C., Kajumba, N., Bandulet, H.-C., Comtois, D., Légaré, F., Giguère, M., Kieffer, J.-C., Corkum, P. B., and Villeneuve, D. M. *Physical Review Letters* **103**(7), 073902 aug (2009).

[97] Chang, Z. *Fundamentals of Attosecond Optics*. CRC Press, feb (2011).

[98] Rundquist, A., Durfee, C. G., Chang, Z., Herne, C., Backus, S., Murnane, M. M., and Kapteyn, H. C. *Science (New York, N.Y.)* **280**(5368), 1412–5 may (1998).

[99] Rothhardt, J., Krebs, M., Hädrich, S., Demmler, S., Limpert, J., and Tünnermann, A. *New Journal of Physics* **16**(3), 033022 mar (2014).

[100] Klenke, A., Hädrich, S., Eidam, T., Rothhardt, J., Kienel, M., Demmler, S., Gottschall, T., Limpert, J., and Tünnermann, A. *Optics Letters* **39**(24), 6875 dec (2014).

[101] Limpert, J., Stutzki, F., Jansen, F., Otto, H.-J., Eidam, T., Jauregui, C., and Tünnermann, A. *Light: Science & Applications* **1**(4), e8–e8 apr (2012).

[102] Limpert, J., Klenke, A., Kienel, M., Breitkopf, S., Eidam, T., Hadrich, S., Jauregui, C., and Tunnermann, A. *IEEE Journal of Selected Topics in Quantum Electronics* **20**(5), 268–277 sep (2014).

[103] Müller, M., Kienel, M., Klenke, A., Gottschall, T., Shestaev, E., Plötner, M., Limpert, J., and Tünnermann, A. *Optics Letters* **41**(15), 3439 aug (2016).

[104] Rothhardt, J., Hädrich, S., Shamir, Y., Tschnernajew, M., Klas, R., Hoffmann, A., Tadesse, G. K., Klenke, A., Gottschall, T., Eidam, T., Limpert, J., Tünnermann, A., Boll, R., Bomme, C., Dachraoui, H., Erk, B., Di Fraia, M., Horke, D. A., Kierspel, T., Mullins, T., Przystawik, A., Savelyev, E., Wiese, J., Laarmann, T., Küpper, J., Rolles, D., Limpert, J., and Tünnermann, A. *Optics Express* **24**(16), 18133 aug (2016).

[105] Grischkowsky, D. and Balant, A. C. 109–116. Springer, Boston, MA (1982).

[106] Nisoli, M., Silvestri, S. D., and Svelto, O. *Applied Physics Letters* **68**(20), 2793 jun (1998).

[107] Zhang, X., Libertun, A. R., Paul, A., Gagnon, E., Backus, S., Christov, I. P., Murnane, M. M., Kapteyn, H. C., Bartels, R. A., Liu, Y., and Attwood, D. T. *Optics Letters* **29**(12), 1357 jun (2004).

[108] Pronin, O., Pervak, V., Fill, E., Rauschenberger, J., Krausz, F., and Apolonski, A. *Optics express* **19**(11), 10232–40 may (2011).

[109] Klas, R., Kirsche, A., Tschernajew, M., Rothhardt, J., and Limpert, J. *Optics Express* **26**(15), 19318 jul (2018).

[110] Chapman, H. N., Barty, A., Bogan, M. J., Boutet, S., Frank, M., Hau-Riege, S. P., Marchesini, S., Woods, B. W., Bajt, S., Benner, W. H., London, R. A., Plönjes, E., Kuhlmann, M., Treusch, R., Düsterer, S., Tschentscher, T., Schneider, J. R., Spiller, E., Möller, T., Bostedt, C., Hoener, M., Shapiro, D. A., Hodgson, K. O., van der Spoel, D., Burmeister, F., Bergh, M., Caleman, C., Huldt, G., Seibert, M. M., Maia, F. R. N. C., Lee, R. W., Szöke, A., Timneanu, N., and Hajdu, J. *Nature Physics* **2**(12), 839–843 nov (2006).

[111] Zürch, M., Rothhardt, J., Hädrich, S., Demmler, S., Krebs, M., Limpert, J., Tünnermann, A., Guggenmos, A., Kleineberg, U., and Spielmann, C. *Scientific reports* **4**, 7356 jan (2014).

[112] Ravasio, A., Gauthier, D., Maia, F. R. N. C., Billon, M., Caumes, J.-P., Garzella, D., Géléoc, M., Gobert, O., Hergott, J.-F., Pena, A.-M., Perez, H., Carré, B., Bourhis, E., Gierak, J., Madouri, A., Mailly, D., Schiedt, B., Fajardo, M., Gautier,

J., Zeitoun, P., Bucksbaum, P. H., Hajdu, J., and Merdji, H. *Physical Review Letters* **103**(2), 028104 jul (2009).

[113] Zürch, M., Kern, C., and Spielmann, C. *Optics Express* **21**(18), 21131 sep (2013).

[114] Gardner, D. F., Zhang, B., Seaberg, M. D., Martin, L. S., Adams, D. E., Salmassi, F., Gullikson, E., Kapteyn, H., and Murnane, M. *Optics Express* **20**(17), 19050 aug (2012).

[115] Guizar-Sicairos, M., Thurman, S. T., and Fienup, J. R. *Optics Letters* **33**(2), 156 jan (2008).

[116] Hädrich, S., Kienel, M., Müller, M., Klenke, A., Rothhardt, J., Klas, R., Gottschall, T., Eidam, T., Drozdy, A., Jójárt, P., Várallyay, Z., Cormier, E., Osvay, K., Tünnermann, A., and Limpert, J. *Optics Letters* **41**(18), 4332 sep (2016).

[117] Mercère, P., Zeitoun, P., Idir, M., Le Pape, S., Douillet, D., Levecq, X., Dovillaire, G., Bucourt, S., Goldberg, K. A., Naulleau, P. P., and Rekawa, S. *Optics Letters* **28**(17), 1534 sep (2003).

[118] Eisebitt, S., Lüning, J., Schlotter, W. F., Lörgen, M., Hellwig, O., Eberhardt, W., and Stöhr, J. *Nature* **432**(7019), 885–888 dec (2004).

[119] Tadesse, G. K., Eschen, W., Klas, R., Hilbert, V., Schelle, D., Nathanael, A., Zilk, M., Steinert, M., Schrempel, F., Pertsch, T., Tünnermann, A., Limpert, J., and Rothhardt, J. *Scientific Reports* **8**(1), 8677 jun (2018).

[120] *CXRO X-Ray Interactions With Matter* (www.henke.lbl.gov/optical_constants/), Accessed 2018–01–20.

[121] Thibault, P., Dierolf, M., Menzel, A., Bunk, O., David, C., and Pfeiffer, F. *Science* **321**(5887) (2008).

[122] Zhang, B., Gardner, D. F. D. D. F., Seaberg, M. D. M. M. D., Shanblatt, E. R., Kapteyn, H. C., Murnane, M. M., and Adams, D. E. *Ultramicroscopy* **158**, 98–104 nov (2015).

[123] Baksh, P. D., Odstrčil, M., Kim, H.-S., Boden, S. A., Frey, J. G., and Brocklesby, W. S. *Optics Letters* **41**(7), 1317 apr (2016).

[124] Tadesse, G. K., Eschen, W., Klas, R., Tschernajew, M., Tuitje, F., Steinert, M., Zilk, M., Schuster, V., Zürch, M., Pertsch, T., Spielmann, C., Limpert, J., and Rothhardt, J. *Scientific Reports* **9**(1), 1735 feb (2019).

[125] Guizar-Sicairos, M., Holler, M., Diaz, A., Vila-Comamala, J., Bunk, O., and Menzel, A. *Physical Review B* **86**(10), 100103 sep (2012).

[126] van Heel, M. and Schatz, M. *Journal of Structural Biology* **151**(3), 250–262 sep (2005).

[127] Horstmeyer, R., Heintzmann, R., Popescu, G., Waller, L., and Yang, C. *Nature Photonics* **10**(2), 68–71 feb (2016).

[128] Fleck, J. A., Morris, J. R., and Feit, M. D. *Applied Physics* **10**(2), 129–160 jun (1976).

[129] Goldberg, K. A., Benk, M. P., Wojdyla, A., Mochi, I., Rekawa, S. B., Allezy, A. P., Dickinson, M. R., Cork, C. W., Chao, W., Zehm, D. J., Macdougall, J. B., Naulleau, P. P., and Rudack, A. volume 9048, 90480Y. International Society for Optics and Photonics, apr (2014).

[130] Goldberg, K. A., Mochi, I., Benk, M. P., Lin, C., Allezy, A., Dickinson, M., Cork, C. W., Macdougall, J. B., Anderson, E. H., Chao, W., Salmassi, F., Gullikson, E. M., Zehm, D., Vytla, V., Cork, W., DePonte, J., Picchi, G., Pekedis, A., Katayanagi, T., Jones, M. S., Martin, E., Naulleau, P. P., and Rekawa, S. B. volume 8880, 88800T. International Society for Optics and Photonics, sep (2013).

[131] Hellweg, D., Weiss, M., Perlitz, S., Peters, J. H., Harnisch, W., and Goldstein, M. volume 8322, 83220L. International Society for Optics and Photonics, mar (2012).

[132] Helfenstein, P., Mohacsi, I., Rajeev, R., and Ekinci, Y. *Journal of Micro/Nanolithography, MEMS, and MOEMS* **15**(3), 034006 sep (2016).

[133] Kienel, M., Müller, M., Klenke, A., Limpert, J., and Tünnermann, A. *Optics Letters* **41**(14), 3343 jul (2016).

[134] Cherukara, M. J., Nashed, Y. S. G., and Harder, R. J. *Scientific Reports* **8**(1), 16520 dec (2018).

[135] Mamezaki, D., Harada, T., Nagata, Y., and Watanabe, T. volume 10454, 1045413. International Society for Optics and Photonics, jul (2017).

[136] Zhang, B., Adams, D. E., Seaberg, M. D., Gardner, D. F., Shanblatt, E. R., Kapteyn, H., and Murnane, M. volume 9050, 90501D. International Society for Optics and Photonics, apr (2014).

[137] Gebhardt, M., Gaida, C., Heuermann, T., Stutzki, F., Jauregui, C., Antonio-Lopez, J., Schulzgen, A., Amezcua-Correa, R., Limpert, J., and Tünnermann, A. *Optics Letters* **42**(20), 4179 oct (2017).

[138] Gaida, C., Gebhardt, M., Heuermann, T., Stutzki, F., Jauregui, C., and Limpert, J. *Optics Letters* **43**(23), 5853 dec (2018).

[139] Li, J., Ren, X., Yin, Y., Zhao, K., Chew, A., Cheng, Y., Cunningham, E., Wang, Y., Hu, S., Wu, Y., Chini, M., and Chang, Z. *Nature Communications* **8**(1), 186 dec (2017).

[140] Gaumnitz, T., Jain, A., Pertot, Y., Huppert, M., Jordan, I., Ardana-Lamas, F., and Wörner, H. J. *Optics Express* **25**(22), 27506 oct (2017).

[141] Kling, M. F. and Vrakking, M. J. *Annual Review of Physical Chemistry* **59**(1), 463–492 may (2008).

Summary

Imaging using sources in the XUV and X-ray spectral range combines high resolution with longer penetration depth (compared to electron/ion microscopy) and found applications in many areas of science and technology. Coherent diffractive imaging (CDI) techniques, in addition, lift the performance limitation of conventional XUV/X-ray microscopes imposed by image forming optics and enable diffraction limited resolutions. Until recently, CDI techniques were mainly confined to large scale facilities e.g. synchrotrons and X-ray free electron lasers due to unavailability of suitable table-top XUV/X-ray sources. Table-top sources based on high-order harmonic generation (HHG) nowadays offer high and coherent photon flux which widened the accessibility of CDI techniques. First imaging experiments already showed the potential of HHG-based setups albeit with limited resolution on features much larger than the illuminating wavelength. So far, table-top CDI systems were not able to resolve sub-100 nm features using performance metrics that can qualify these systems for real world applications. The huge progress in scaling the coherent flux of HHG sources driven by high power femtosecond fiber laser systems presented unique opportunities for reaching new regimes in imaging performance. However, experimental issues with power handling and the onset of so-far-unexplored resolution limits for wavelength-scale features were some of the challenges that needed to be addressed. In this work, CDI experiments with the highest resolutions in different modalities using a high flux fiber laser driven HHG source are presented. In conventional CDI, a record-high resolution of 13 nm is demonstrated together with the possibility of high speed acquisition with sub-30 nm resolution. In a holographic implementation of CDI, features with a half-distance of 23 nm are resolved which are the smallest features to ever be resolved with a table-top XUV/X-ray imaging system. In addition, waveguiding effects are shown to affect image quality and limit the achievable resolution in these wavelength-sized features. Ptychographic imaging of extended samples is also performed using a reliable Rayleigh-like resolution metric and resolving of features as small as 2.5λ (sub-50 nm) is demonstrated. Together with the significant reduction in measurement times, the imaging results presented push the performance of table-top CDI systems a step closer to that required for real world applications. The scalability of the HHG flux at higher photon energies (soft X-rays) with the power of the driving fiber laser system promises to deliver imaging setups with few nanometer resolutions in the near future. These systems can find applications in material and biological sciences, study of ultrafast dynamics, imaging of semiconductor structures and EUV lithographic mask inspection.

Zusammenfassung

Bildgebung mit XUV- und Röntgenstrahlung verbindet hohe Auflösung mit größeren Eindringtiefen (verglichen mit Elektronen- oder Ionenmikroskopie) und findet Anwendung in vielen Bereichen der Wissenschaft und Technik. Bildgebung durch kohärente Beugung (englisch: coherent diffractive imaging, kurz: CDI) umgeht die Limitierung von konventionellen XUV-/Röntgenmikroskopen, welche durch die bildgebenden Optiken gegeben sind, und ermöglicht deshalb Bildgebung mit beugungsbegrenzter Auflösung. Bis vor kurzem war CDI hauptsächlich an Großforschungseinrichtungen wie zum Beispiel Synchrotrons bzw. Freie-Elektronen-Laser möglich, da keine kompakten XUV-/Röntgenquellen in Laborgröße zugänglich waren. Die Erzeugung von hohen Harmonischen (englisch: high harmonic generation, kurz: HHG) mit ausreichend hohem kohärenten Photonenfluss erlaubt kohärente Beugungs-Bildgebung im Labormaßstab. Erste Experimente haben bereits das Potential kohärenter Bildgebung mithilfe dieser Lichtquellen aufgezeigt. Bisher konnten jedoch nur Strukturen aufgelöst werden, die wesentlich größer als die verwendete Wellenlänge und größer als 100 nm waren. Zusätzlich verhinderten die bisher erzielten Messzeiten (in der Größenordnung von Stunden) gezielte Anwendungen der kohärenten Bildgebungsmethoden auf konkrete Fragestellungen im Labormaßstab. Die enorme Steigerung des kohärenten Photonenflusses von HHG-Quellen mit Hilfe von Hochleistungs-Faserlasern ermöglichte es, im Rahmen der vorliegenden Arbeit, ein neues Regime in der XUV-Bildgebung zu erschließen. So konnte eine Reihe von Bildgebungsexperimentes unter Verwendungen von verschiedenen kohärenten Bildgebungsmethoden realisiert werden, jeweils mit Rekordauflösung und deutlich verringerten Messzeiten. Jedoch galt es auch experimentelle Herausforderungen in Bezug auf die Handhabung der hohen Durchschnittsleistung der verwendeten Hochleistungslaser zu bewältigen. Mittels konventioneller CDI wurde erstmals eine Auflösung von 13 nm erzielt. Zusätzlich konnten Hochgeschwindigkeitsmessungen mit 30 nm Auflösung und 3 s Integrationszeit realisiert werden. Unter der Verwendung einer holographischen Methode konnten nur 23 nm große Strukturen mit hohem Kontrast aufgelöst werden. Dies entspricht den kleinsten Strukturen, die jemals mit irgendeiner XUV-/Röntgen-Quellen im Labormaßstab aufgelöst werden konnten. Gleichzeitig konnten neue Limitierungen bei der Auflösungen von Strukturen, deren Abmessungen in der Größenordnung der Wellenlänge der verwendeten Strahlung liegen, aufgedeckt und erklärt werden. Die Zugrunde liegenden Wellenleitereffekte beeinflussen die Bildqualität und die erreichbare Auflösung erheblich. Die Umsetzung einer weiteren Bildgebungsmethode, der sogenannten Ptychographie, erlaubte

es auch ausgedehnte (nicht-isolierte) Proben hochauflösend abzubilden. Hierbei wurde erstmals mittels eines Rayleigh-ähnlichen Kriteriums eine Auflösung von 2.5λ (sub-50 nm) an einem Siemensstern demonstriert. Verbunden mit einer signifikanten Reduktion der benötigten Messzeit auf wenige Sekunden pro Einzelbild, sind die erzielten Ergebnisse ein großer Schritt in Richtung Anwendung. Die lineare Skalierbarkeit des HHG Flusses bei hohen Photonenenergien (weicher Röntgenbereich) über die Erhöhung der Leistung des treibenden Faserlasers verspricht in Zukunft Auflösungen von wenigen Nanometern. Solche Nanoskope können eine Vielzahl von Anwendungen in Materialwissenschaften, Biologie, Mikroelektronik oder bei in der EUV-Maskeninspektion finden.

Acknowledgement

First of all, I would like to extend my gratitude to my supervisors Dr. Jan Rothhardt and Prof. Jens Limpert for guiding me through this work and creating different opportunities to help me progress in my scientific carrier. I feel deeply indebted to the Helmholtz Institute Jena from which I received help and support in completing my studies. My colleagues Wilhelm Eschen, Robert Klas, Maxim Tschernajew and Vinzenz Hilbert in the XUV subgroup were of great help through the difficult phases of my work and I am grateful for having them around. I would also like to thank my colleagues at the 'Fiber and Waveguide Lasers' group: Dr. Birgitta Schultze-Bernhardt, Dr. Cesar Jauregui, Dr. Arno Klenke, Joachim Buldt, Christian Gaida, Martin Gebhardt, Tobias Heuermann, Alexander Kirsche, Chang Liu, Michael Müller, Vittoria Schuster, Evgeny Shestaev, Lars Henning Stark, Albrecht Steinkopff, Christopher Aleshire, Christoph Stihler, Ziyao Wang and Philipp Gierschke. Finally, I am deeply thankful to have my family and friends whose support and encouragement was of great comfort.

Ehrenwörtliche Erklärung

Ich erkläre hiermit ehrenwörtlich, dass ich die vorliegende Arbeit selbständig, ohne unzulässige Hilfe Dritter und ohne Benutzung anderer als der angegebenen Hilfsmittel und Literatur angefertigt habe. Die aus anderen Quellen direkt oder indirekt übernommenen Daten und Konzepte sind unter Angabe der Quelle gekennzeichnet. Bei der Auswahl und Auswertung folgenden Materials haben mir die nachstehend aufgeführten Personen in der jeweils beschriebenen Weise unentgeltlich geholfen:

1) Die Koautoren der entsprechenden Publikationen bei den durchgeführten Experimenten.
2) Wilhelm Eschen: Datenverarbeitung der ptychographischen CDI Messung und Ausführen der ptychographischen Rekonstruktionen unter Verwendung des Open-Source Ptypy Frameworks.
3) Mathhias Zilk: Durchführen der FDTD Simulationen für die FTH- und Ptychographie-Proben.

Weitere Personen waren an der inhaltlich-materiellen Erstellung der vorliegenden Arbeit nicht beteiligt. Insbesondere habe ich hierfür nicht die entgeltliche Hilfe von Vermittlungs- bzw. Beratungsdiensten (Promotionsberater oder andere Personen) in Anspruch genommen. Niemand hat von mir unmittelbar oder mittelbar geldwerte Leistungen für Arbeiten erhalten, die im Zusammenhang mit dem Inhalt der vorgelegten Dissertation stehen. Die Arbeit wurde bisher weder im In- noch im Ausland in gleicher oder ähnlicher Form einer anderen Prüfungsbehörde vorgelegt. Die geltende Promotionsordnung der Physikalisch-Astronomischen Fakultät ist mir bekannt.

Ich versichere ehrenwörtlich, dass ich nach bestem Wissen die reine Wahrheit gesagt und nichts verschwiegen habe.

Jena, den 28.03.2019

Getnet Kassa Tadesse

Curriculum Vitae

Tadesse, Getnet Kassa

Personal Information

Date of Birth - 09 March, 1988
Place of Birth- Gondar, Ethiopia
Gender - Male

Education

• 1993 – 1999	Meseret Primary School, Gondar, Ethiopia
• 1999 – 2001	Fasiledes Junior High School, Gondar, Ethiopia
• 2001 – 2005	Fasiledes Secondary School, Gondar, Ethiopia
• June 2005	Final secondary school examination
• 2005 – 2009	Bahir Dar University, Bahir Dar, Ethiopia Undergraduate study in Electrical Engineering
• July 2009	B.Sc. degree in Electrical Engineering
• 2009 – 2012	Addis Ababa University, Addis Ababa, Ethiopia Graduate courses in Communication Engineering
• 2012 – 2015	Friedrich Schiller University of Jena, Germany Graduate study in Photonics Abbe School of Photonics Scholarship Thesis: Spectral Beam Combining by Femtosecond Laser Written 2D Volume Bragg Gratings
• Jan. 2015	M.Sc. degree in Photonics
• Feb. 2015 – present	Friedrich Schiller University of Jena, Germany Ph.D. Study in Optics Helmholtz Institute - Advanced Photon Science Scholarship Dissertation title: Nanoscale Coherent Diffractive Imaging using High- harmonic XUV sources

....

Place, Date Getnet Kassa Tadesse